Universidade Federal de Minas Gerais

Shallow sunspot formation, a numerical study using ILES.

by

Francisco Javier Camacho Rodriguez

Dissertation submitted to UNIVERSIDADE FEDERAL
DE MINAS GERAIS as a requisite for the degree of
MASTER IN PHYSICS

Research area: ASTROFISICA
Advisor: Gustavo Andres Guerrero Erazo

Departamento de Fisica - ICEx - UFMG

April 2018

Declaration of Authorship

I, Francisco Javier Camacho Rodriguez, declare that this thesis titled, 'Implicit large eddy simulations of shallow magnetic flux concentrations in stratified turbulent convection' and the work presented in it are my own. I confirm that:

- This work was done wholly or mainly while in candidature for a research degree at this University.
- Where any part of this thesis has previously been submitted for a degree or any other qualification at this University or any other institution, this has been clearly stated.
- Where I have consulted the published work of others, this is always clearly attributed.
- Where I have quoted from the work of others, the source is always given. With the exception of such quotations, this thesis is entirely my own work.
- I have acknowledged all main sources of help.
- Where the thesis is based on work done by myself jointly with others, I have made clear exactly what was done by others and what I have contributed myself.

Signed:

Date: 19th April, 2018

"Astronomy is much more fun when you are not an astronomer."

Brian May

Abstract

Sunspots are dark patches at the surface of the Sun where the magnetic field is strong. To the date, the mechanism by which sunspots are generated remains unclear. In the current literature two types of explanations can be found. The first one is related to buoyant emergence of toroidal magnetic fields generated at the tachocline. The second one states that active regions are formed, from an initially diffused magnetic flux, by MHD instabilities that develop in the near-surface layers of the Sun. Using the anelastic MHD code EULAG-MHD we address the problem of sunspot formation by performing implicit large-eddy simulations of stratified magneto-convection in a domain that mimics the uppermost layers of the Sun. By applying a homogeneous magnetic field over an initially stationary hydrodynamic convective state, we investigate the formation of self-organized magnetic structures. The strength of the imposed magnetic field is a free parameter of the model and varies in the range, $0.01 < B_0/B_{eq} < 0.5$ (where B_{eq} is the characteristic equipartition field strength). Specifically we explore the role of the Negative effective magnetic pressure instability NEMPI (Rogachevskii & Kleeorin (2007), Kleeorin et al. (1996), Brandenburg et al. (2010)) in the formation of such magnetic flux concentrations. Although we observe the formation of magnetic structures with length scales of the order of the largest convective motions, the results are inconclusive to determine whether this instability is the responsible for the formation of the observed structures.

Acknowledgements

First of all I would first like to thank my advisor Gustavo Guerrero for being the one who gave me the hope and motivation to keep working on physics in a moment of my life when I have had given up on continuing with my post-graduate studies, and also for being such an amazing friend during my staying in Brazil. He was always patient and kind to teach me all the tricks that a good programmer need to know to survive the competitive world of Computational Physics. He always steered me in the right direction whenever he thought I needed it, and I will be eternally grateful for that. I also need to thank him for helping me economically during the difficult times I had during my master studies, and for his patience when I had personal problems that delayed the termination of my master studies. His strong but very educative corrections on this final dissertation are also very appreciated. I will always consider him a friend, and he also deserves all of my respect as a physicist.

I thank CAPES and the UFMG Physics department for the scholarship they gave me to make possible my master studies at UFMG in Belo Horizonte. During my time in Brazil I met wonderful people, so many that maybe I won't be able to mention all of them. However, I have to point out the most important ones. I thank the prof. Silvia Alencar for letting me catch a bit of his enormous knowledge in astrophysics. The few seminars, conversations and discussions we had were very educative and certainly will leave mark in my way of thinking as a physicist, she must know that I admire her a lot, not only as a physicist but also as a person. I'm very grateful with all the friends/members of the astrophysics group at UFMG (Bonnie, Alana, Tatiana, Ariana, Julia, Filipe, Mateus, etc ...), and all the other master and PhD fellows at ICEx that I now consider my friends (they are too many to write all of their names, but I will have each one of them in my heart always) for providing me a friendly and warm environment in which I was able to take part in the Brazilian culture and learn Portuguese from the very first day, sometimes in the middle of beers, music and dancing. Special thanks to Bonnie for having the patience to teach me a bit of python and helping me to improve many of the scripts I used for the post-processing of the data from the simulations presented in this dissertation.

The development of this work required a long and very complex sequence of learning steps in programing and physics of MHD turbulence. To perform the simulations presented in this dissertation, very expensive computational resources were needed. I thank the prof. Elisabete Maria de Gouveia Dal Pino and all the staff of the Laboratorio de Astroinformatica (LAi) at IAG-USP in Sao Paulo for letting me to use the **Alphacrucis** cluster for the development of the 2D convection simulations. I also thank the profesor Alexander Kosovichev, from the New Jersey Institute of Technology (NJIT) at

New Jersey, USA, and the NASA Advanced supercomputing division - Computational Physics Branch Chief, Nagi Nicolas Mansour, for granting me to access the supercomputer **Pleiades** to perform the 3D simulations of magneto-convection.

I thank the UCAR Visiting Scientist Programs (VSP) for the invitation to participate in the 2016 NASA Ames Heliophysics Summer Program supported by the NASA LWS Program, and the NASA Ames Research Center for the hospitality during the summer program, time over which part of the work presented in this dissertation was done. I am very grateful to Piotr Smolarkiewickz for his patience helping me to understand the physics of the anelastic model behind the EULAG-MHD code, and to, Irina Kitiashvili, Alexander Kosovichev, Nagi Mansour, Alan Wray and David Hathaway for their advices on the setup of the simulations, and the discussions during the summer program that helped me to find ways to improve the simulations and gain a better understanding of the physics of magneto-convection. I also thank the Sociedade Astronomica Brasilera (SAB), CAPES and SCOSTEP organizations for the grants they gave me to participate in events and symposiums were I was able to present my work and have important discussions with leading-edge researches in the area.

Finally, the most important acknowledgement goes to my family: my dearest mother and brother who are my every-day inspiration to never give up, no matter the problems and obstacles that life put in front of me. Even in the distance, they always encouraged me to keep moving forward. I owe to them everything I am. This dissertation is dedicated to them, specially to my mom, for teaching me that even when you are so fragile physically, you can become invincible if you a have a spirit strong enough to believe you can beat any difficulty. This accomplishment would not have been possible without their support. Thank you.

Contents

Declaration of Authorship i

Abstract iii

Acknowledgements iv

List of Figures viii

List of Tables x

Abbreviations xi

1 Introduction 1
- 1.1 Observable properties of the Solar magnetic field . . . 2
  - 1.1.1 Sunspots and the Solar cycle . . . 2
  - 1.1.2 Solar magnetic cycle . . . 5
- 1.2 Solar Interior . . . 6
  - 1.2.1 Internal structure of the Sun . . . 6
  - 1.2.2 The Sun's Convective Zone . . . 7
  - 1.2.3 Understanding solar convection . . . 9
- 1.3 Sunspot Formation phenomenology . . . 12
  - 1.3.1 The global solar dynamo . . . 12
  - 1.3.2 Deep seated vs Shallow magnetic field . . . 15

2 The Negative effective magnetic pressure instability NEMPI 20
- 2.1 Physics of NEMPI . . . 20
  - 2.1.1 Scale separation of the MHD equations . . . 20
  - 2.1.2 Turbulence effects on Lorentz force . . . 23
  - 2.1.3 Growth rate of NEMPI for imposed vertical field . . . 26
- 2.2 State of art of NEMPI . . . 29
  - 2.2.1 First numerical hints of NEMPI . . . 29
  - 2.2.2 Isothermal DNS with forced turbulence . . . 30
  - 2.2.3 Flux concentrations in polytropic atmospheres . . . 31
  - 2.2.4 Magnetic flux concentrations in convection simulations . . . 33

3 Numerical simulation of turbulent convection **35**
3.1 Direct Numerical Simulation (DNS) . . . 35
3.1.1 Richardson cascade . . . 35
3.1.2 Kolmogorov microscales . . . 36
3.1.3 Energy spectra and Kolmogorov $-5/3$ law . . . 38
3.1.4 Numerical resolution constraints . . . 40
3.2 Large Eddy Simulation (LES) . . . 42
3.2.1 Filtered equations and SGS models . . . 42
3.2.2 DNS vs LES . . . 44
3.3 Implicit Large Eddy Simulation . . . 46
3.3.1 The basic MPDATA . . . 46
3.3.2 The ILES character of MPDATA . . . 49

4 The model **51**
4.1 EULAG-MHD . . . 51
4.1.1 The set of equations . . . 51
4.1.2 Aneslastic atmosphere . . . 52
4.1.3 Closure for the Reynolds heat flux . . . 53
4.2 Setup of the simulations . . . 54
4.2.1 Physical and code units . . . 54
4.2.2 Cartesian box setup . . . 54

5 Results: Solar convection and magnetic structures with EULAG **57**
5.1 HD convective states . . . 57
5.1.1 Two dimensional HD simulations with EULAG . . . 57
5.1.2 Three dimensional HD simulations . . . 62
5.2 Simulations with imposed magnetic field . . . 66
5.2.1 Low resolution simulations . . . 66
5.2.2 High resolution simulations . . . 69
5.2.3 Calculation of NEMPI coefficients . . . 74

6 Conclusions and future work **77**

Bibliography **79**

List of Figures

1.1 Sunspot groups observed by Schwabe per year from 1826 to 1843 3
1.2 International sunspot number from 1750 to 2010 4
1.3 Comparison of Sunspot number by Hoyt & Schatten (1998) with pseudoSSN from cosmogenic radioisotopes 4
1.4 Magnetograms of the sunspot cycles 22 and 23. 5
1.5 Magnetic Butterfly Diagram taken from instruments on Kitt Peak and SOHO. 6
1.6 The Solar interior 7
1.7 Image of solar granulation obtained with the primary mirror of the Big Bear Solar Observatory (BBSO) 8
1.8 Dopplergram of the supergranulation from data by SOHO/MDI/ESA . . 9
1.9 Seismic constraints on the convective spectrum obtained by Hanasoge et al. (2012) using data from HMI (Schou et al., 2012) 11
1.10 Internal structure of solar convection as depicted by Spruit et al. (1990) . 11
1.11 Mean rotation profile of the sun obtained from GONG data 13
1.12 Parker's picture of cyclonic turbulence 14
1.13 Illustration of the omega and alpha effects in the Sun 16

2.1 NEMPI coefficients obtained from a DNS by Brandenburg et al. (2010) . 30
2.2 xz slices of $(\overline{B}_y - B_0)/B_{eq0}$ for $R_m = 6$, taken from the simulations performed by Brandenburg et al. (2011) 31
2.3 xz slices of $(\overline{B}_y - B_0)/B_{eq0}$ for $R_m = 36$, taken from the simulations performed by Brandenburg et al. (2011) 31
2.4 xy cuts of $B_z/B_{eq}(z)$ at the top boundary of the simulations performed by Losada et al. (2014) 32
2.5 Effective magnetic pressure as a function of β_{eq} from a DNS with polytropic stratification performed by Losada et al. (2014) 33
2.6 Horizontal slices of B_z near the top surface for different box sizes from the convection simulations performed by Käpylä et al. (2016) 34

3.1 Turbulent energy cascade as envisaged by Richardson. 36
3.2 Sources and sinks in the Richardson's energy cascade. 38
3.3 Full representation of the Richardson's energy cascade. 40
3.4 Representation of a typical energy spectrum for a high Reynolds number flow. 40
3.5 Graphical representation of a 2D resolution sufficiently good to capture the Kolmogorov scale in a tubulent flow. 41

3.6 Comparison of energy spectra obtained from DNS (Kaneda et al., 2003), hyperviscosity (Haugen & Brandenburg, 2004) and Smagorinsky LES (Haugen & Brandenburg, 2006) simulations. 45
3.7 Stencil representation of MPDATA. 48

4.1 Schematics of the cartesian boxes considered for the simulations with a four-layer stratification. Horizontally, all boxes have dimensions of $50 \times 50 \times 20$ Mm. 55
4.2 Polytropic stratification considered for the magneto-convection simulations with EULAG-MHD 55

5.1 x-z slices of the vertical velocity, u_z, for the 2D convection simulations. . 60
5.2 Kinetic energy spectra for the 2D simulations. 61
5.3 x-z slices of the radial velocity u_z for the 3D HD convection simulations . 63
5.4 x-y slices of the radial velocity u_z for the 3D HD convection simulations. . 64
5.5 Kinetic energy spectra for the 3D HD simulations. 64
5.6 Radial profiles of horizontally averaged u_{rms} and θ' for the 3D HD convection simulations. 65
5.7 Kinetic and magnetic energy spectra for the simulation **MHD-LR-0.1**. . 67
5.8 xy cuts (at $z = 18.8$ Mm) of u_z and B_z for the simulation **MHD-LR-0.1**. 68
5.9 xy cuts (at $z = 15.6$ Mm) of u_z and B_z for the simulation **MHD-LR-0.1**. 68
5.10 xz cuts (at $y = 28.0$ Mm) of u_z and B_z for the simulation **MHD-LR-0.1**. 69
5.11 Kinetic and magnetic energy spectra for the high resolution simulations **MHD-HR-0.05** and **MHD-HR-0.1**. 70
5.12 xy cuts (at $z = 18.8$ Mm) of u_z and B_z for the simulation **MHD-HR-0.05**. 71
5.13 xy cuts (at $z = 15.6$ Mm) of u_z and B_z for the simulation **MHD-HR-0.05**. 71
5.14 xz cuts (at $y = 30.5$ Mm) of u_z and B_z for the simulation **MHD-HR-0.05**. 72
5.15 xy cuts (at $z = 18.8$ Mm) of u_z and B_z for the simulation **MHD-HR-0.1**. 73
5.16 xy cuts (at $z = 15.6$ Mm) of u_z and B_z for the simulation **MHD-HR-0.1**. 73
5.17 xz cuts (at $y = 29.0$ Mm) of u_z and B_z for the simulation **MHD-HR-0.1**. 74
5.18 Profiles of the NEMPI coefficient $q_p(z)$ for the MHD simulations 75

List of Tables

5.1 Results for the 2D simulations 58

Abbreviations

CME	**C**oronal **M**ass **E**jections
DNS	**D**irect **N**umerical **S**imulation
GONG	**G**lobal **O**scillation **N**etwork **G**roup
HMI	**H**elioseismic and **M**agnetic **I**mager
ILES	**I**mplicit **L**arge **E**ddy **S**imulation
LES	**L**arge **E**ddy **S**imulation
MEA	**M**odified **E**quation **A**nalysis
MHD	**M**agneto-**H**ydro **D**ynamics
MLT	**M**ixing **L**ength **T**heory
MPDATA	**M**ulti-dimensional **P**ositive **D**efinite **A**dvection **T**ransport **A**lgorithm
NEMPI	**N**egative **E**ffective **M**agnetic **P**ressure **I**nstability
NFV	**N**on-oscillatory **F**inite **V**olume
SDO	**S**olar **D**ynamics **O**bservatory
SGS	**S**ub-**G**rid **S**cale

Dedicated to the strongest woman I've ever met, my mother.

Chapter 1

Introduction

One of the most relevant unanswered questions in astrophysics, concerns to the generation and dynamics of the large-scale magnetic field observed in cosmic objects. The magnetism on Earth has been known by humans since very ancient times. Nowadays, it is known that our planet has its own magnetic field generated by a dynamo mechanism that operates at the inner liquid core (McElhinny & Senanayake (1980), Roberts & Glatzmaier (2001)). The magnetism in stars is a more recent discovery. The first evidence of magnetism in astrophysical objects different from Earth was found by Hale in 1908. When he observed Zeeman splittings of sunspot's spectra, indicated the existence of a magnetic field in the Sun. Nowadays the existence of magnetic fields in stars (Reiners, 2012), galaxies (Beck & Wielebinski, 2013) and clusters of galaxies (Govoni & Feretti, 2004), is a conclusively established fact.

Our understanding of the solar magnetic fields has grown considerably over the last century, however, many questions remain open. In addition, our capability of predicting solar events, like solar flares and coronal mass ejections (CME), is still too far from being achieved. It is believed that these solar events are correlated with the appearance of sunspots (Schrijver & Siscoe, 2012). However, the mechanism by which sunspots are formed remains uncertain. A concise understanding of sunspot formation could reveal hints on the way solar flares and CME's can be predicted.

Solar flares are violent, rapid explosions where magnetic energy stored below the solar atmosphere is released mostly in the form of electromagnetic radiation (flares encompass various forms of energy, but the main contribution is radiative energy, Shibata & Magara (2011)). When twisted magnetic field lines nearby active regions intersect, a reconnection process ocurrs. In this event, the energy of the magnetic field is converted into thermal energy and leads to acceleration of particles, including electrons and protons (Schrijver & Zwaan, 2008). A CME is a large-scale eruption that carries a huge amount of plasma

(up to 10^{13} kg) to the interplanetary space. In a typical CME, a large magnetic loop with a size comparable to the solar radius moves away from the Sun at speeds of about $30 - 2500$ km/s (Yashiro et al., 2004).

The largest flares (classified as X-class flares) may have a significant effect on Earth. For instance, the electromagnetic radiation resulting from such event can eventually reach the Earth's atmosphere driving long-lasting radiation storms which, in turn, could trigger radio blackouts. A smaller class of flares called M-class can cause brief radio blackouts in polar regions. The radiation coming from flares can also put risk on astronauts in space. Like solar flares, CMEs generate an increase in radiation that affects astronauts and electronics in space, but they can also bring charged particles that interact and distort the Earth's magnetic field (Schwenn, 2006).

The relevance of solar events like flares and CMEs, together with their possible connection with the process of sunspot formation, makes sunspots a necessary topic of research. In this work, we study the possible mechanisms by which sunspots could be generated. In this chapter we review the most relevant properties of the observable solar magnetic field revealed in the form of active regions at the surface. Then we discuss the main properties of the solar interior and the dynamo theory which explains the generation of magnetic field in the convection zone. Finally, we discuss the different scenarios by which astrophysicist attempt to explain the formation of sunspots. The connection between the observable magnetic field and the dynamo-generated field at the interior of the Sun is then established.

1.1 Observable properties of the Solar magnetic field

1.1.1 Sunspots and the Solar cycle

Since the discovery of Hale, the study of the magnetic field in the Sun has been done through the observation of its active regions at the surface. Active regions are defined as localized regions where a strong magnetic field inhibits the convection. The surface area where the strong field is present, looks darker than its surroundings. Some active regions can be seen as dark patches at the surface of the Sun, commonly called sunspots. These sunspots can appear as dipolar structures or as groups of relatively smaller patches (Schrijver & Zwaan, 2008).

The number of sunspots varies with time in a periodic form, as it was first shown by Schwabe (1844). He published the first conclusive evidence of a periodic cycle in the solar activity based on his observations of the number of sunspot groups over a period

of 18 years (1826 - 1843). In his report, the data indicate a cycle with a period of about 10 years (See Fig. 1.1). It is possible to see irregularities in the amplitude and shape of the activity cycle from the Schwabe's data (note that the maximum of the first cycle is rather smaller than the second one). Also, there is an asymmetry in the location of the maxima relative to the length of the cycle, i.e., the number of sunspots exhibits a fast rise and a slow decay.

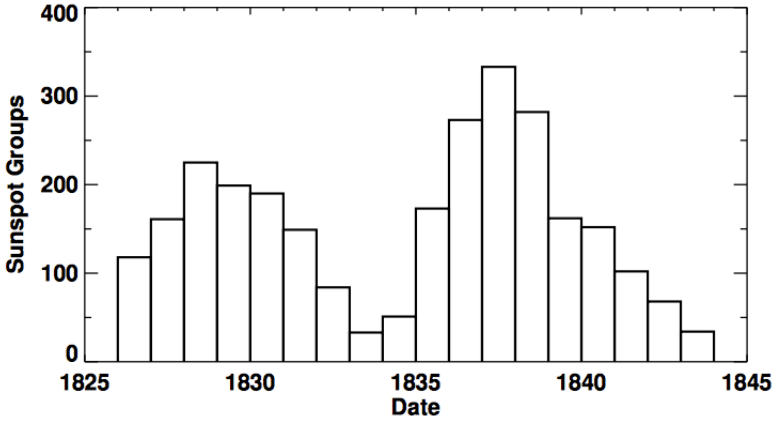

FIGURE 1.1: Sunspot groups observed by Schwabe per year from 1826 to 1843 (Schwabe, 1844)

In 1849 Rudolf Wolf established a standard technique for measuring the solar activity in terms of the nowadays so-called Wolf sunspot number (or Zurich relative sunspot number):

$$R = k\,(10g + f)\,, \tag{1.1}$$

where f is the number of individual sunspots, g is the number of sunspot groups, and k is a correction factor for calibration between different observers. Nowadays it is used the international sunspot number (since 1981, when the Royal observatory of Belgium assumed the process of measurement) which is a weighted average of the measurements of many observers based on the Wolf standard. The measurements of the activity clearly show the existence of a solar cycle. With the monthly averages of the daily international sunspot number made since 1750 (measurements previous to Schwabe were reconstructed with the data collected by other observers around the world, Hathaway (2015)), the variations in amplitude, shape and length of the cycle period seen in Schwabe's data are evident (see Fig. 1.2). One of the most outstanding irregularities of the activity cycle is the amplitude of the maxima. For instance, strong variations in the amplitude of the cycle maxima can be seen between the years 1800 and 1820. This event, known today as the Dalton minimum, belongs to a class of events characterized by a deep and prolonged minimum in the sunspot cycle (similar events can be seen in fig. 1.3).

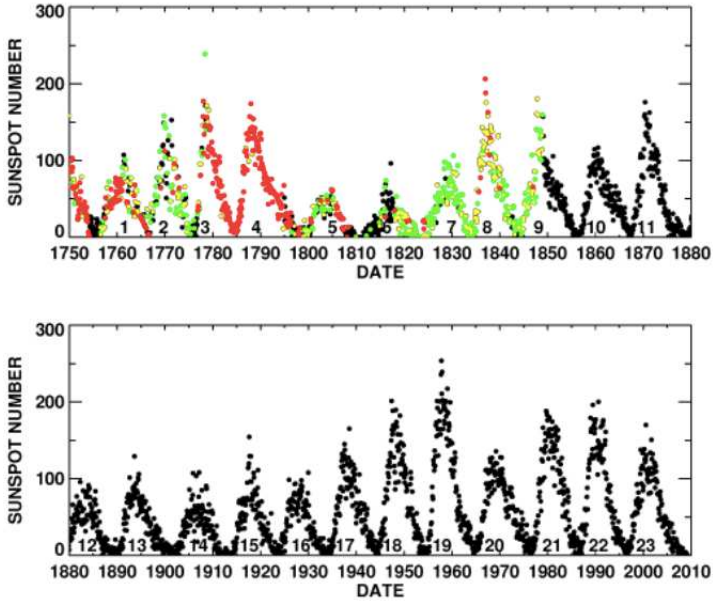

FIGURE 1.2: Monthly averages of the daily International sunspot number from 1750 to 2010. Months with daily observations are shown in black. Months missing 1-10, 11-20 and more than 20 days of observations are shown in green, yellow and red, respectively (Hathaway, 2015).

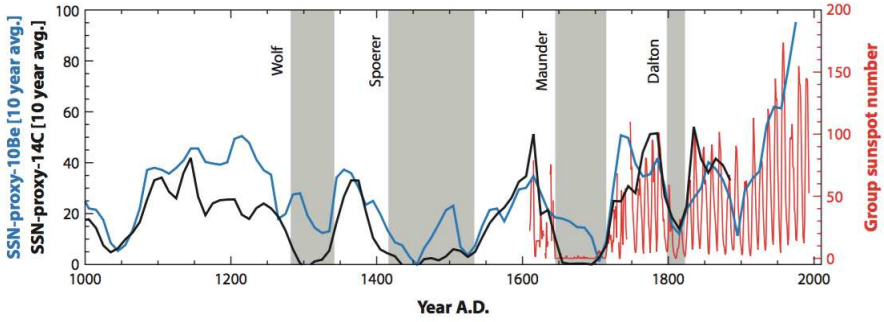

FIGURE 1.3: "Time series of the sunspot group number by Hoyt & Schatten (1998) together with pseudoSSN time series constructed from two cosmogenic radioisotopes" (figure courtesy of I. Usoskin, Sodankyla Obs).

Fig. 1.3 shows the current record of sunspot groups number measurements, starting at the beginning of the telescopic era (early seventeenth century), together with indirect measurements of solar activity made using the radioisotopes ^{14}C and ^{10}Be. These are produced in the Earth's stratosphere by the impact of galactic cosmic rays on ^{14}N and ^{16}O. (The solar cycle modulates the flux of cosmic rays on earth leading to variations in the atmospheric abundances of these isotopes). In this figure the Dalton minimum can be observed as well. In addition, more prolonged activity minima can be observed over the last one thousand years (Maunder, Spörer and Wolf). The appearance of minima in the activity cycle seems to be a pseudo-regular pattern in the sense that they appear repeatedly but with a fluctuating period.

1.1.2 Solar magnetic cycle

Nowadays, it is possible to analyse the magnetic field over the entire surface of the Sun. By exploiting the Zeeman effect [1], graphical representations of the magnetic field strength over the solar surface can be created. The result is called a magnetogram, it exhibits the most noticeable properties of the solar magnetic field. Fig. 1.4 shows magnetograms of two consecutive sunspot cycles. As it can be observed in the yellow-blue shades of Fig 1.4, the strongest active regions have a dipolar structure. Moreover, in opposite hemispheres the dipolar groups have opposite leading magnetic polarities (here leading refers to the strongest spot that appears eastwards). It is also interesting to note that the leading spot in a dipolar group switches polarity from one cycle to the next. This is known as the Hale's polarity rule (Hale et al., 1919). In 1959 it was found that the polar field reverses polarity with the same periodicity as the sunspot cycle (Babcock, 1959), suggesting the existence of another cycle related directly with the magnetic field itself, with a period that should be about twice the period of the sunspot cycle, i.e., $\sim$ 22 years.

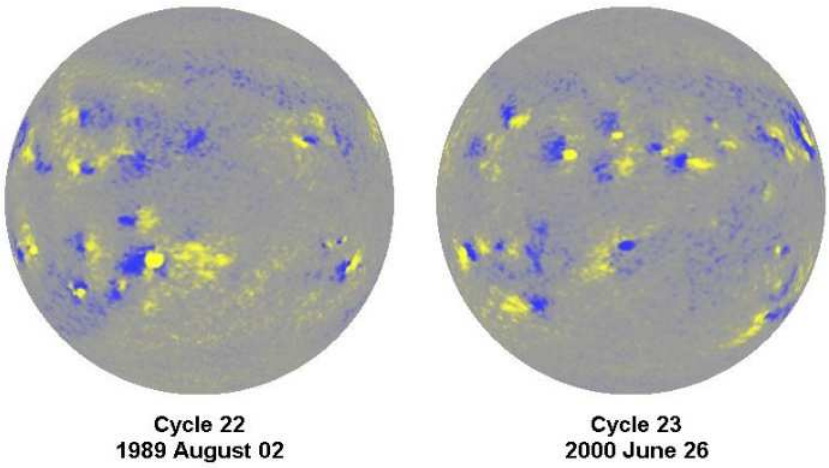

FIGURE 1.4: From Left to right, magnetograms corresponding to the sunspot cycles 22 and 23 respectively. Yellow indicates radial magnetic field out of the page, while blue denotes radial field going into the page (taken from Hathaway (2015)).

In addition to Hale's polarity rule, there are other two important features of the solar magnetic field, called respectively, the Joy's and Spörer's rules. Fig. 1.5 shows the magnetic butterfly diagram of the Sun from 1975 to 2010, which shows the longitudinally averaged radial magnetic field as a function of time. From it we distinguish a equatorward migration of active regions. At the beginning of the cycle, sunspots appear around

[1] The Zeeman effect is the splitting of spectral lines of radiation emitted by an atom in the presence of a magnetic field. This is due to the interaction of the magnetic field with the magnetic moment of the electrons which results in a change of the energy of the atom.

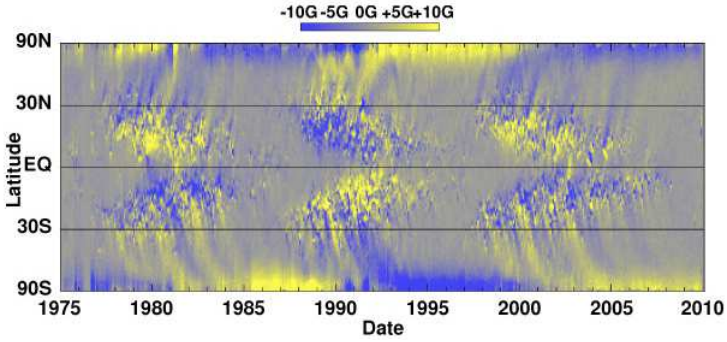

FIGURE 1.5: Magnetic Butterfly Diagram constructed from the longitudinally averaged radial magnetic field obtained from instruments on Kitt Peak and SOHO (taken from Hathaway (2015)).

$30° - 40°$ latitude. As the cycle progresses, they appear at lower and lower latitudes. During the maximum, the latitude of appearance is $\sim 15°$ and by the end of the cycle, sunspots appear at $\sim 7°$. This characteristic is known as the Spörer's law (Schrijver & Zwaan, 2008).

As sunspot pairs migrate equatorwards, they appear tilted with the leading sunspot in each pair always closer to the equator than the following sunspots. The tilting angle decreases as the sunspot pair approaches the equator. This phenomenon is known as the Joy's law (Dasi-Espuig et al., 2010). While a magnetogram analysis is enough to distinguish the Joy's law, the features described by Hale's and Spörer's laws are observed in a magnetic butterfly diagram. From Fig. 1.5 it is also easy to note the reversal of polar magnetic field, and therefore the existence of a magnetic cycle associated with a large-scale solar magnetic field. Any theory or model aiming to explain the existence of a magnetic field in the Sun, should be able to reproduce the properties presented above. However, up to date, there is not a model able to successfully explain all these properties.

1.2 Solar Interior

1.2.1 Internal structure of the Sun

To understand the evolution of the solar magnetic field and the way it manifests at the surface (as sunspots for example), it is crucial to study the solar interior. Thus, the dynamical relation between the plasma motions and the magnetic field generation and evolution can be unveiled. The interior of the Sun is divided into three layers as shown in Fig. 1.6. The interface between radiative and convective zones is not explicitly shown.

This thin layer is known as tachocline and it defines the transition between solid body rotation and differential rotation (Hughes et al., 2012).

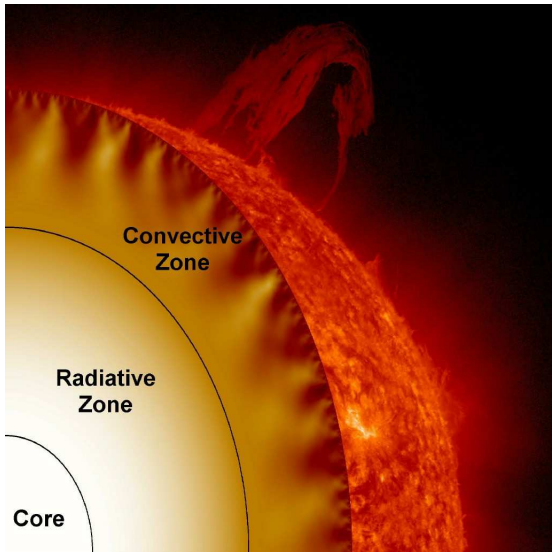

FIGURE 1.6: In the innermost 25 % of the solar interior energy is generated through nuclear reactions. This energy propagates outward in the form of photons along the radiative zone and then in the form of convective motions in the outermost 30 % of the star.

The innermost 25 % of the Sun constitutes the central core. There the energy is generated through nuclear reactions that burn hydrogen to form helium. The energy generated in the core starts propagating outwards along the radiation zone in the form of photons. Once inside the dense material in this layer the photons are absorbed and emitted from one particle to another a great number of times. If a single photon were traced, it would take about a million years to reach the interface with the convective zone.

The most external layer is the convective zone. In this region the atoms don't release the energy so easily, reducing considerably the transport of energy by radiation (except in a thin thermal layer near the surface). In the convective zone the transport of energy occurs via the buoyant rising of warm parcels of fluid, i.e., thermal convection.

1.2.2 The Sun's Convective Zone

Imagine that at the bottom of a pot of boiling water an element of fluid, carrying a certain amount of heat, rises up adiabatically. It means that the element rises slowly enough so that it remains in pressure equilibrium with its surroundings, but quickly enough so that temperature equilibrium is not achieved. Formally, this is equivalent to the thermodynamic concept of an adiabatic process. The fluid element will continue to rise up over a certain lengthscale after which it releases its energy as heat. This is the simplest idea behind the convective transport of energy. Formally speaking, convection happens in an

atmosphere where its temperature gradient is larger than the gradient corresponding to a blob of fluid rising adiabatically under the same boundary conditions[2]. In the solar convection zone happens a similar process driving stellar convection. However, unlike the pot of boiling water, solar convection is a non-local process, highly turbulent and occurs in a strongly stratified rotating atmosphere. It gives to the convective transport of energy inside the Sun a quite dynamical richness and complexity.

Current solar interior models (Christensen-Dalsgaard et al., 1996) show that the stratification of the convection zone is almost adiabatic except by a thin layer at the surface called the ionization layer. Within this layer, the mean-free path of the photons is comparable to the distance to the solar surface, i.e., the plasma that reaches this layer starts to loose a considerable fraction of its thermal energy by radiation. In the solar case, convection could be mainly driven by radiative cooling occurring at the ionization layer as proposed by Stein & Nordlund (1989). The ionization process that takes place at the surface layers leads to cold overdense plasma that is pulled down by gravity. As a result, strong downflows are generated at this layer. These downflows are able to propagate down to the bottom of the convection zone, crossing the layers where the atmopshere is nearly adiabatic in a process called overshooting. This mechanism implies that the resulting convection is non-local. This is in contrast with the simplified picture of the convection inside a pot of boiling water, where the mechanism is intrinsically local.

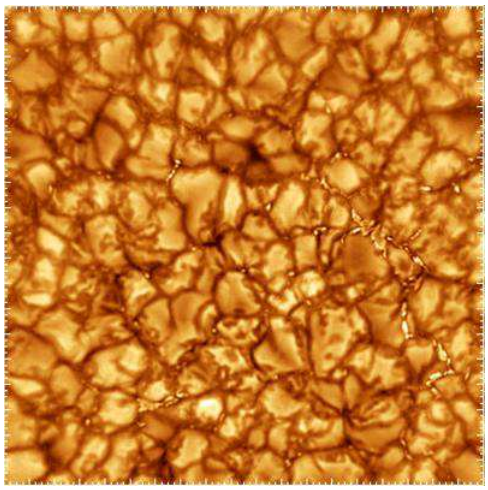

FIGURE 1.7: Solar granulation covering a field of 19,312 by 19,312 km obtained with the primary mirror of the solar telescope at Big Bear Solar Observatory (BBSO) of the New Jersey Institute of Technology (NJIT).

The most distinctive intensity variations of the solar surface, aside from sunspots, are granules (bright areas surrounded by dark lanes). The granulation pattern covers the

[2]Here we denote the atmosphere temperature gradient by, $\nabla = d(log(T))/d(log(P))$, where, T, is the temperature and, P, is the pressure. Besides, we denote by, $\nabla_{ad} = d(log(T_{ad}))/d(log(P_{ad}))$, the adiabatic gradient of the rising parcel of fluid. Convection occurs when the condition, $\nabla > \nabla_{ad}$, is satisfied.

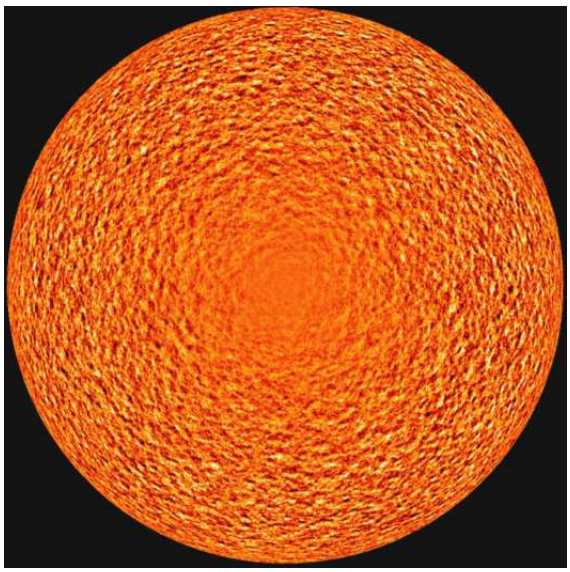

FIGURE 1.8: A Dopplergram revealing the supergranulation pattern (credits SOHO/MDI/ESA)

entire surface of the Sun, apart from active regions (see Fig. 1.7). Nowadays, we know that granulation is a manifestation of convective heat transport with horizontal scales of the order of $\sim$ 1 Mm. Besides granulation, there is observational data that fairly suggest the existence of another large-scale convective pattern in the surface layers of the Sun called supergranulation (See Fig 1.8). The length scale of this flow pattern lies within the range of $20 - 70$ Mm (Hathaway et al. (2000), Rieutord et al. (2008)). The most accurate hypotheses aiming to describe the plasma flow inside the convection zone should be in agreement with the patterns of granulation and supergranulation observed at the surface. See the reviews by Rieutord & Rincon (2010) and Nordlund et al. (2009) for a comprehensive description of the observed granular and supergranular flow patterns at the Sun's surface layers.

1.2.3 Understanding solar convection

The observational data of the granulation and supergranulation patterns is insufficient to infer the internal convective structure. Therefore, numerical models are the appropriate tool to study the physics of these flows. However, modelling solar convection remains as a formidable challenge. Any discussion on the modelling of solar convection starts with the simplest approach based on what is known as the mixing-length theory (MLT). The "toy model" of the pot of boiling water explained in the previous section represents the basic idea behind MLT. More precisely, in the MLT the convective transport of energy is supposed to be performed by parcels of fluid of characteristic spatial and velocity scales. These fluid elements should be coherent over a lengthscale called the *mixing length*.

Despite its simplicity, the MLT has been remarkably successful as a key element of some stellar structure models (di Mauro et al., 2010). Furthermore, recent three-dimensional anelastic simulations of global convection (Käpylä et al. (2010); Guerrero et al. (2013); Hotta et al. (2014), Hotta et al. (2015)) result in convective turnover time and velocity amplitudes comparable to those of MLT predictions. MLT predicts an increase of the density and pressure scale heights with depth, suggesting the existence of large convective cells (termed as *giant-cells*) in the deeper layers of the convection zone. Several observational attempts to detect giant cells have been performed using data either from the solar surface (Hathaway et al., 2014) or from the solar interior (Duvall, 2003). However, the results remain inconclusive or insufficient to prove the existence of convective giant-cells. This difficulty suggests that the typical size of these giant-cells should be considerably smaller than the one predicted by MLT, thus implying that MLT could be an incomplete theory for solar and stellar convection. Time-distance helioseismology inversions [3] performed by Hanasoge et al. (2012) placed limits on the velocity spectrum in the bulk of the convective zone. These limits, together with the velocity spectrum obtained from a simulation of anelastic convection using the Anelastic Spherical Harmonic code (ASH) are shown in Fig. 1.9 for comparison (The red and blue lines denote data taken at different depths, while the dashed and continuous lines correspond to the results from the simulations and helioseismology inversions, respectively). The differences between observations and ASH simulations suggest that the solar convection might be operating in a non-MLT regime.

As mentioned before, another mechanism for solar convection has been proposed as an alternative for MLT (Spruit et al., 1990). This mechanism was first suggested by Stein & Nordlund (1989) after the analysis of fully compressible hydrodynamical convection simulations including surface radiative transfer. In these simulations, the authors identified a plume-based convective structure. A tree-like structure of vertically elongated and narrow downflows is observed in the vertical direction while in the horizontal directions, the upflows form closed areas surrounded by downflow lanes. The area of the upflows increases at deeper layers (See Fig. 1.10). Under this scenario the topology of the velocity field in the solar interior is dominated by the effects of a strong density stratification. However, the convection is driven by the radiative cooling due to Hydrogen ionization in the near surface layers. This results in a local entropy decrease and then in strong downdrafts. The scale of convection is set by the pressure scale height of the stratification.

[3] Helioseismology is an observational technique by which the internal structure and dynamics of the Sun can be inferred from observed frequencies and travel times of acoustic waves propagating within the star. For a detailed discussion see Kosovichev (1999).

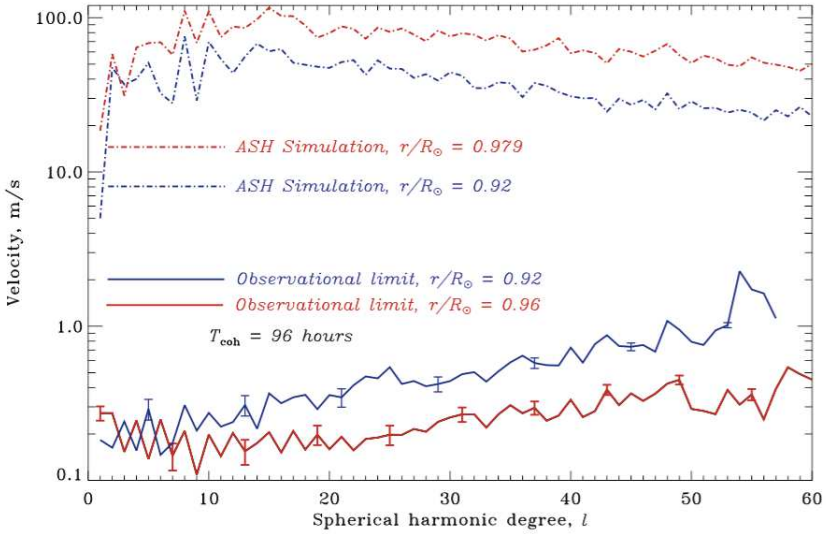

FIGURE 1.9: Seismic constrains obtained by Hanasoge et al. (2012) using data from HMI (Schou et al., 2012). Upper bounds on the observed convective spectrum compared with the Aneslastic Spherical Harmonic (ASH) convective spectrum are shown (The red and blue lines denote data taken at different depths, while the dashed and continuous lines correspond to the results from the simulations and helioseismology inversions, respectively). The differences suggest that solar convection might be operating in a non-MLT regime.

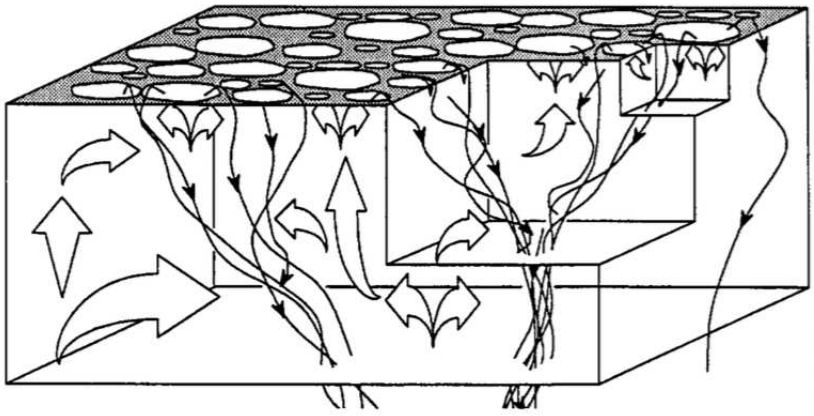

FIGURE 1.10: Representation of the successive merging structure of the internal convective downdrafts onto larger and larger scales at deeper layers of the convection zone (from Spruit et al. (1990)).

1.3 Sunspot Formation phenomenology

1.3.1 The global solar dynamo

In 1919 Larmor suggested that the mechanism responsible for the existence of the solar magnetic field could be a dynamo process, where the observed magnetic field could be generated by plasma motions inside the Sun. In the subsequent years different flow configurations allowing the development of a dynamo were identified (Roberts, 1970). However, in 1934 Cowling showed that an axisymmetric magnetic field cannot be maintained by plasma motions (Busse, 2007), leading to the conclusion that the magnetic field of the Sun could not be axisymmetric (Cowling, 1945). Later, with a separation of the magnetic and flow fields into mean and turbulent components Parker (1955a) formulated the so-called mean-field theory (MFT). The MFT identifies the effect of small scale kinetic helicity: $k_H = (\nabla \times \vec{u}) \cdot \vec{u}$ as a source of large scale magnetic field. This is a crucial ingredient for the existence of a solar dynamo. In this sense, Parker's formulation represents a consistent way to explain the solar dynamo without violating Cowling's theorem.

The next step was to figure out which flow configurations, under this framework, could produce a large-scale magnetic field similar to the one observed in the Sun. In the following years the solar dynamo theory incorporated the constraints imposed by solar observation of the plasma motions; namely, the differential rotation and the meridional flow.

Differential Rotation. In the latitude, the solar angular velocity is larger at the equator and decreases monotonically towards the poles. This pattern persists with depth until the tachocline (Schou et al., 1998). The solar rotation is not uniform, it has solid body rotation in the radiative core and differential rotation in the bulk of the convection zone (see Fig. 1.11). It has been observed that close to the surface the angular velocity decreases at all latitudes, creating the so called near-surface shear layer. Therefore, there is radial shear both, at the tachocline and at the near-surface layers (Howe, 2009).

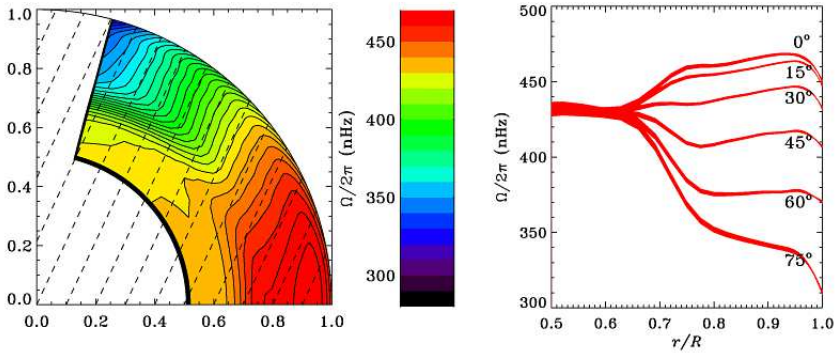

FIGURE 1.11: Mean rotation profile from GONG data; contours of constant rotation (left), showing lines at 25° to the rotation axis as dashed lines, after Howe et al. (2005), and cuts at constant latitude as a function of radius (right), after Howe et al. (2000).

Meridional circulation. There is conclusive evidence of a large-scale meridional flow (r and θ directions) with a poleward component at the surface of the Sun (see Ulrich (2010) and references therein). However, there is no consensus about the location of the equatorward return flow and the meridional flow profile in the interior of the convection zone. By using data from SDO/HMI, Zhao et al. (2013) found a double-cell circulation profile in radius. Jackiewicz et al. (2015) found a similar profile from helioseismic inversions of GONG data. However, Schad et al. (2013) found a different spatial structure of multiple cells distributed in depth and latitude.

The observed granulation and supergranulation patterns as well as the torsional oscillations[4] are other flow constraints that also serve as a diagnostic to test dynamo models (See Cameron et al. (2016)). To analyze how the plasma motions can generate the large-scale magnetic field, it is usual to consider the large-scale magnetic field as axially symmetric, and to decompose it into its toroidal, $\vec{B}_\phi = (0, B_\phi, 0)$, and poloidal, $\vec{B}_p = (B_r, 0, B_\theta)$, components. The poloidal component (typically assumed as a dipole field) might be stretched in the azimuthal direction by the *differential rotation* so that a toroidal component can be generated eventually. This is the so-called Ω-*effect*. Accordingly to Joy's law, the preferential nearly East-West orientation of dipolar sunspot groups suggests that the active regions should emerge from a nearly toroidal magnetic flux bundle below the surface of the Sun. There is no controversy in the literature about this mechanism. However, since the Ω effect alone is not able to explain how the poloidal field could be maintained, it is not sufficient to self-consistently describe a large-scale dynamo. Parker (1955a) suggested that the helicity of the turbulent motions of the rotating plasma could solve this issue.

[4]There is observational evidence of periodic variations of Sun's angular velocity of about $\pm 0.5\%$ of the average rotation profile shown in Fig. 1.11 (Howe et al., 2011). These periodic variations are known as torsional oscillations.

When rising blobs of plasma expand laterally tend to rotate due to the Coriolis effect. This implies that they rotate clockwise in the northern hemisphere and counterclockwise in the southern hemisphere, and so does the magnetic field within these blobs. Thus, the rising loops of magnetic field are twisted, leading to a transformation of toroidal field into poloidal field and vice-versa (See Fig. 1.12). The generation of poloidal field by the helicity of convective motions is usually called the α-*effect* (Schrijver & Zwaan, 2008). Both, the Ω and α effects can have different relative magnitudes, leading to different dynamos as follows:

$\alpha\Omega$ *dynamo*: In the generation of toroidal field, the α effect has little influence when compared with the Ω effect.

α^2 *dynamo*: In this case the Ω effect does not contribute to the generation of the toroidal field. The α effect alone is sufficient to sustain the dynamo.

$\alpha^2\Omega$ *dynamo*: In this case both, the α and Ω effects, contribute similarly in the self-sustainability of the dynamo.

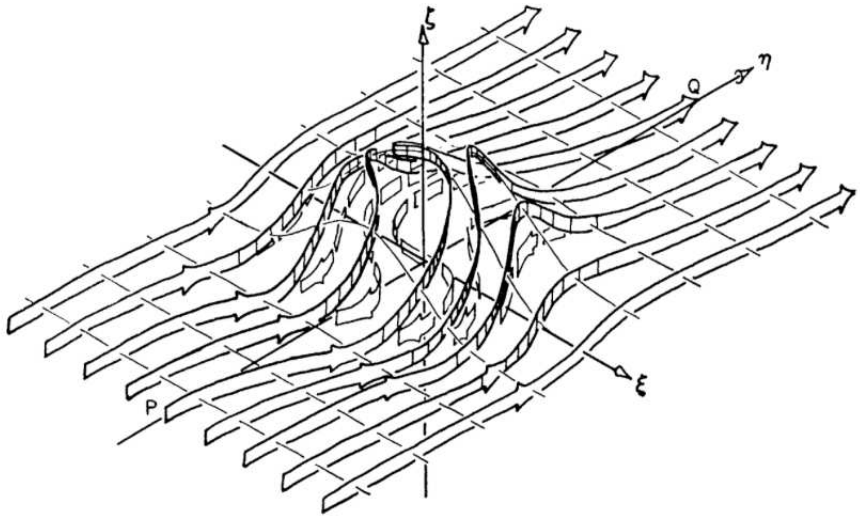

FIGURE 1.12: Parker's picture of cyclonic turbulence twisting toroidal magnetic field (pointing in the η direction) into meridional planes (given by the coordinates $[\xi, \zeta]$) (Parker, 1955a)

In the solar case, it is usually estimated that the generation of toroidal field is mainly due to differential rotation (Ω effect). Thus, the solar dynamo is assumed to be of the $\alpha\Omega$ *dynamo* class (Charbonneau, 2010). Parker showed that for semi-infinite Cartesian geometry, the $\alpha\Omega$ dynamo model allows the existence of traveling-wave-like solutions, offering a simple and elegant explanation for the equatorward migration of sunspot groups. Those kinds of dynamo solutions were extended to spherical geometry by Yoshimura (1975) who showed that these so-called dynamo waves propagate in a direction $\vec{s}$ given by:

$$\vec{s} = \alpha \nabla \Omega \times \hat{e}_{\phi}, \tag{1.2}$$

where, α represents the tensor component, $\alpha_{\phi\phi}$

[5], and, $\hat{e}_{\phi}$, is the unit vector in the azimuthal direction (See Moffatt (1978)). According to the Parker-Yoshimura rule (Eq. 1.2), in the case of the Sun, equatorward propagation at low latitudes is possible if the $\alpha_{\phi\phi}$ tensor component is negative (positive) in the Northern (Southern) hemisphere, and the dynamo is concentrated within the equatorial part of the Tachocline where $\nabla\Omega \sim \partial\Omega/\partial r > 0$ (See left panel of Figure 1.11). However it is still unclear if $\alpha_{\phi\phi}$ for the case of solar convection, has the right sign so that the equatorward migration can be readily explained by Eq. 1.2. Several attempts of measuring the components of the α effect tensor in turbulent convection simulations have been performed (See Charbonneau (2014)). The results mostly lead to a turbulent α effect positive (negative) in the bulk of the convection zone's Northern (Southern) hemisphere. This leads to poleward migration of the dynamo waves.

The flux-transport solar dynamo approach (Dikpati & Charbonneau (1999), Nandy & Choudhuri (2002), Guerrero & de Gouveia Dal Pino (2008), Jiang et al. (2014)) was proposed as an alternative to overcome this issue. It uses the large-scale meridional flow (assuming that it is directed equatorwards at the base of the convection zone) as a conveyor belt that advects the magnetic field towards the desired latitudes. Since the magnetic field is generated at the tachocline, this model assumes that the sunstpots form from magnetic flux bundles that rise from the bottom of the convection zone. Under certain parameters, flux-transport models result in patterns of propagation of the magnetic field which agree with the one observed in the butterfly diagram (See Fig. 1.5). However, as mentioned before to the date there is no consensus about the direction of the meridional flow at the base of the convection zone.

1.3.2 Deep seated vs Shallow magnetic field

According to the current paradigm, the sunspot groups emerge from a toroidal magnetic flux bundle originated at the base of the convection zone. This toroidal flux is believed to be generated by the stretching of the poloidal field via the Ω effect (Cameron et al., 2016). Afterwards, the toroidal flux emerges up to the surface due to magnetic buoyancy and gives rise to magnetic loops that appear as the active regions (Parker, 1955b). Since loops on opposite hemispheres should generate dipolar active regions with opposite leading

[5] In general, the alpha effect must be parameterized by a second order tensor, α_{ij}. Cyclonic turbulence can appear in any direction, say i, having effect in the generation of magnetic field in any other direction, say j.

polarities, this picture is consistent with the Hale's polarity law (See left panel of Fig. 1.13). The right panel of Fig. 1.13 shows reconnecting loops of twisted toroidal field that merge to maintain the large-scale poloidal field in a statistical process called the Babcock-Leighton (BL) mechanism (Choudhuri, 2013). It is worth noticing that, similar to the turbulent α-effect, the BL mechanism is able to generate a poloidal field from a toroidal one. It is until now not clear if both effects coexist in the dynamo process and what is their relative importance.

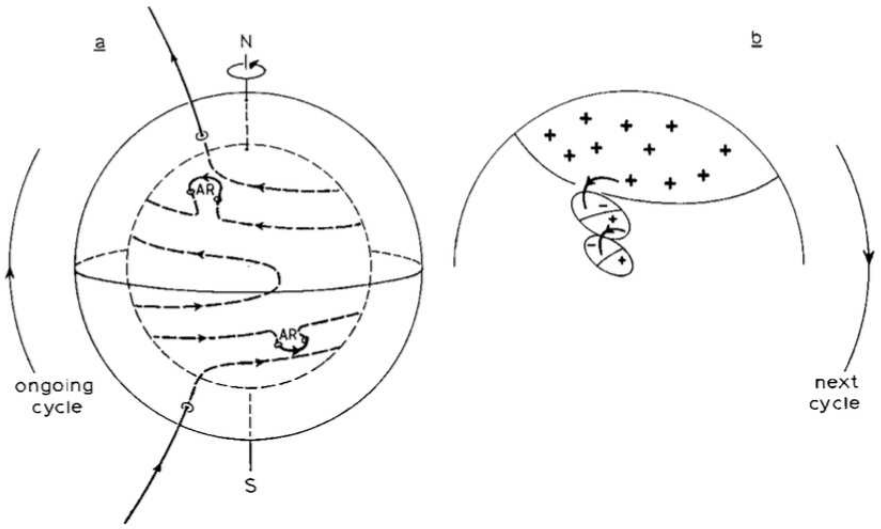

FIGURE 1.13: Panel a: Differential rotation stretches the poloidal magnetic field to generate nearly toroidal flux bundles that eventually break through the photosphere forming bipolar active regions. Panel b: Reconnecting flux loops as pictured by the dynamo flux-transport model (Zwaan, 1996)

.

Despite the simplicity and beauty of this phenomenological picture, the detailed dynamics behind the emergence of toroidal field as dipolar active regions remains unclear. The precise connection between the magnetic field generated by the solar dynamo and the observable magnetic field at the surface is still uncertain. The scenario described above implies that the magnetic flux tubes need to cross the entire convection zone to reach the photosphere. Thus, they must overcome the distortions due to turbulent convection and remain coherent across a layer of about 20 pressure scale heights. High resolution observations (Domínguez Cerdeña et al. (2003); Khomenko et al. (2003); Socas-Navarro & Sánchez Almeida (2003), Orozco Suárez et al. (2007)) show that the magnetic field on the photosphere's active regions contain discrete flux tubes of high field strength ($B > 10^3 G$) with a hierarchy of cross-sectional sizes ranging from sunspots to below the limit of instrumental resolution. Therefore, it is natural to suppose that the subsurface magnetic fields within the convection zone are also concentrated in the form of discrete flux tubes.

The evolution of buoyant magnetic flux tubes were studied first through linear stability analysis (Spruit & van Ballegooijen (1982), Ferriz-Mas & Schuessler (1990), Ferriz-Mas & Schüssler (1993), Ferriz-Mas & Schüssler (1995)). The authors found the magnitude of the toroidal field necessary to drive the instability for different regions, at or below the tachocline. Later on, buoyancy was studied numerically with the so-called thin flux tube approximation, where the flux tubes were considered to have only one dimension. These models were able to qualitatively reproduce phenomenological sunspot rules like Joy's law (Fan, 2009). However, they face a number of issues. For instance, the strength of the toroidal magnetic field at the tachocline. According to Caligari et al. (1995), it should be of the order of 10^5 G for the flux tube to become unstable and cross the convective zone. This value is about two orders of magnitude larger than the equipartition magnetic field, B_{eq}, that represents the energy available from the plasma turbulent motions. More recent flux tube simulations (Fan et al. (2003), Cline (2003)) revealed that for field strengths at the tachocline greater that $3B_{eq}$, magnetic buoyancy dominates over the convective downdrafts and therefore the flux tube can rise up to the surface.

Another important problem refers to the coherence that the flux tube has to maintain during the rising process. Simulations performed by Guerrero & Käpylä (2011), including convection and shear, are able to form flux ropes which expand and loose coherence during their rise through a convection zone. A certain amount of twist is required to maintain the tubes coherent after their interaction with irregular convective downdrafts. The origin of this twist, however, cannot be easily explained (Fan, 2009). Recent observations of horizontal flows around active regions find another discrepancy between the buoyancy scenario and the formation of sunspots. By contrasting measurements of horizontal flows at the solar surface around active regions with those obtained by realistic simulations of sunspot formation, Birch et al. (2016) found that the subsurface rise speed of emerging flux must be no larger than 150 m/s at a depth of 20 Mm. The prediction of the standard thin flux model for this rise speed is about 500 m/s (Fan, 2009). Because of the larger influence of the Coriolis force on rising flux tubes with speeds about 150 m/s, the emergent bipolar regions will disagree with the Joy's law. However, the previous helioseismology measurements by Kosovichev et al. (2000) and Ilonidis et al. (2011) found that the emergence speed can be as large as 1 km/s in the top 70 Mm layer. These results were recently confirmed by Kosovichev et al. (2016).

In view of these difficulties, other mechanisms have been proposed to explain sunspot formation. An alternative model suggests that the magnetic flux concentrations, relevant for the generation of active regions, can spontaneously occur due to MHD instabilities developing at the upper layers of the convective zone, i.e., sunspot formation could be a shallow phenomenon. The negative effective magnetic pressure instability (NEMPI) (Kleeorin et al. (1989), Kleeorin et al. (1996), Rogachevskii & Kleeorin (2007)) is one

possible scenario for the generation of flux concentrations. Under certain conditions, the turbulent terms of the Lorentz force in the momentum equation can lead to a sign reversal in the magnetic effective pressure which induces the growth of an instability (the detailed physical formulation of NEMPI is presented in Chapter 2). The first numerical evidence of such instability in a direct numerical simulation (DNS, see chapter 3 for details) was obtained by Brandenburg et al. (2011) by considering stably stratified, externally forced, isothermal, hydromagnetic turbulence. More recent simulations of forced turbulence in polytropic atmospheres (Losada et al., 2014) have confirmed the formation of shallow magnetic structures. Simulations where the turbulence arises in a natural way, e.g., turbulent convection, have also shown the formation of magnetic structures in the near-surface layers (Käpylä et al. (2012), Käpylä et al. (2016)). However, the presence of NEMPI in these simulations is still unclear. Another model of magnetic flux concentrations was developed by Kitiashvili et al. (2016) who performed realistic 3D radiative compressible MHD simulations using a LES (Large Eddy Simulation, see chapter 3 for details) approach. They found that pore-like structures can be spontaneously formed from an initially uniform magnetic field. In this case, the instability is driven by interacting magnetized vortex tubes. The large scale magnetic structure is maintained by converging downdrafts. Such downdrafts have been observed by helioseismology (e.g. Zhao et al. (2001)).

The study of formation of magnetic structures in turbulent convection has been performed in DNS and LES. In this work we explore the same phenomenon by using implicit sub-grid scale (SGS) modelling, often termed as ILES (Implicit Large Eddy Simulation, see chapter 3 for details). The simulations are performed with the code EULAG-MHD. This code is widely known for its success in modeling atmospheric and astrophysical multiscale-flows (Smolarkiewicz & Charbonneau, 2013). It has been shown that its Multidimensional positive definite advection transport algorithm (MPDATA, see chapter 3) leads to an implicit SGS model for the turbulent motions (Grinstein et al., 2007). The simulations consider a Cartesian domain of $50 \times 50 \times 20$ Mm divided by three layers: a convection-unstable layer for the uppermost 2 Mm, a convection-stable layer for the innermost 2 Mm and an adiabatic one in the middle. This setup aims to mimic the uppermost part of the convection zone. However, since we do not consider radiative transfer which plays an important role driving the convection in the Sun (Stein & Nordlund, 1989), we impose a negative gradient of entropy at the top of the domain. The convection driven in this thin superadiabatic region penetrates down to the bottom of the domain creating a multi-scale convective pattern. Once the convection reaches a statistically steady state, we impose a homogeneous vertical magnetic field with different strengths. We analize the presence of NEMPI and its correlation with the magnetic

structures in our simulations. In addition, we explore the effects of varying the numerical resolution, which, for the case of our implicit SGS model, represents increasing the effective Reynolds and magnetic Reynolds numbers.

This dissertation is organized a follows: In Chapter 2 a comprehensive introduction to the physics concerning NEMPI is presented, next we present the state of the art of the research related to this instability. Chapter 3 encompasses a minimum set of concepts and definitions required to understand the different schemes used in numerical simulation of MHD turbulent convection (DNS, LES and ILES). At the end of this chapter, the MPDATA scheme is presented, followed by the details of the numerical setup considered for the simulations performed in this work. The results and analysis are presented in Chapter 4. Finally, the conclusions and future work are presented in Chapter 5.

Chapter 2

The Negative effective magnetic pressure instability NEMPI

In this chapter we present the physics concerning NEMPI. We introduce first the basic mean-field MHD equations. Then, following Käpylä et al. (2012), a closure for the turbulent contributions of the momentum-stress tensor is considered. From this we define the effective magnetic pressure, P_m and identify a regime where it might have negative values. We also show that an instability develops when the derivative of P_m assumes negative values. Finally, in the second part of the chapter, we discuss the state of the art of the research related to this instability.

2.1 Physics of NEMPI

2.1.1 Scale separation of the MHD equations

To understand the effect of the negative effective magnetic pressure instability we need to study the effects of turbulence in the mean Lorentz force. To that end, for any field variable in the MHD equations of motion, ψ, we consider a Reynolds average[1] , $\overline{\psi}$, and the fluctuations around that average, ψ' (such that $\psi = \overline{\psi} + \psi'$). This procedure is most commonly known as Reynolds decomposition (in this framework the fluctuations are considered much smaller than the averages, thus, $\psi' \ll \overline{\psi}$). First, consider the momentum equation in tensor notation:

[1] We refer here to a Reynolds average as to any average that satisfies a certain set of rules known as Reynolds conditions (Pope, 2000). These conditions include linearity of the average and commutativity with space and time derivatives.

$$\rho \frac{\partial u_i}{\partial t} = -\frac{\partial}{\partial x_j}\Pi_{ij} + \rho g_i, \tag{2.1}$$

where g_i denotes the components of the gravitational field, and Π_{ij} is the momentum-stress tensor that encompasses the viscous and magnetic contributions:

$$\Pi_{ij} = \rho u_i u_j + \delta_{ij}\left(p + \frac{\mathbf{B}^2}{2\mu_0}\right) - \frac{1}{\mu_0} B_i B_j - \sigma_{ij}. \tag{2.2}$$

Here u_i and B_i are the components of the velocity and magnetic fields, respectively. σ is the viscous stress tensor with, $\sigma_{ij} = 2\nu\rho S_{ij}$, where ν is the kinematic viscosity and S_{ij} the rate-of-strain tensor (Pope, 2000; Davidson, 2015). Applying a Reynolds average over the momentum equation (2.1) leads to:

$$\overline{\rho} \frac{\partial \overline{u}_i}{\partial t} = -\frac{\partial}{\partial x_j}\overline{\Pi}_{ij} + \overline{\rho} g_i, \tag{2.3}$$

where the gravitational field, g_i, is considered constant [2] and low-Mach number turbulence is considered, i.e., turbulent velocity correlations with density fluctuations are ignored ($\overline{\rho u_i} \sim \overline{\rho}\,\overline{u}_i$). The averaged momentum-stress tensor is given by:

$$\overline{\Pi}_{ij} = \overline{\rho}\,(\overline{u_i u_j}) + \delta_{ij}\left(\overline{p} + \frac{\overline{\mathbf{B}^2}}{2\mu_0}\right) - \frac{1}{\mu_0}\overline{B_i B_j} - \overline{\sigma}_{ij}. \tag{2.4}$$

Now, we consider the Reynolds scale separation ($\mathbf{B} = \overline{\mathbf{B}} + \mathbf{B}'$, $\mathbf{u} = \overline{\mathbf{u}} + \mathbf{u}'$, $p = \overline{p} + p'$) to split the averaged momentum-stress tensor into their mean and turbulent (fluctuating) parts; namely, $\overline{\Pi}_{ij}^{(m)}$ and $\overline{\Pi}_{ij}^{(f)}$ ($\overline{\Pi}_{ij} = \overline{\Pi}_{ij}^{(m)} + \overline{\Pi}_{ij}^{(f)}$). Substitution of the Reynolds scale separation into (2.4) leads to:

$$\begin{aligned}
\overline{\Pi}_{ij} = {} & \overline{\rho}\left[\overline{(\overline{u}_i + u_i')(\overline{u}_j + u_j')}\right] \\
& + \delta_{ij}\left(\overline{p} + \frac{1}{2\mu_0}\overline{(\overline{B}_k + B_k')(\overline{B}_k + B_k')}\right) \\
& - \frac{1}{\mu_0}\left[\overline{(\overline{B}_i + B_i')(\overline{B}_j + B_j')}\right] - \overline{\sigma}_{ij}.
\end{aligned} \tag{2.5}$$

Since the viscous stress tensor is linear in the flow field components (Pope, 2000):

[2] For a constant gravitational field we have $g_i' = 0$, thus, $g_i = \overline{g_i}$.

$$\sigma_{ij} = 2\nu\rho\left[\frac{1}{2}\left(\frac{\partial u_i}{\partial x_j} + \frac{\partial u_j}{\partial x_i}\right) - \frac{1}{3}\delta_{ij}(\partial_k u_k)\right], \tag{2.6}$$

it does not contribute to the turbulent momentum-stress tensor $\overline{\Pi}_{ij}^{(f)}$. After some algebra on the eq. (2.5), and using some properties of Reynolds averages ($\overline{\phi_i\overline{\beta}_j} = \overline{\phi}_i\overline{\beta}_j$ and $\overline{\phi'}_i = 0$), the total momentum-stress tensor reduces to:

$$\begin{aligned}\overline{\Pi}_{ij} = &\left[\overline{\rho}\left(\overline{u}_i\overline{u}_j\right) + \delta_{ij}\left(\overline{p} + \frac{\overline{\mathbf{B}}^2}{2\mu_0}\right) - \frac{1}{\mu_0}\overline{B}_i\overline{B}_j - \overline{\sigma}_{ij}\right] \\ &+ \left[\overline{\rho}\left(\overline{u_i'u_j'}\right) + \delta_{ij}\left(\frac{\overline{\mathbf{B}'^2}}{2\mu_0}\right) - \frac{1}{\mu_0}\overline{B_i'B_j'}\right],\end{aligned} \tag{2.7}$$

where the mean and turbulent parts can be identified as:

$$\overline{\Pi}_{ij}^{(m)} = \overline{\rho}\left(\overline{u}_i\overline{u}_j\right) + \delta_{ij}\left(\overline{p} + \frac{\overline{\mathbf{B}}^2}{2\mu_0}\right) - \frac{1}{\mu_0}\overline{B}_i\overline{B}_j - \overline{\sigma}_{ij}, \tag{2.8}$$

$$\overline{\Pi}_{ij}^{(f)} = \overline{\rho}\left(\overline{u_i'u_j'}\right) + \delta_{ij}\left(\frac{\overline{\mathbf{B}'^2}}{2\mu_0}\right) - \frac{1}{\mu_0}\overline{B_i'B_j'}. \tag{2.9}$$

Here the fluctuations in hydrostatic pressure were neglected since we are considering a low Mach number regime. Now, the momentum equation for the mean flow is given by:

$$\overline{\rho}\frac{\partial\overline{\mathbf{u}}}{\partial t} = -\nabla\cdot\left(\overline{\Pi}^{(m)} + \overline{\Pi}^{(f)}\right) + \overline{\rho}\mathbf{g}. \tag{2.10}$$

A scale separation of the magnetic field into large-scale and turbulent components is also needed to obtain the averaged equation for the magnetic field. Consider the magnetic induction equation without dissipative effects:

$$\frac{\partial\mathbf{B}}{\partial t} = \nabla\times\left(\mathbf{u}\times\mathbf{B}\right). \tag{2.11}$$

Averaging eq. (2.11), and introducing the scale separation, $\mathbf{B} = \overline{\mathbf{B}} + \mathbf{B}'$, leads to:

$$\frac{\partial\overline{\mathbf{B}}}{\partial t} = \nabla\times\left(\overline{\mathbf{u}}\times\overline{\mathbf{B}} + \overline{\mathbf{u}'\times\mathbf{B}'}\right), \tag{2.12}$$

where the properties of the Reynolds averages, $\overline{\phi_i\overline{\beta}_j} = \overline{\phi}_i\overline{\beta}_j$ and $\overline{\phi'}_i = 0$, were considered. The term, $\overline{\mathbf{u}' \times \mathbf{B}'}$ is the mean electromotive force produced by the turbulent correlations of the flow and the magnetic field. For non-rotating systems, it is usual to take the closure, $\overline{\mathbf{u}' \times \mathbf{B}'} = -\eta_t \nabla \times \overline{\mathbf{B}}$, leading to (Brandenburg et al., 2014) [3]:

$$\frac{\partial \overline{\mathbf{B}}}{\partial t} = \nabla \times \left(\overline{\mathbf{u}} \times \overline{\mathbf{B}} - \eta_t \nabla \times \overline{\mathbf{B}} \right), \tag{2.13}$$

where η_t is the turbulent magnetic diffusivity. To close the set of MHD equations, the mass conservation and divergence-free condition of $\mathbf{B}$ are considered (See section 2.1.3).

2.1.2 Turbulence effects on Lorentz force

From equation (2.2) it can be seen that the isotropic part of the Maxwell stress tensor contributes to the total pressure of the system with the term $\mathbf{B}^2/2\mu_0$. In a similar way, the Mean Maxwell Stress Tensor (MMST) contributes to the total mean pressure with the term $\overline{\mathbf{B}}^2/2\mu_0$ (See eq. (2.8)). However, turbulent scales can modify the effective mean Lorentz force, i.e., the total mean pressure as well. To analyze the effect of turbulence on the mean Lorentz force we follow the approach presented in Kleeorin et al. (1996) and Rogachevskii & Kleeorin (2007). Lets consider first the turbulent Reynolds and Maxwell stress tensors denoted by $\sigma_{ij}^{(\nu)}$ and $\sigma_{ij}^{(m)}$, respectively:

$$\sigma_{ij}^{(\nu)} = \overline{\rho} \left(\overline{u_i' u_j'} \right), \tag{2.14}$$

$$\sigma_{ij}^{(m)} = \delta_{ij} \left(\frac{\overline{\mathbf{B}'^2}}{2\mu_0} \right) - \frac{1}{\mu_0} \overline{B_i' B_j'}. \tag{2.15}$$

Notice that $\overline{\Pi}_{ij}^{(f)} = \sigma_{ij}^{(\nu)} + \sigma_{ij}^{(m)}$ (see eq. (2.9)). The simplified case of isotropic and homogeneous turbulence will be considered to illustrate how the turbulent fluctuations in the magnetic field can modify the mean Lorentz force, i.e., the total mean pressure. The isotropic turbulence condition implies that:

$$\overline{B_i' B_j'} = \frac{\overline{\mathbf{B}'^2}}{3} \delta_{ij}, \tag{2.16}$$

[3] In this case the time scale of convection is much smaller than the time scale of rotation (30 days), i.e., the dynamics of convection do not care about the rotation of the system.

$$\overline{\rho}\left(\overline{u_i' u_j'}\right) = \overline{\rho}\frac{\overline{\mathbf{u}'^2}}{3}\delta_{ij}. \tag{2.17}$$

Therefore, the turbulent stress tensors can be written as:

$$\sigma_{ij}^{(m)} = \frac{\overline{\mathbf{B}'^2}}{6\mu_0}\delta_{ij} = \frac{W_m}{3}\delta_{ij}, \tag{2.18}$$

$$\sigma_{ij}^{(\nu)} = \overline{\rho}\frac{\overline{\mathbf{u}'^2}}{3}\delta_{ij} = \frac{2W_k}{3}\delta_{ij}, \tag{2.19}$$

where W_m and W_k are the turbulent magnetic and kinetic energy densities, respectively. These turbulent tensors can be written in terms of the magnetic and hydrodynamic turbulent pressures, p_m and p_ν ($\sigma_{ij}^{(m)} = p_m\delta_{ij}$ and $\sigma_{ij}^{(\nu)} = p_\nu\delta_{ij}$). Thus, substitution of equations (2.18) and (2.19) into the total turbulent pressure, $p_t = p_\nu + p_m$, leads to the state equation for isotropic turbulence:

$$p_t = \frac{W_m}{3} + \frac{2W_k}{3}. \tag{2.20}$$

Another equation for the temporal evolution of the total turbulent energy density, $W_T = W_m + W_k$, for isotropic and homogeneous turbulence in the presence of mean magnetic field $\overline{\mathbf{B}}$ is required. It is given by (Kleeorin et al. (1989), Kleeorin et al. (1996)):

$$\frac{\partial W_T}{\partial t} = I_T - \frac{W_T}{\tau_0} + \eta_t(\nabla\times\overline{\mathbf{B}})^2, \tag{2.21}$$

where τ_0 is the correlation time corresponding to the largest scale of turbulent motions l_0, also known as integral lengthscale (see Chapter 3) and I_T is the source of turbulent energy. Here, the mean magnetic field is prescribed. The solution of eq. (2.21) for a time-independent source I_T is given by:

$$W_T = W_T^0\exp\left(-t/\tau_0\right) + \tau_0\left[I_T + \eta_t(\nabla\times\overline{\mathbf{B}})^2\right]\left[1-\exp\left(-t/\tau_0\right)\right], \tag{2.22}$$

with $W_T^0 = W_T(t=0)$. Now, it is convenient to define the parameter, $\beta_{eq} = |\overline{\mathbf{B}}|/B_{eq}$, which is a measure of the relative strength of the magnetic field with respect to an equipartition magnetic field defined as:

$$\frac{\mathbf{B}_{eq}^2}{2\mu_0} = \frac{1}{2}\overline{\rho}\overline{\mathbf{u}_0'^2}, \tag{2.23}$$

where $\mathbf{u}_0'$ is the turbulent flow velocity in the absence of large-scale external magnetic field. Then, we consider the regime, $\beta_{eq} \ll 1$, and we take a mean magnetic field for which its characteristic dimension, L_B, is larger than the integral lengthscale of the turbulent motions, i.e., $L_B \gg l_0$. Under these considerations, it can be shown that the ratio of the two turbulent sources, I_N/I_T, with $I_N = \eta_t(\nabla \times \overline{\mathbf{B}})^2$ is of the order of (Kleeorin et al., 1996):

$$\frac{I_N}{I_T} \simeq \left(\frac{l_0}{L_B}\right)^2 \frac{\overline{\mathbf{B}}^2}{\overline{\rho}\overline{U_0'^2}} << 1. \tag{2.24}$$

This implies that the magnetic source, I_N, can be neglected in the limit where $\beta_{eq} \ll 1$ and $L_B \gg l_0$ (note that for the case of uniform mean magnetic field $l_0/L_B \to 0$). Then, the formula (2.22) reduces to $W_T \simeq \tau_0 I_T$ for $t >> \tau_0$, i.e., the total turbulent energy density of fully developed isotropic and homogeneous MHD turbulence is conserved:

$$W_T = W_k + W_m = const. \tag{2.25}$$

Combining eqs. (2.20) and (2.25) leads to a formula for the turbulent pressure variations in terms of the turbulent magnetic energy density variations:

$$\delta p_t = -\frac{1}{3}\delta W_m. \tag{2.26}$$

Physically, this means that the generation of magnetic fluctuations ($\delta W_m > 0$) implies negative values of δp_t, i.e., a decline in the total turbulent pressure. This result can be extended to anisotropic turbulence (Rogachevskii & Kleeorin, 2007):

$$\delta p_t = -\frac{2 + 3A_N}{3(2 + A_N)}\delta W_m, \tag{2.27}$$

with A_N being a measure of the turbulence anisotropy (A_N vanishes for isotropic turbulence). In the regime where $\beta_{eq} \ll 1$, the magnetic fluctuations, $\overline{B'^2}$, in the presence of a mean magnetic field can be expanded as a series in $\overline{\mathbf{B}}^2$ (Kleeorin et al., 1989):

$$\overline{\mathbf{B}'^2} = \overline{\mathbf{B}_0'^2} + a_m(\overline{\mathbf{B}}, R_m)\overline{\mathbf{B}}^2 + O(\overline{\mathbf{B}}^4/(\overline{\rho}\overline{\mathbf{u}_0'^2})), \tag{2.28}$$

where, the subscript 0 means quantities taken from the steady state without mean magnetic field. The coefficient a_m depends only on the mean magnetic field and the magnetic Reynolds number, $Rm = UL/\lambda$, where U and L are the characteristic velocity

and lengthscale of the flow, and λ is the so-called magnetic difussivity (Davidson, 2015). We take the magnetic energy and turbulent pressure variations as, $\delta W_m = (\overline{\mathbf{B}'^2} - \overline{\mathbf{B}_0'^2})/2\mu_0$ and $\delta p_t = p_t - p_{0t}$, respectively. Then, using equations (2.26) and (2.28) leads to:

$$p_t = p_{0t} - \frac{1}{3}\left(\frac{a_m}{2\mu_0}\right)\overline{\mathbf{B}}^2 = p_{0t} - q_p\frac{\overline{\mathbf{B}}^2}{2\mu_0}, \tag{2.29}$$

where the coefficient $q_p = (a_m/3)$. Next, notice that substituting eq. (2.29) in the total pressure results in:

$$P = \overline{P} + \frac{\overline{\mathbf{B}}^2}{2\mu_0} + p_t = \overline{P} + p_{0t} + (1 - q_p)\frac{\overline{\mathbf{B}}^2}{2\mu_0}. \tag{2.30}$$

In eq. (2.30) the term that depends on the mean magnetic field is called the effective magnetic pressure

$$P_m = (1 - q_p)\frac{\overline{\mathbf{B}}^2}{2\mu_0}. \tag{2.31}$$

Finally, the effective mean Lorentz force is given by:

$$\overline{\rho}\overline{\mathbf{F}}_i^{(m)} = -\frac{1}{2\mu_0}\nabla_i\left[(1 - q_p)\overline{\mathbf{B}}^2\right]. \tag{2.32}$$

Equation (2.31) shows that for isotropic and homogeneous turbulence in the presence of a large-scale magnetic field, the effective magnetic pressure can be negative if $q_p > 1$. In the regime, $\overline{P} >> \overline{\mathbf{B}}^2/2\mu_0$, there can be conditions for which the effective magnetic pressure is negative while the total pressure remains positive. In the following section we will demonstrate that an instability develops when the effective magnetic pressure is negative. This instability can generate inhomogeneities in the magnetic field, i.e., magnetic flux concentrations that might be correlated to sunspot formation.

2.1.3 Growth rate of NEMPI for imposed vertical field

A general closure for the turbulent component of the momentum-stress tensor, $\overline{\Pi}_{ij}^{(f)}$, is given by (Rogachevskii & Kleeorin (2007), Käpylä et al. (2012), Käpylä et al. (2016)):

$$\Delta\overline{\Pi}_{ij}^{(f)} = \overline{\Pi}_{ij}^{(f,\overline{B})} - \overline{\Pi}_{ij}^{(f,0)} = \frac{1}{\mu_0}\left(q_s\overline{B}_i\overline{B}_j - \frac{1}{2}q_p\delta_{ij}\overline{\mathbf{B}}^2\right), \tag{2.33}$$

where, $\overline{\Pi}_{ij}^{(f,0)}$, is the turbulent momentum-stress tensor without the presence of a large-scale magnetic field, $\overline{\mathbf{B}}$. On the other hand, $\overline{\Pi}_{ij}^{(f,\overline{B})}$ is the corresponding momentum stress tensor when there is a large-scale magnetic field in the system. The coefficient q_p has the same interpretation as in eq. (2.31) and the coefficient q_s accounts for possible anisotropies of the turbulent correlations. Neglecting the anisotropies ($q_s = 0$), a substitution of (2.33) into the eq. (2.10) leads to:

$$\overline{\rho}\frac{\partial\overline{\mathbf{u}}}{\partial t} + (\overline{\mathbf{u}}\cdot\nabla)\,\overline{\mathbf{u}} = -\nabla\left(\overline{P} + (1-q_p)\frac{\overline{\mathbf{B}}^2}{2\mu_0}\right) + \frac{1}{\mu_0}\left(\overline{\mathbf{B}}\cdot\nabla\right)\overline{\mathbf{B}} + \overline{\rho}\mathbf{g}. \tag{2.34}$$

A consistent set of mean-field MHD equations can be obtained from eqs. (2.13) and (2.34) and applying scale separation on the mass conservation equation and the divergence free condition on the magnetic field:

$$\overline{\rho}\frac{D\overline{\mathbf{u}}}{Dt} = -\nabla\overline{P}_{tot} + \frac{1}{\mu_0}\left(\overline{\mathbf{B}}\cdot\nabla\right)\overline{\mathbf{B}} + \overline{\rho}\mathbf{g} \tag{2.35}$$

$$\frac{\partial\overline{\mathbf{B}}}{\partial t} = \nabla\times\left(\overline{\mathbf{u}}\times\overline{\mathbf{B}}\right) \tag{2.36}$$

$$\nabla\cdot(\overline{\rho}\overline{\mathbf{u}}) = 0 \tag{2.37}$$

$$\nabla\cdot\overline{\mathbf{B}} = 0, \tag{2.38}$$

where both large-scale and turbulent dissipative effects have been neglected. We linearize equations (2.35)-(2.38) around the equilibrium state: $\overline{\mathbf{u}}_0 = \mathbf{0}$, $\overline{\mathbf{B}}_0 = B_0\hat{\mathbf{k}}$, and adopt an isothermal state equation, $p = \rho c_s^2$, where, $c_s = \text{const}$, is the sound speed. In the absence of magnetic field the hydrostatic solution for the stratification is given by $\overline{\rho} = \rho_0\exp(-z/H_\rho)$, where $H_\rho = c_s^2/g$ is the density scale height. Then, the equations for the small perturbations are given by:

$$\frac{\partial\mathbf{u}'}{\partial t} = \frac{1}{\overline{\rho}}\left(\frac{1}{\mu_0}\left(\overline{\mathbf{B}}_0\cdot\nabla\right)\mathbf{B}' - \nabla P_m'\right) \tag{2.39}$$

$$\frac{\partial\mathbf{B}'}{\partial t} = \nabla\times\left(\mathbf{u}'\times\overline{\mathbf{B}}_0\right) \tag{2.40}$$

$$\nabla\cdot\mathbf{u}' = \frac{u_z'}{H_\rho} \tag{2.41}$$

$$\nabla\cdot\mathbf{B}' = 0. \tag{2.42}$$

An expression for the effective magnetic pressure perturbation, P'_m, is obtained by performing a Taylor series expansion of P_m around its corresponding value in the equilibrium state, P^0_m:

$$P'_m = 2B_0 B'_z \left(\frac{dP_m}{d\overline{B}^2}\right)_{\overline{B}=B_0} + \cdots . \tag{2.43}$$

It is usual to define the normalized effective magnetic pressure, $\wp_m$, as:

$$\wp_m = \frac{\mu_0}{B^2_{eq}} P_m = \frac{1}{2}(1 - q_p)\beta^2_{eq}, \tag{2.44}$$

where, B_{eq}, is defined in eq. (2.23) and $q_p = q_p(\beta_{eq})$ (see eqs. 2.28 and 2.29). Substituting eq. (2.44) and the vertical field condition, $\overline{\mathbf{B}}_0 = B_0\hat{\mathbf{k}}$, into eq. (2.39) gives for the perturbative momentum equation

$$\frac{\partial \mathbf{u}'}{\partial t} = \frac{B_0}{\overline{\rho}\mu_0}\left[\partial_z \mathbf{B}' - 2\left(\frac{d\wp_m}{d\beta^2_{eq}}\right)_{\beta_0} \nabla B'_z\right]. \tag{2.45}$$

To reduce the number of variables we consider a second time derivative over equation (2.40), which leads to:

$$\frac{\partial^2 \mathbf{B}'}{\partial t^2} = \nabla \times \left(\frac{\partial \mathbf{u}'}{\partial t} \times \overline{\mathbf{B}}_0\right), \tag{2.46}$$

and replace eqs. (2.45) and (2.42) into eq. (2.46). Then, the z-component of the resulting expression is:

$$\frac{\partial^2 B'_z}{\partial t^2} = \frac{2B^2_0}{\overline{\rho}\mu_0}\left(\frac{d\wp_m}{d\beta^2_{eq}}\right)_{\beta_0} \left(\partial^2_x + \partial^2_y\right) B'_z + \frac{B^2_0}{\overline{\rho}\mu_0}\partial^2_z B'_z. \tag{2.47}$$

Now we look for solutions of eq. (2.47) in the form:

$$B'_z(x, y, z) = f(z) \exp(\lambda t) \exp[i(k_x x + k_y y)]. \tag{2.48}$$

Substitution of eq: (2.48) into eq. (2.47) results in:

$$\lambda^2 = -2v^2_a \left(\frac{d\wp}{d\beta^2_{eq}}\right)_{\beta_0} k^2_\perp + v^2_a \frac{f''(z)}{f(z)}, \tag{2.49}$$

where $v_a(z) = B_0/\sqrt{\overline{\rho}\mu_0}$ is the Alfvén speed and $k_\perp$ is the vertical wavenumber. For $v_a^2 f''(z)/f(z) \ll 1$ (we assume that $f(z)$ changes smoothly such that the term with its second derivative can be neglected), the growth rate of the instability is given by:

$$\lambda = v_a \sqrt{-2 \left(\frac{d\wp}{d\beta_{eq}^2} \right)_{\beta_0}} k_\perp. \tag{2.50}$$

Equation (2.50) shows that for negative values of the derivative of the normalized effective magnetic pressure an instability develops. This result agrees with NEMPI growth rates previously found by Kemel et al. (2013) and Brandenburg et al. (2014).

2.2 State of art of NEMPI

2.2.1 First numerical hints of NEMPI

Theoretically, the effect of small-scale magnetic fluctutations over the mean Lorentz force was first recognized by Kleeorin et al. (1989). It was shown the possibility of a sign reversal in the effective magnetic pressure, i.e., the appearance of an instability that could generate inhomogeneities of the large-scale magnetic field. Later, Brandenburg et al. (2010) observed for the first time a sign reversal in the Lorentz Force in a DNS with forced turbulence[4]. In section 2.1.3 we found that the total turbulent pressure in eq. (2.29) was obtained by using the Taylor expansion of the magnetic energy fluctuations in eq. (2.28) (procedure valid only for the case of isotropic turbulence and for $\overline{B} \ll B_{eq}$). Following Brandenburg et al. (2010) a more general parameterization of the magnetic energy fluctuations requires additional coefficients different from q_p, to account for possible anisotropies generated in the model. To that end, consider the turbulent part of the stress tensor, $\Pi_{ij}^{(f)}$, as given in eq. (2.9). In the absence of an external mean magnetic field this tensor has a value denoted by $\Pi_{ij}^{(f,0)}$. On the other hand, if a mean magnetic field is imposed over the system, the turbulent stress tensor will have a different value, $\Pi_{ij}^{(f,\overline{B})}$. Therefore, all the energy fluctuations due to the presence of the external mean magnetic field, $\overline{B}$, can be represented by the difference $\Delta\Pi_{ij}^{(f)} = \Pi_{ij}^{(f,\overline{B})} - \Pi_{ij}^{(f,0)}$. According to Rogachevskii & Kleeorin (2007), in this case the difference $\Delta\Pi_{ij}^{(f)}$ can be parameterized as:

$$\Delta\Pi_{ij}^{(f)} = \frac{1}{\mu_0} \left(q_s \overline{B}_i \overline{B}_j - \frac{1}{2} q_p \delta_{ij} \overline{B}^2 \right), \tag{2.51}$$

[4]The term forced turbulence refers to simulations in which turbulence is artificially generated with an stochastic function that is added to the equations of motion. This kind of simulations allow to reach a high Reynolds number with less computational resources.

such that the corresponding generalization of the effective mean Lorentz force given in (2.32) is now expressed as:

$$\overline{\rho}\overline{F}_i^{(m)} = -\frac{1}{2\mu_0}\nabla_i\left[(1-q_p)\overline{B}^2\right] + \frac{1}{\mu_0}\overline{B}\cdot\nabla\left[(1-q_s)\overline{B}_i\right]. \tag{2.52}$$

In Fig. 2.1 are shown the results from the DNS performed by Brandenburg et al. (2010). There it can be seen that for mean magnetic fields small enough compared with the corresponding equipartition magnetic field, B_{eq}, the coefficients q_p and q_s show values considerably greater than unity. Therefore, negative values of both, the magnetic pressure and magnetic tension are obtained.

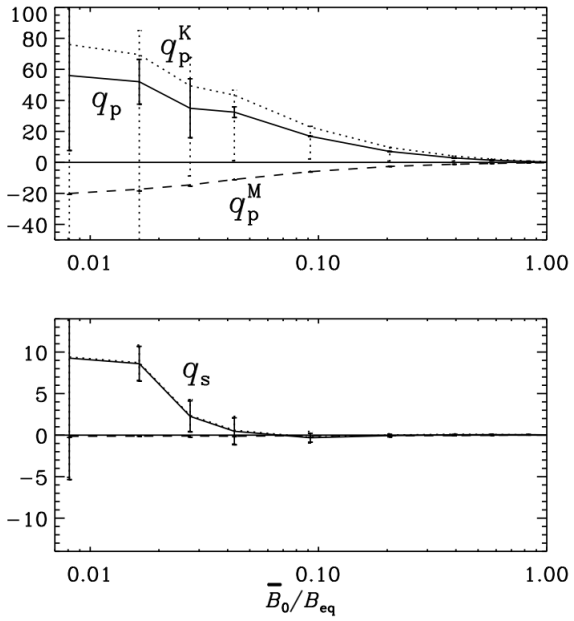

FIGURE 2.1: Coefficients q_p and q_s obtained from the DNS performed by Brandenburg et al. (2010) ($Re = 180$ and $R_M = 45$). The coefficients q_p^K and q_p^M represent the hydrodynamic and magnetic parts of q_p ($q_p^K + q_p^M = q_p$), i.e., they represent separately the effects of the mean magnetic field on the turbulent Reynolds and Maxwell stresses.

2.2.2 Isothermal DNS with forced turbulence

Brandenburg et al. (2011) presented the first numerical demonstration of the instability triggered by the sign reversal in the Lorentz force due to the small-scale fluctuations. DNS of MHD turbulence in an isothermal atmosphere showed the appearance of magnetic flux concentrations from an initially uniform horizontal magnetic field, were the forced turbulence is generated by a forcing function made of random, white-in-time, plane, non-polarized waves with an average wavenumber $k_f = 15k_1$, where $k_1 = 2\pi/L_z$ is the lowest wavenumber corresponding to the vertical dimension of the domain.

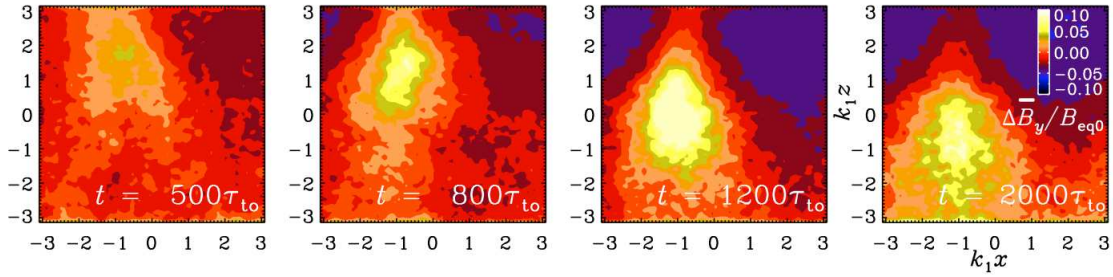

FIGURE 2.2: $(\overline{B}_y - B_0)/B_{eq0}$ in the x-z plane for $R_M = 6$ and $B_0/B_{eq0} = 0.05$. Time is in units of τ_{to} (Taken from Brandenburg et al. (2011))

Fig. 2.2 shows a magnetic structure termed as a descending "potato-sack". The time in Fig. 2.2 is given in terms of the eddy turnover time, $\tau_{to} = (u_{rms}k_f)^{-1}$. During the first 500 turnover times, flux concentrations form near the surface. Afterwards, the location of the peak magnetic field descends gradually, characterized by the "potato-sack" structure shown in the figure.

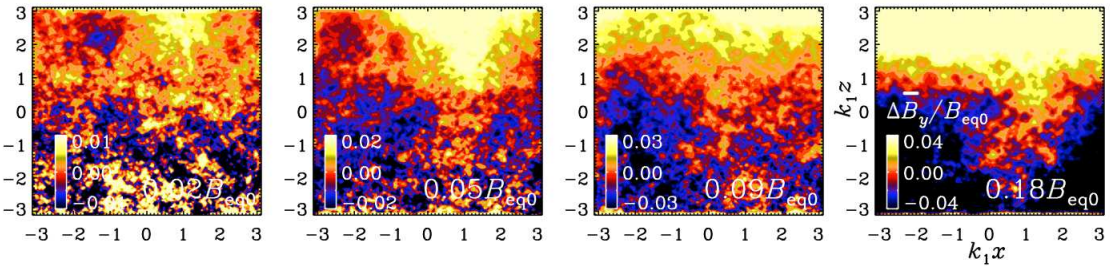

FIGURE 2.3: $(\overline{B}_y - B_0)/B_{eq0}$ in the x-z plane for $R_M = 36$ and $B_0/B_{eq0} = (0.02, 0.05, 0.09, 0.18)$ from left to right. (Taken from Brandenburg et al. (2011))

Fig. 2.3 shows $(\overline{B}_y - B_0)/B_{eq0}$ in the x-z plane (the over line means average over the y direction) at a time interval $\Delta t \sim 800\tau_{to}$. Flux concentrations are formed for a certain range of the imposed magnetic field strengths, $(0.02 < B_0/B_{eq0} < 0.2)$. For stronger imposed magnetic field, the flux concentrations are less evident. Even though negative values of the effective magnetic pressure have been found in DNS, a direct connection between magnetic structures and the action of NEMPI is still unclear (Kemel et al. (2012); Käpylä et al. (2012), Kemel et al. (2013)).

2.2.3 Flux concentrations in polytropic atmospheres

The work discussed above was performed in an isothermal atmosphere, where the density scale height is constant. However, it is reasonable to analyze a more realistic stratification (stellar convection has a density stratification with variable density scale height). In the DNS of forced turbulence in a polytropic atmosphere performed by Losada et al.

(2014), they found magnetic flux concentrations reaching super-equipartition values for the case of external vertical magnetic fields (See Fig. 2.4).

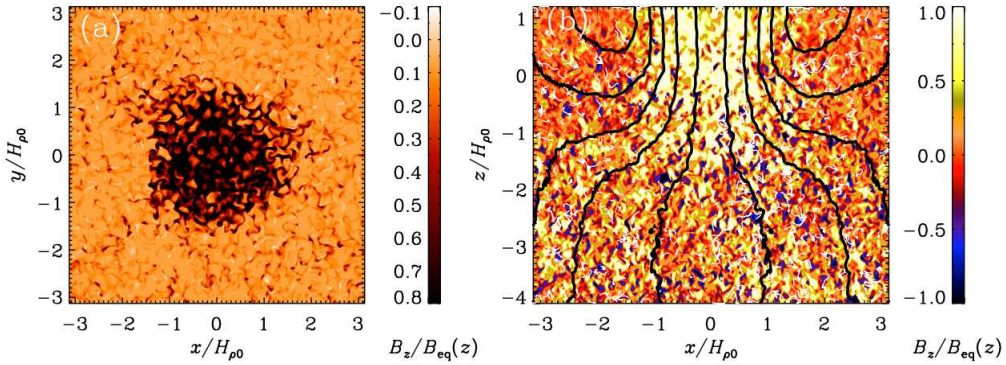

FIGURE 2.4: Cuts of $B_z/B_{eq}(z)$ in (a) the xy plane at the top boundary ($z/H_{\rho 0} = 1.2$) and (b) the xz plane through the middle of the spot at $y = 0$ for $\beta_0 = 0.05$ (Taken from Losada et al. (2014))

For horizontal magnetic fields the "potato-sack" effect was observed in agreement with the isothermally stratified DNS. Since these simulations considered the influence of a homogeneous gravitational field, g_0, necessary to construct the polytropic atmosphere, a more general parameterization of the stress tensor variations $\Delta\Pi_{ij}^{(f)}$ is required in the presence of a horizontal magnetic field, $\overline{\mathbf{B}}$:

$$\Delta\Pi_{ij}^{(f)} = \frac{1}{\mu_0}\left(q_s\overline{B}_i\overline{B}_j - \frac{1}{2}q_p\delta_{ij}\overline{B}^2 - q_g\hat{g}_i\hat{g}_j\overline{B}^2\right), \tag{2.53}$$

where $\hat{g}_i$ is the i-th component of the unit vector in the direction of the gravitational field. Note the appearance of the additional turbulent coefficient q_g. For vertical fields eq. 2.51 is recovered. A plot of the mean effective magnetic pressure as a function of β_{eq} (denoted as β in the plot) is shown in fig. 2.5, where $\gamma = c_p/c_\nu$ is the ratio of the specific heats at constant pressure and constant density. The different values of γ account for the different polytropic stratifications considered.

It is important to note that the structure of the flux concentrations in the case of vertical magnetic field is entirely different from the horizontal magnetic field case. While in the horizontal magnetic field case the instability still leads to "potato-sack" down-flows, in the vertical magnetic field case the flux concentrations do not sink and remain in the surface layers.

For polytropic atmospheres NEMPI develops in the uppermost layers, provided that the mean magnetic field is not too strong. The main result, however, is that the magnetic structure does not sink. (See in fig. 2.4). This case supports the hypothesis of NEMPI as a viable mechanism for spontaneous formation of magnetic spots in the surface layers.

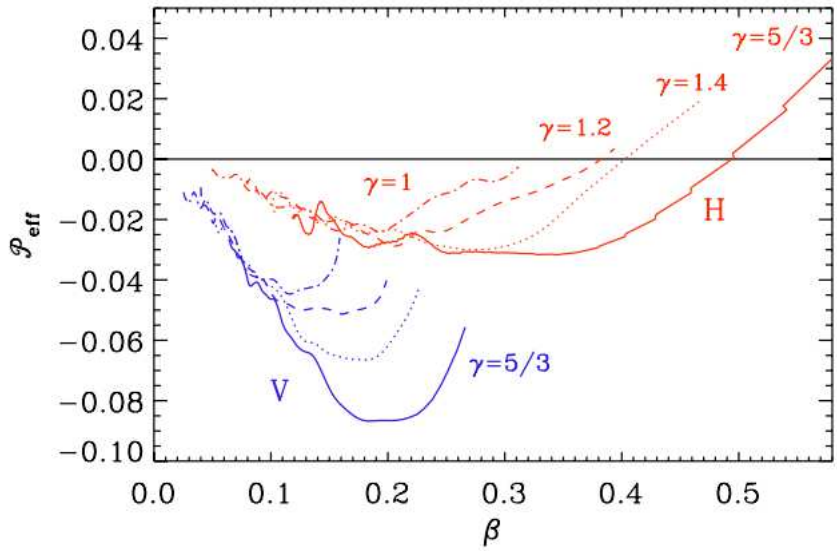

FIGURE 2.5: Effective magnetic pressure, as a function of β_{eq}, obtained from DNS in a polytropic layer with different γ for horizontal (H, red curves) and vertical (V, blue curves) magnetic fields (Taken from Losada et al. (2014)).

2.2.4 Magnetic flux concentrations in convection simulations

High-resolution local convection simulations performed by Käpylä et al. (2016) revealed super-equipartition magnetic flux concentrations near the surface of the domain (see fig. 2.6). Vertical and horizontal uniform magnetic field at different strengths were imposed on the simulations. They calculate the effective magnetic pressure by using eq. (2.53). Even though the results showed negative contributions to the effective magnetic pressure, the growth of the magnetic structures was not exponential as expected. The results were more consistent with a linear growth of the magnetic field, suggesting that in this case the formation of magnetic structures is related to tangling of the magnetic field by large-scale convection.

The simulations of Käpylä et al. (2016) for vertical and horizontal imposed magnetic fields led to inconclusive results about the relevance of NEMPI in the formation of sunspots. It seems that their setups were unable to excite NEMPI possibly due to the fact that the scale separation between the size of the system and the turbulent scales was insufficient. Therefore the relevance of NEMPI as the responsable for the formation of sunspot-like structures in convection simulations remains unclear.

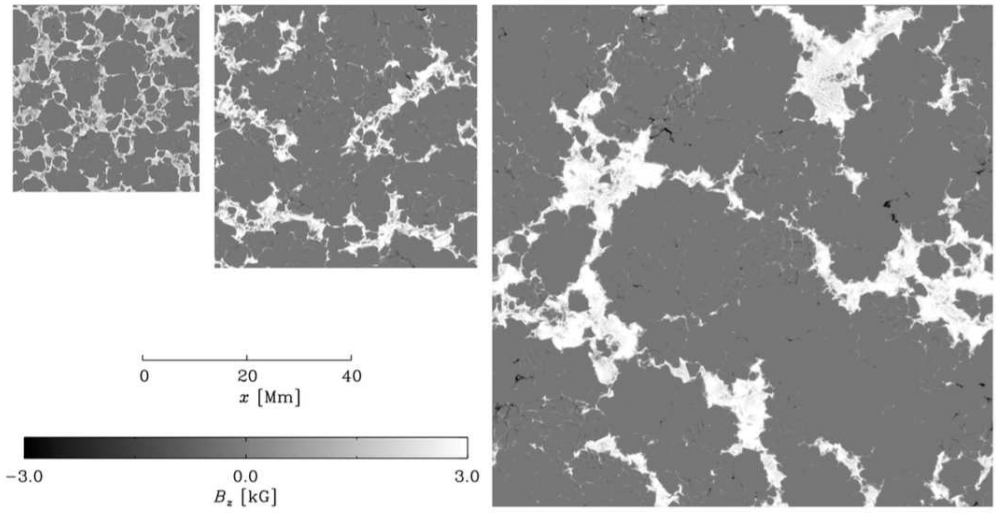

FIGURE 2.6: Horizontal slices of B_z near the top surface for different box sizes where convection is interacting with an imposed vertical magnetic field. The strength of the imposed vertical field is different in each simulation. The physical scale is shown in the legend (Taken from Käpylä et al. (2016)).

Chapter 3

Numerical simulation of turbulent convection

The phenomenon of sunspot formation is an MHD problem associated with turbulent convection at high Re (Re $> 10^6$ for the solar case). Numerical simulations of turbulent convection are in general a complex endeavour due to the wide range of scales that turbulence encompasses. Kolmogorov's theory of turbulence shows that the typical scale of the smallest turbulent eddies in a complex flow, so called Kolmogorov scale, is of the order of $Re^{-3/4}$. Hence, the larger the Reynolds number, the smaller the Kolmogorov scale, and the wider the range of turbulent scales. In terms of numerical resolution this implies that a simulation of a turbulent flow requires a high number of meshpoints to resolve from the Kolmogorov to the integral scales (see section 3.1 below).

3.1 Direct Numerical Simulation (DNS)

A numerical simulation that captures all the scales of a turbulent flow is called a direct numerical simulation or DNS, as described before in Chp. 1. This requirement leads to certain constraints. Thus, any numerical scheme for DNS results to be very expensive in terms of computational power. Before introducing the numerical constraints necessary for a DNS to capture all turbulent scales, we briefly discuss the so-called Richardson energy cascade process and the Kolmogorov theory.

3.1.1 Richardson cascade

Turbulence can be considered as a hierarchy of structures with different sizes (called eddies). These eddies can be thought as vortical structures localized within a certain

length, often called the typical eddy size or eddy lengthscale. A given eddy with lengthscale l, has a corresponding velocity, $u(l)$, and a typical timescale, $\tau(l)$. The typical lengthscale of the largest turbulent eddies is called the integral lengthscale, l_0, with u_0 and τ_0 the associated velocity and time scales, respectively. The integral velocity and length scales are comparable to the typical scales of the large-scale flow ($l_0 \sim L$ and $u_0 \sim u$). Thus, the Reynolds number relative to the integral lengthscale, $Re_0 = l_0 u_0/\nu$, is of the same order as the Reynolds number of the large-scale flow ($Re_0 \sim Re$).

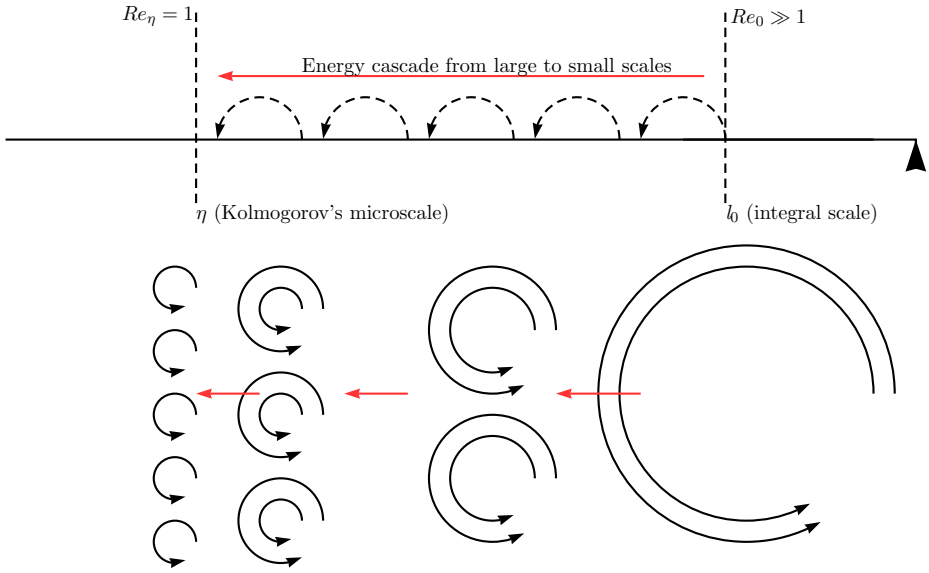

FIGURE 3.1: Energy cascade as envisaged by Richardson. The smallest scale of the energy cascade, at which viscosity is important, is called the Kolmogorov microscale. The large scale at which energy is injected into the system is called the integral scale.

In the 1920s Lewis F. Richardson introduced the concept of energy cascade for turbulent flows. Richardson proposed that eddies within a certain range of scales are unstable, and break down into smaller eddies. Thus, the energy is transferred from the largest to these smaller convective structures. These smaller eddies follow the same breaking process originating yet small-scale motions until a certain scale at which the eddies are stable. This picture of energy transfer from the large to the small scales is known as the energy cascade (see Fig. 3.1). However, the scale at which this cascade stops has a Reynolds number small enough for the viscous process to be effective in dissipating the eddies (Pope, 2000). As it will be shown in the next section this scale is called the Kolmogorov microscale, η. The Reynolds number associated to this scale is of the order of unity.

3.1.2 Kolmogorov microscales

In general, at the integral scale (also called injection scale), the eddies have an anisotropic behaviour because of the boundary conditions over the flow. However, according to

Kolmogorov, this anisotropic bias of the integral lengthscales is lost through the scale reduction process of the energy cascade such that for sufficiently high Re, and for small enough eddy lengthscales, the statistics of the turbulent motions are isotropic and homogeneous. This is known as the Kolmogorov's hypothesis of local isotropy which is stated as follows:

Kolmogorov's Hypothesis of local isotropy: At sufficiently high Reynolds number, the small scale turbulent motions ($l << l_0$) are statistically isotropic.

The term local refers to isotropy only at small scales. In this context it is defined a critical lengthscale $l_{EI} \simeq l_0/6$ that works as a boundary between the isotropic and the anisotropic scales along the cascade (Pope, 2000). Kolmogorov argued that the information concerning the eddy geometry, as well as boundary conditions, is also lost through the energy cascade. This implies that the statistics of small scale motions are, in a sense, universal for every flow at high Reynolds number.

It is necessary to identify the parameters that determine this statistically universal state for the small turbulent scales. Within the energy cascade ($l < l_{EI}$) the two important processes are the energy transfer to successively smaller scales and the viscous dissipation. Therefore, it is possible to say that the important parameters are the energy transfer rate, at which the small eddies receive energy from the large ones (T_{EI}), and the kinematic viscosity ν. The energy dissipation rate at the end of the cascade (denoted by ϵ) is nearly equal to the energy transfer rate, i.e., $\epsilon \sim T_{EI}$ (Pope, 2000). This leads to the second hypothesis of Kolmogorov about the parameters that determine the universal statistics for every turbulent flow:

Kolmogorov's First similarity hypothesis: For every turbulent flow at sufficiently high Reynolds number, the statistics of the small-scale motions ($l << l_0$) have a universal form determined uniquely by ν and ϵ

The range of isotropic scales is often called the *Universal equilibrium range*. In this range the statistics should be the same for any flow at high Re, and uniquely defined by the parameters ϵ and ν. Related to these parameters there are unique length, velocity and time scales that can be calculated from a simple dimensional analysis:

$$\eta = \left(\nu^3/\epsilon\right)^{1/4} \tag{3.1}$$

$$u_\eta = (\epsilon\nu)^{1/4} \tag{3.2}$$

$$\tau_\eta = (\nu/\epsilon)^{1/2} \tag{3.3}$$

These three parameters are called the Kolmogorov microscales. It is easy to see that they satisfy $Re_\eta = \eta u_\eta/\nu = 1$. This means that the Kolmogorov scale η represents the smallest scale at which the cascade ends, i.e., the scale at which viscous dissipation takes place. In a few words, within the *Universal equilibrium range* the flow receives energy from eddies within the integral lengthscale, l_{EI}, at a rate, T_{EI}, and looses energy at a dissipation rate ϵ over the smallest eddies at the Kolmogorov scale (See Fig. 3.2).

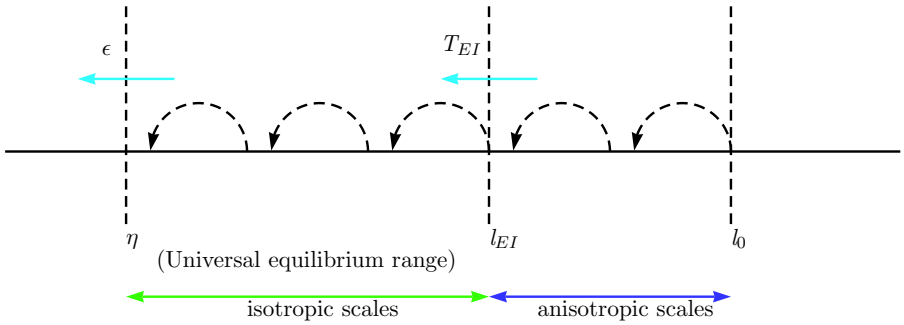

FIGURE 3.2: Energy cascade. The lengthscale l_{EI} serves as a separation between the isotropic and anisotropic scales. Energy is injected into the cascade at a rate T_{EI} and at the end of the cascade the energy is dissipated at a rate ϵ.

It can be shown that a reasonable scaling for the dissipation rate is given by $\epsilon \sim u_0^3/l_0$ (Pope, 2000). This relation is particularly useful to relate the Kolmogorov scales with the integral scales. Using the above scaling for the dissipation rate together with the flow Reynolds number, $Re = Lu/\nu$, it can be shown that:

$$\eta \sim l_0 Re^{-3/4} \tag{3.4}$$

$$u_\eta \sim u_0 Re^{-1/4} \tag{3.5}$$

$$\tau_\eta \sim \tau_0 Re^{-1/2} \tag{3.6}$$

3.1.3 Energy spectra and Kolmogorov $-5/3$ law

From (3.4) it can be seen that the ratio η/l_0 decreases with Re. This implies that for sufficiently high Reynolds numbers, there will be a range of scales, l, small enough compared with the integral scale, and yet large enough compared with η ($\eta \ll l \ll l_0$)

such that the influence of the viscosity over the dynamics of the eddies can be neglected. This leads to the third Kolmogorov Hypothesis:

Kolmogorov's Second similarity hypothesis: for every turbulent flow at sufficiently high Reynolds number, the statistics of the motions at scales l in the range ($l_0 \gg l \gg \eta$) has a universal form that is uniquely determined by ϵ and independent of ν.

This hypothesis separates the universal equilibrium range into two subintervals. At this point it is convenient to define a scale that limits this range separation. This limiting scale will be denoted by l_{DI}, where $l_{DI} = 60\eta$ (Pope, 2000). The range of scales that specifies the Kolmogorov's second similarity hypothesis is then given by $l_{DI} < l < l_{EI}$, and this is called the inertial subrange. The range of scales between η and l_{DI} is called the dissipation range (see Fig. 3.3).

With the above definitions it is possible to demonstrate the Kolmogorov's $-5/3$ law. To that end it is still necessary to make a spectral decomposition of the kinetic energy budget of the flow. This procedure is quite convenient since it allows the study of the energy distribution along the different scales that the turbulent flow encompasses. Thus, a lengthscale l has an associated wavenumber $k = 2\pi/l$. Then, the spectral kinetic energy distribution is defined as:

$$E(k,t) \equiv \int\int\int |\hat{u}(\vec{k'},t)|^2 \delta(|\vec{k'}| - k) d^3k' \tag{3.7}$$

Where the integration is done over the entire wavenumber space, and $\hat{u}$ denotes the three-dimensional Fourier transform of the flow velocity field. The spectral kinetic energy distribution is normalized such that:

$$\int_0^\infty E(k)dk = \frac{1}{2}\langle u^2 \rangle, \tag{3.8}$$

where the brackets denote volume averaging. Notice that eq. (3.8) shows that $E(k)$ can be interpreted as the kinetic energy per unit mass per wavenumber. It can be shown from the Kolmogorov's second similarity hypothesis that, within the inertial subrange, the spectral kinetic energy distribution has the following scaling (Pope, 2000):

$$E(k) = C\epsilon^{2/3}k^{-5/3} = Ak^{-5/3}. \tag{3.9}$$

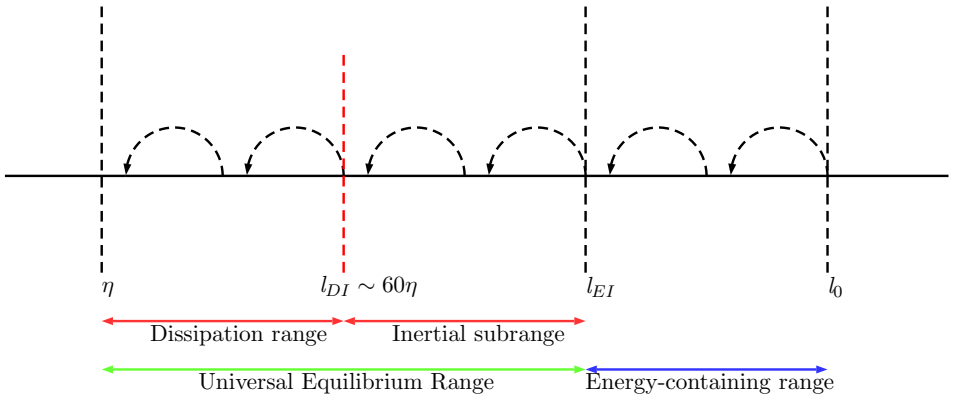

FIGURE 3.3: Full representation of the Energy cascade. The lengthscale l_{DI} serves as a separation between the Inertial subrange and the dissipation range. Within the inertial subrange the universality of the statistics is uniquely determined by ϵ. (The proportions are exaggerated in the figure for illustration purposes. Thus, they do not represent accurately the relative sizes of each of the ranges along the cascade.)

Eq. (3.9) represents the so-called Kolmogorov's $-5/3$ law. It shows how the spectral kinetic energy distribution within the inertial subrange is uniquely defined by the dissipation rate ϵ as a parameter, with a $-5/3$ power dependence on the wavenumber. A graphical representation of a typical turbulent energy spectrum is shown in Fig. 3.4 (in logarithmic scales). In the figure, the already discussed lengthscales, $l_0, l_{EI}, l_{DI}, \eta$, have corresponding wavenumbers, $k_{l_0}, k_{l_{EI}}, k_{l_{DI}}, k_\eta$.

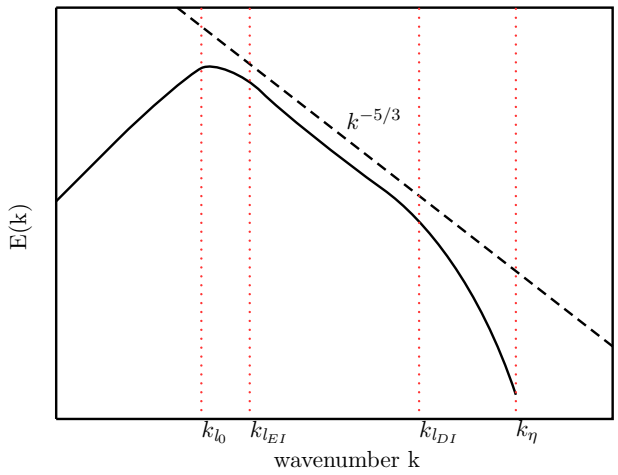

FIGURE 3.4: Typical energy spectrum for a high Reynolds number flow in logarithmic scale. The spectra within the inertial subrange should satisfy the $-5/3$ Kolmogorov's law for high Reynolds number.

3.1.4 Numerical resolution constraints

In the previous sections it was discussed the physical nature of turbulence in terms of the Richardson energy cascade. It was also mentioned that a DNS has to capture all the

turbulent scales of the simulated flow. In terms of the Kolmogorov theory this means that for a given discrete grid of resolution Δx one necessary condition is:

$$\Delta x \leq \eta \sim l_0 Re^{-3/4}. \tag{3.10}$$

That is, the grid resolution has to be smaller than the local Kolmogorov lengthscale. Higher Reynolds number flows will require a finer grid resolution (see Fig. 3.5 for a simplified example of a good grid resolution in a DNS). Given a homogeneous 3D mesh with equal resolution along the three axes, Δx, the number of points in the mesh is given by $N = (L_{box}/\Delta x)^3$, where L_{box} is the domain length (in this case a regular box). Therefore, the number of meshpoints required to satisfy eq. (3.10) is given by:

$$N \geq \left(\frac{L_{box}}{l_0}\right)^3 Re^{9/4} \sim Re^{9/4} \tag{3.11}$$

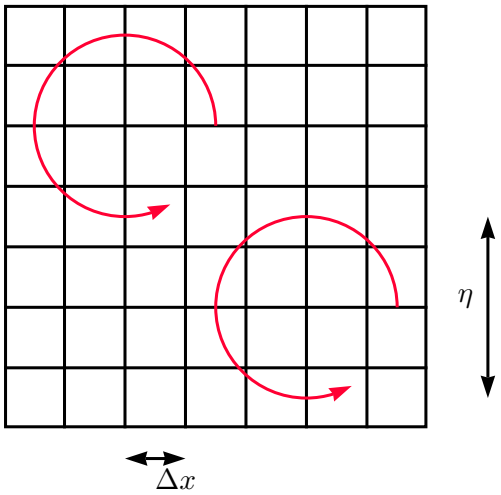

FIGURE 3.5: Graphical representation of a 2D resolution sufficiently good ($\Delta x \leq \eta$) to capture the Kolmogorov scale of a certain turbulent flow.

Eq. (3.11) reveals the main reason why DNS are unachievable for high Reynolds number flows. As the number of meshpoints in a DNS increases with the Reynolds number, it becomes more expensive to simulate high Re turbulent flows. Kaneda et al. (2003) performed the largest DNS so far using the Earth Simulator supercomputer (ES) with a resolution of 4096^3, attaining Reynolds numbers of the order of up to 10^3. Real flows in engineering and astrophysics typically have Reynolds numbers larger than 10^6. Thus, it is understandable that DNS of turbulent flows remain unreachable with the available computational power.

It is important to notice that the condition given by eq. (3.10) is not always sufficient to have a physically acceptable DNS. Condition (3.10) guarantees a finite in time solution but not necessarily physically correct. In convection simulations, linear fixed-grid algorithms can guarantee positivity-preserving solutions only if (Oran & Boris, 2005)

$$L_{box}/\Delta x > Re, \tag{3.12}$$

otherwise nonphysical structures at short wavelengths might appear in the DNS. Condition (3.12), combined with the relation for η in (3.4) leads to:

$$\Delta x \leq \eta Re^{-1/4}, \tag{3.13}$$

which clearly is a more severe condition than (3.10). Thus, in these cases the numerical resolution has to be considerably better than the Kolmogorov lengthscale, even if nothing relevant for the flow happens at this scale. This makes DNS even more expensive as a computational approach to study the physics of high Re turbulent flows.

3.2 Large Eddy Simulation (LES)

Different approaches have been developed over the years to numerically simulate turbulent flows. These alternatives belong to what is known as turbulence modeling. As the name itself suggests, turbulence modeling aims to mimic the contribution of the small scales of turbulence. A numerical scheme in which the small scales are not resolved but modeled by a suitable physical theory of turbulence is called a sub-grid scale (SGS) method. This allows to perform computationally less expensive simulations of complex turbulent flows at higher Reynolds number, but at the expense of a model that is not always possible to justify rigorously. Simulations based on a SGS method are called Large Eddy Simulations or LES, since they are designed to resolve only the large scales of a turbulent flow, while the physics of the small scales are incorporated through a theoretical turbulence model.

3.2.1 Filtered equations and SGS models

The most common conceptual approach to understand LES is via the filtering of the dynamical equations. The main idea behind this approach is that the LES represents a smoothed solution of the equations where the small scales have been eliminated, or

more accurately: filtered. Thus, a filtering operation is defined when the field variables, $\phi_i = (u, v, w, P, ...)$, are decomposed into the sum of a filtered (or resolved) component, $\widetilde{\phi}_i$, and a residual (or sub-grid scale) component, ϕ_i' (The Reynolds decomposition used in chapter 2 is a particular filtering operation where $\widetilde{\phi}_i = \overline{\phi}_i$). As an illustrative example, in the following lines we present the filtering process of the Navier-Stokes equation in the absence of external forces over the fluid:

$$\frac{\partial u_i}{\partial t} + (u_j \nabla_j)\, u_i = \frac{1}{\rho}\nabla_i P + \nu \nabla^2 u_i, \tag{3.14}$$

Notice that eq. (3.14) is a particular case of eq. (2.1) with $g_i = 0$ and $B = 0$ and in the incompressibility regime. The incompressibility condition, $\nabla_i u_i = 0$, reduces the viscous stress tensor, σ_{ij}, in eq. (2.1) to the Laplacian term at the end of the rhs of eq. (3.14). Any filtering operator can be written as a convolution integral, hence the filtered velocity field can be written as:

$$\widetilde{u}_i(\vec{x}, t) = G(\Delta) * u_i(\vec{x}, t) = \int_\Omega G(\Delta, \vec{x}, \vec{y})\; u_i(\vec{y}, t) d^3 y, \tag{3.15}$$

where Ω, $G(\Delta, \vec{x}, \vec{y})$ and Δ are the domain, the filter kernel and the filter characteristic length, respectively. $\vec{x}$ is the position vector and $\vec{y}$ is the spatial vector variable over which the integration is done (the filter operator defined above belongs to the class of spatial filters, other kinds of filters are discussed in Grinstein et al. (2007)). In general, for any quantity ϕ the corresponding filtered value will be denoted as $\widetilde{\phi}$. The filtered Navier-Stokes equations are obtained by substituting eq. (3.15) into eq. (3.14), which leads to:

$$\frac{\partial \widetilde{u}_i}{\partial t} + \widetilde{(u_j \nabla_j)}\, u_i = \frac{1}{\rho}\widetilde{\nabla_i P} + \nu \widetilde{\nabla^2 u_i}. \tag{3.16}$$

The analysis to obtain filtered dynamical equations will be restricted here to spatial filters that commute with spatial derivatives, i.e., $\widetilde{\partial u_i} = \partial \widetilde{u}_i$. The use of a spatially homogeneous filter together with the incompressibility condition implies $u_j \nabla_j u_i = \nabla_j (u_i u_j)$. This simplifies (3.16) to

$$\frac{\partial \widetilde{u}_i}{\partial t} + \nabla_j \widetilde{(u_i u_j)} = \frac{1}{\rho}\nabla_i \widetilde{P} + \nu \nabla^2 \widetilde{u}_i. \tag{3.17}$$

Next, we define the SGS stress tensor as $\tau_{ij}^G = \widetilde{u_i u_j} - \widetilde{u}_i \widetilde{u}_j$. Then, eq. (3.17) can be written as

$$\frac{\partial \widetilde{u}_i}{\partial t} + (\widetilde{u}_j \nabla_j)\, \widetilde{u}_i + \nabla_j \tau_{ij}^G = \frac{1}{\rho} \nabla_i \widetilde{P} + \nu \nabla^2 \widetilde{u}_i. \tag{3.18}$$

A closure problem of the equations appear at this point since the term $\nabla_j \tau_{ij}^G$ cannot be computed exactly [1]. Therefore it must be evaluated using a model, since it involves the non-resolved stress tensor, it is called a SGS model.

The simplest SGS model is the Smagorinsky one. It states that the SGS stress tensor can be written in terms of the filtered strain tensor, $\widetilde{S}_{ij}$, multiplied by an eddy viscosity that accounts for the small-scale (not resolved) motions, denoted by ν_t:

$$\tau_{ij}^G = -2\nu_t \widetilde{S}_{ij}. \tag{3.19}$$

For the case of incompressible flow this modifies eq. (3.18) to

$$\frac{\partial \widetilde{u}_i}{\partial t} + (\widetilde{u}_j \nabla_j)\, \widetilde{u}_i = \frac{1}{\rho} \nabla_i \widetilde{P} + (\nu + \nu_t) \nabla^2 \widetilde{u}_i. \tag{3.20}$$

The Smagorinsky eddy viscosity is given by $\nu_t = (C_s \Delta)^2 \mid \widetilde{S} \mid$ (Pope, 2000). Here, Δ is the filter width and C_s the so-called Smagorinsky coefficient, for which values around 0.15 are typically assumed depending of the filter used. Eq. (3.20) is identical to the original Navier-Stokes equation (3.14) with exception that the filtered eqs. above have an effective small-scale contribution that accounts for the SGS eddy viscosity (i.e., these scales contribute only as dissipative processes). In this sense the LES solution is equivalent to the DNS solution for a Reynolds number lowered by a factor $(1 + \nu_t/\nu)$. A concise discussion of other SGS models, including several improvements of the Smagorinsky model, can be found in Pope (2000) and Grinstein et al. (2007).

3.2.2 DNS vs LES

Since a LES does not resolve all the turbulent scales, it results computationally less expensive and in that sense more attractive for practical purposes in engineering, geophysics and astrophysics. However, the LES approach is not entirely independent from the DNS one, since comparing the results of LES with DNS is crucial to validate a SGS

[1] Any filter applied to the non-linear Navier-Stokes equations leads to the appearance of second order correlations which represent additional unknowns for the filtered equations. In this sense, we say there is a closure problem as the number of unknowns exceeds the number of equations.

model. In engineering applications these models can always be tested against the experiments. This is not usually the case in astrophysics where experimental setups are extremely hard to realize (if not impossible).

For different flow configurations, different methods have been used, and most of the physics behind the different LES approaches known today is still not well understood. Therefore, it is not easy to have a general idea of the global advantages of LES over DNS. As an example, consider the incompressible forced turbulence simulations carried out, at resolutions up to 4096^3 meshpoints, by Kaneda et al. (2003). Comparisons, in terms of the energy spectra, with Smagorinsky LES by Haugen & Brandenburg (2006) and hyperviscosity simulations by Haugen & Brandenburg (2004) are shown in Fig. 3.6.

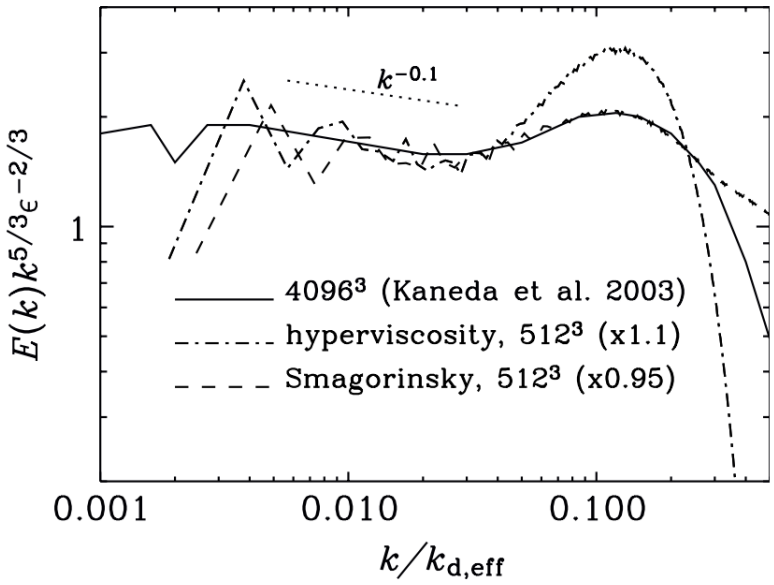

FIGURE 3.6: Comparison of energy spectra of the 4096^3 meshpoints DNS of Kaneda et al. (2003) and 512^3 meshpoints numerical experiments with hyperviscosity of (Haugen & Brandenburg, 2004), and Smagorinsky LES of (Haugen & Brandenburg, 2006). The Taylor microscale Reynolds number (the Taylor microscale marks the transition between the inertial subrange and the dissipation range, i.e., it can be identified with the scale l_{DI} previously defined) of the Kaneda simulations is 1201, while for the hyperviscous simulation it has a value between 340 and 730, and for the simulation with the Smagorinsky SGS model, it is slightly smaller (Plot taken from Haugen & Brandenburg (2006)).

Fig. 3.6 reveals an important correction, within the inertial subrange, of about $k^{-0.1}$ to the usual $k^{-5/3}$ spectrum. Thus, the energy transfer scales with the wavenumber as $k^{-1.77}$. Similar deviations are observed for the Smagorinsky SGS model (Haugen & Brandenburg, 2006), and for the simulations with hyperviscosity (Haugen & Brandenburg, 2004). Despite the agreement of the three simulations within the inertial subrange, the nature of the $k^{-0.1}$ correction factor is still not well understood. On the other hand, near the dissipation range a power excess of the spectra is observed, phenomena called the bottleneck effect (Falkovich, 1994) .

3.3 Implicit Large Eddy Simulation

Over the last few years a new class of numerical schemes has exhibited the capacity of producing LES of turbulent flows without the need of any explicit SGS model. The so-called nonoscillatory finite volume (NFV) schemes are the only ones able to show such a behaviour so far. The term Implicit Large Eddy Simulations (ILES) refers to simulations using such a class of numerical schemes. The absence of explicit SGS models in ILES offers certain practical advantages in terms of computational efficiency and implementation, but that is not enough to justify the use of an ILES approach. A completely satisfactory rationale for the success of the ILES approach has not been developed yet. It can be said that ILES works because it gives solution to the equations that most accurately represent the fluid finite volume dynamics, thus, the equations that govern the behaviour of physically measurable quantities on the computational cells (Grinstein et al., 2007).

All numerical schemes have approximation errors. These errors can be identified, by using modified equation analysis (MEA), as truncation terms that add to the original analytic equations. It has been proved that, in typical flow regimes, these truncation terms have the same order of magnitude as the SGS terms in an explicit LES (Ghosal (1996), Hirt (1969)). Therefore it is reasonable to ask whether the numerical scheme truncation errors would serve as SGS models by themselves. In this chapter we analize the MPDATA algorithm (mostly used in the EULAG code), which is widely known for its success in modelling atmospheric flows (Prusa et al., 2008), and more recently for its use in studies of solar-stellar dynamos (Ghizaru et al. (2010),Smolarkiewicz & Charbonneau (2013), Guerrero et al. (2013), Guerrero et al. (2016), Strugarek et al. (2016)).

3.3.1 The basic MPDATA

A particular ILES approach is implemented in the so-called method MPDATA (multidimensional positive definite advection transport algorithm). In this section a 1D example is presented to explain the basics of MPDATA; then in the next section, a rationale for the success of MPDATA as an ILES scheme is discussed. Originally designed for the transport of non-negative thermodynamic variables in atmospheric models, MPDATA has grown into a family of finite-difference approximations for the advective terms in the equations of fluid dynamics. To illustrate the basic idea behind the MPDATA consider the one-dimensional advection equation for a scalar variable Φ:

$$\frac{\partial \Phi}{\partial t} = -c\frac{\partial \Phi}{\partial x} \tag{3.21}$$

,

where c is a constant advection velocity. The first pass of MPDATA is a donor cell approximation to the eq. (3.21), in flux form, given by:

$$\Phi_i^{n+1} = \Phi_i^n - \left[F(\Phi_i^n, \Phi_{i+1}^n, U_{i+1/2}) - F(\Phi_{i-1}^n, \Phi_i^n, U_{i-1/2})\right], \tag{3.22}$$

here the indices n and i account for the time step and the spatial location in the grid, respectively. The flux function, F, is defined in terms of the local Courant number, U, as:

$$F(\Phi_L, \Phi_R, U) = [U]^+\Phi_L + [U]^-\Phi_R \tag{3.23}$$

$$U = \frac{c\delta t}{\delta x} \tag{3.24}$$

$$[U]^+ = 0.5(U + |U|) \tag{3.25}$$

$$[U]^- = 0.5(U - |U|), \tag{3.26}$$

where the integer and half-integer indices correspond to the cell vertices and walls, respectively (See Fig. 3.7); and δt and δx correspond to the time step and cell width. Replacing a Taylor expansion of the scalar fields ($\Phi_i^{n+1}, \Phi_{i+1}^n.\Phi_{i-1}^n$), around Φ_i^n, into eq. (3.22) gives:

$$\left[\frac{\partial \Phi}{\partial t}\right]_i^n = -c\left[\frac{\partial \Phi}{\partial x}\right]_i^n + \frac{(\delta x)^2}{2\delta t}\left(|U| - U^2\right)\left[\frac{\partial^2 \Phi}{\partial x^2}\right]_i^n \tag{3.27}$$

where the symbol $[]_i^n$, means that the term inside is evaluated at grid point i; and time-step n. Eq. (3.27) shows that the discretization in eq. (3.22) more accurately approximates the advection-diffusion equation:

$$\frac{\partial \Phi}{\partial t} = -c\frac{\partial \Phi}{\partial x} + \frac{\partial}{\partial x}\left(K\frac{\partial \Phi}{\partial x}\right) \tag{3.28}$$

where

$$K = \frac{(\delta x)^2}{2\delta t}\left(|U| - U^2\right). \tag{3.29}$$

Eq. (3.28) is called the modified equation (ME) of the numerical scheme and remains valid even for non-constant advection velocity $c = c(x)$. To improve the accuracy of the method, a numerical estimate of the truncation error is substracted from the original discrete eq. (3.22). For this particular case, the MPDATA uses a donor cell approximation for the error term, i.e., the error term is written as:

$$error^{(1)} = \frac{\partial}{\partial x}\left(v^{(1)}\Phi\right) , \tag{3.30}$$

where

$$v^{(1)} = \frac{(\delta x)^2}{2\delta t}\left(|U| - U^2\right)\frac{1}{\Phi}\frac{\partial \Phi}{\partial x} \tag{3.31}$$

is called a pseudo velocity. The superscript (1) refers to the first approximation, given by (3.22), to subtracting the error. Notice that to write the pseudo velocity, the second term in (3.28) is multiplied by a factor Φ/Φ, i.e., by unity. However, in the donor cell approximation the factor in the numerator is evaluated using an upstream value, while the denominator is evaluated using a centered value (See Fig. 3.7).

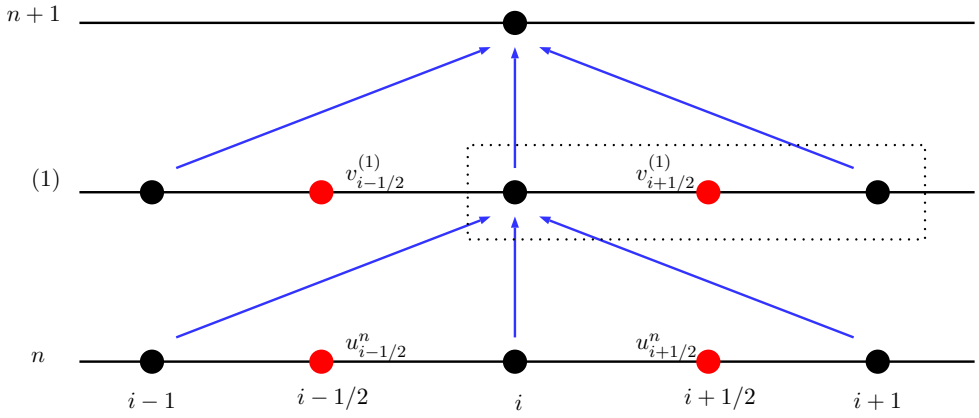

FIGURE 3.7: Stencil representation of MPDATA. The vertical direction shows the time advance and the horizontal axis shows the spatial discretization (advection first-pass velocities and second-pass pseudo-velocities are computed using centered values, i.e., at the walls of the grid cells). The dotted box encompasses the grid points considered for the calculation of the pseudo-velocity $v^{(1)}_{i+1/2}$.

Therefore, in the donor cell approximation, the term $\partial\Phi/\partial x$ in eq. (3.31) is evaluated using a forward difference formula, $(\Phi^{(1)}_{i+1} - \Phi^{(1)}_i)/\delta x$. While in the denominator, Φ, is computed using a centered value, $\Phi^{(1)}_{i+1/2} = 1/2\left(\Phi^{(1)}_{i+1} + \Phi^{(1)}_i\right)$. In this sense a first order accurate estimate of the pseudo velocity is given by:

$$v^{(1)}_{i+1/2} = \frac{\delta x}{\delta t}\left(|U| - U^2\right)\frac{\Phi^{(1)}_{i+1} - \Phi^{(1)}_i}{\Phi^{(1)}_{i+1} + \Phi^{(1)}_i}, \tag{3.32}$$

and the corresponding Courant number is given by $V^{(1)} = v^{(1)}\delta t/\delta x$. In the second pass of MPDATA, the error, given by eq. (3.32), is subtracted via the donor cell discretization to get the second order approximation of the field $\Phi^{(2)}$:

$$\Phi_i^{(2)} = \Phi_i^{(1)} - \left[F(\Phi_i^{(1)}, \Phi_{i+1}^{(1)}, V_{i+1/2}^{(1)}) - F(\Phi_{i-1}^{(1)}, \Phi_i^{(1)}, V_{i-1/2}^{(1)})\right]. \tag{3.33}$$

Then, we take $\Phi^{n+1} \sim \Phi^{(2)}$ (The entire MPDATA stencil is shown in fig. 3.7). The two-pass MPDATA scheme described above can be extended to an arbitrary number of iterations, reducing the magnitude of the truncation error (Smolarkiewicz & Margolin, 1998b). The extension of MPDATA to 2 or more dimensions follows the same iterative donor cell approach. However, there are subtleties due to the cross derivatives that appear in the Taylor expansions in several variables (Smolarkiewicz & Margolin, 1998a).

3.3.2 The ILES character of MPDATA

A relatively simple rationale (using MEA) for the success of MPDATA in modeling turbulent flows is presented by Grinstein et al. (2007). There, the MPDATA is applied to the 1D Burgers equation:

$$\frac{\partial u}{\partial t} = -u\frac{\partial u}{\partial x} + \lambda\frac{\partial^2 u}{\partial x^2} \tag{3.34}$$

The derivation of the corresponding modified equation is quite long and requires several algebraic manipulations. Therefore, the result is presented without derivation. Let $\overline{u}$ be the MPDATA numerical solution of 3.34 for which the corresponding modified equation is given by [2]:

$$\begin{aligned}\overline{u}_t = &-\overline{u}_x\overline{u} + \lambda\overline{u}_{xx} + \lambda\left(\frac{\overline{u}_{xxtt}(\delta t)^2}{8} + \frac{\overline{u}_{xxxx}(\delta x)^2}{12}\right) + \left(\frac{|U|}{4} - \frac{1}{6}\right)\overline{u}_{xxx}\overline{u}(\delta x)^2 \\ &+ \frac{(1-|U|)(\delta x)^2}{4}\left(|\overline{u}_x|\,\overline{u}_{xx} - \overline{u}_x\overline{u}_{xx}\right) - \frac{\delta t\delta x}{4}\left(sgn\,(U)\,|\overline{u}_x|\,(\overline{u}_x)^2 - U\,(\overline{u}_x)^3\right) + ...\end{aligned} \tag{3.35}$$

where $U = \overline{u}\delta t/\delta x$ is the Courant number and $sgn\,(U) = |U|/U$. On the other hand, if we consider volume integration of the Burgers equation over a finite interval in space and time, the resulting equation describes the evolution of finite volumes of Burgers

[2] Here we use a short notation for derivatives, e.g., $\overline{u}_x = \frac{\partial \overline{u}}{\partial x}$. In a similar way, for high-order derivatives we use various subscript symbols, e.g., $\overline{u}_{xxtt} = \frac{\partial^2}{\partial^2 t}\left(\frac{\partial^2 \overline{u}}{\partial^2 x}\right)$.

fluid. Denote the time and spatial scales of integration as T and L, respectively, and let $\overline{u}$ be the volume averaged (cell-averaged) velocity field. Then, the resulting equation for the volume integration of the Burgers equation is given by (Grinstein et al., 2007):

$$\begin{aligned}\overline{u}_t = &-\overline{u}_x\overline{u} - \frac{1}{3}\overline{u}_x\overline{u}_{xx}\left(\frac{L}{2}\right)^2 - \frac{1}{3}\left(\overline{u}_x^3\overline{u} + \overline{u}^2\overline{u}_x\overline{u}_{xx}\right)\left(\frac{T}{2}\right)^2 \\ &+ \lambda\overline{u}_{xx} + \frac{\lambda}{6}\left(\left(\overline{u}_x\right)^2\overline{u}_{xx} + \overline{u}\left(\overline{u}_{xx}\right)^2 + \overline{u}_x\overline{u}_{xxx}\overline{u}\right)\left(\frac{T}{2}\right)^2 \\ &+ \lambda\left[\frac{1}{6}\overline{u}_{xxxx}\left(\frac{L}{2}\right)^2 + \frac{1}{6}\overline{u}_{xxtt}\left(\frac{T}{2}\right)^2\right] + ...\end{aligned} \tag{3.36}$$

The close similarity of the eqs. (3.35) and (3.36) is the basis of the rationale for the success of MPDATA in simulating the unresolved turbulent scales. If the modified equation of MPDATA is compared to the original Burgers equation, the nonlinearly dispersive terms are identified as truncation errors. However, if the MPDATA modified equation is compared directly with the finite volume equation, it can be seen that these terms corresponding to the truncation errors are, indeed, necessary corrections to represent correctly the fluid finite volume dynamics.

Therefore, a direct comparison of the MPDATA modified equation and the analytic equation for the finite volume dynamics shows that the truncation errors have physical significance. Even though, a closer look to eqs. (3.35) and (3.36) shows certain differences that are still a matter of research, it can be said that the success of MPDATA for modelling turbulent flows is a consequence of its more accurate approximation to the equations of the dynamics of finite volumes of fluid. More comprehensive studies have revealed additional hints on the implicit SGS model of MPDATA. Domaradzki et al. (2003) showed that the SGS model implicit in MPDATA qualitatively mimics an eddy viscosity, in the context of 3D homogeneous turbulence in a cartesian box. Based on this idea, Strugarek et al. (2016) compared global simulations of solar convection performed with the ILES-type code EULAG (which uses MPDATA, Prusa et al. (2008)) and the LES-type code ASH (Brun et al., 2004), finding good agreement between the large-scale flows developed in both codes in the hydrodynamic regime.

Although the precise nature of the ILES approach remains elusive, recent developments are showing that numerical schemes like MPDATA are quite robust in modeling the small-scales of turbulent flows. In the next chapter we present implicit large eddy simulations of solar convection performed with the code EULAG-MHD.

Chapter 4

The model

In this work we use an MHD extension of the code EULAG to perform ILES of a domain that resembles a fraction of the upper part of the solar convection zone. In this chapter, we present the equations solved by the code EULAG, and the anelastic background atmosphere equations that allow the development of the convective instability.

4.1 EULAG-MHD

The code EULAG is used to perform simulations of anelastic[1] turbulent convection. As mentioned before, this code was originally designed to model atmospheric (multi-scale) flows and is widely known for its success in that area (Prusa et al., 2008). Recently, an MHD extension of the code has allowed to perform simulations of solar and stellar dynamos (Ghizaru et al. (2010), Racine et al. (2011), Smolarkiewicz & Charbonneau (2013), Guerrero et al. (2013), Guerrero et al. (2016), Strugarek et al. (2016)). The versatility of EULAG relies on its generalized curvilinear coordinates formulation, with the nonoscilatory forward-in-time (NFT) differencing scheme based on MPDATA (Smolarkiewicz & Margolin, 1998b), and its robust elliptic solver (Smolarkiewicz et al., 1997). In the following we will refer to the MHD extension of EULAG as EULAG-MHD.

4.1.1 The set of equations

The set of equations that EULAG-MHD solves is an MHD extension of the Lipps-Hemler anelastic system (Lipps & Hemler, 1982). In a non-rotating frame these equations can be written as:

[1] The anelastic approximation, originally proposed for global atmospheric models, was invented by Ogura & Phillips (1962) in order to filter sound-wave solutions from the equations of motion without assuming hydrostatic balance.

$$\frac{d\vec{u}}{dt} = -\nabla\pi' - \vec{g}\frac{\theta'}{\theta_0} + \frac{1}{\mu\rho_0}\vec{B}\cdot\nabla\vec{B} \tag{4.1}$$

$$\frac{d\theta'}{dt} = -\vec{u}\cdot\nabla\theta_e - \alpha\theta' \tag{4.2}$$

$$\frac{d\vec{B}}{dt} = \vec{B}\cdot\nabla\vec{u} - \vec{B}\nabla\cdot\vec{u} \tag{4.3}$$

$$\nabla\cdot\rho_0\vec{u} = 0 \tag{4.4}$$

$$\nabla\cdot\vec{B} = 0 \tag{4.5}$$

Here, θ is the potential temperature, which commensurates the specific entropy via $s = c_p \ln\theta$. Subscripts "o" denote an isentropic base state in hydrostatic balance, primes denote perturbations around an ambient state (denoted by subscript "e"). In analogy with the MLT, isentropic and ambient states can be thought as the ones corresponding to the fluid-elements, which move adiabatically, and their surroundings. Finally, $\vec{g}$ is the gravitational acceleration considered constant and π' is a density normalized pressure perturbation encompassing the hydrostatic and magnetic pressure.

4.1.2 Aneslastic atmosphere

The scheme used in EULAG-MHD makes use of two initial states (Smolarkiewicz & Charbonneau, 2013), an **adiabatic state** (for which the corresponding potential temperature, θ_o, is constant) and the **ambient state** (for which the potential temperature is denoted as θ_e). For our setup the adiabatic stratification profiles are obtained from the adiabatic state equation, $P\rho^{-\gamma} = cte$ (here γ is the adiabatic exponent), and the hydrostatic equilibrium condition in the radial direction:

$$\frac{dP}{dr} = \rho(r)g(r), \tag{4.6}$$

where $g(r)$ is the radial component of the gravitational field (taken constant, $g(r) = g_o$). The previous equations can be easily integrated yielding:

$$\rho_o(r) = \rho_b\left[1 - \frac{(\gamma-1)g\rho_b}{\gamma P_b}(r - r_0)\right]^{\frac{1}{\gamma-1}}, \tag{4.7}$$

$$P_o(r) = P_b\left[1 - \frac{(\gamma-1)g\rho_b}{\gamma P_b}(r - r_0)\right]^{\frac{\gamma}{\gamma-1}}, \tag{4.8}$$

$$T_o(r) = T_b\left[1 - \frac{(\gamma-1)g\rho_b}{\gamma P_b}(r - r_0)\right], \tag{4.9}$$

$$\theta_o(r) = \theta_b = T_b, \tag{4.10}$$

here, T_b, ρ_b, P_b are the values of the temperature, T; density, ρ; and pressure, P, at the bottom of the domain. The ambient state is chosen to be a polytropic state with a polytropic index, $m = m(r)$, that is a function of the vertical coordinate, r. To define the ambient state we use the general definition of a polytropic state:

$$\frac{d}{dr}\left(\log P\right) = \left(1 + \frac{1}{m}\right)\frac{d}{dr}\left(\log \rho\right), \tag{4.11}$$

which, together with the eq. (4.6) and the ideal gas state equation $P = R_g \rho T$, result in

$$\frac{dT_e}{dr} = \frac{g_o}{R_g(m(r)+1)}. \tag{4.12}$$

It is well known that a polytropic state is convectively unstable for $m < 1.5$, and convectively stable for $m > 1.5$. The critical value $m = 1.5$ corresponds to an adiabatic state. Another equation is necessary to complete the description of the ambient state, i.e., T_e, ρ_e, P_e. It can can be derived from the ideal gas relation and the hydrostatic equilibrium condition:

$$\frac{d\rho_e}{dr} = \frac{\rho_e}{T_e}\left[\frac{g_o}{R_g} - \frac{dT}{dr}\right]. \tag{4.13}$$

The set of eqs. (4.12) and (4.13) can be numerically integrated by using a Runge-Kutta solver of fourth order and boundary values for T_e and ρ_e. The ambient pressure, P_e, can be obtained from the ideal gas equation once the system is solved.

4.1.3 Closure for the Reynolds heat flux

The last term on the rhs of eq. (4.2) is a Newtonian cooling term that mimics the divergence of the non-computable Reynolds heat flux (See Appendix A and B in Cossette (2015)). This term has the form:

$$\frac{d}{dz}\rho_0\langle w'\theta'\rangle = -\rho_0\alpha\theta'. \tag{4.14}$$

Here, the turbulent horizontal velocity is denoted as w'. The term in (4.14) relaxes θ' toward zero within a time-scale $\tau = \alpha^{-1}$. To look for a suitable value of α in our configuration, we consider different values of this quantity and study its effect on the convective structure and on anomalous radial modes observed in the simulations (see Chapter 5).

4.2 Setup of the simulations

4.2.1 Physical and code units

The simulations with EULAG-MHD were performed using code units. However, for comparisons with the Sun, it is convenient to transform the results into physical units. To that end it is necessary to choose suitable characteristic units of length, density, temperature and magnetic field. The conversion from code units (with primes) to physical units considered here is given by:

$$x_j = L_0 x'_j, \tag{4.15}$$

$$t = (L_0/g_\odot)^{1/2}\, t', \tag{4.16}$$

$$\rho = \rho_\odot, \tag{4.17}$$

$$T = T_\odot T', \tag{4.18}$$

$$B = (\mu_0 \rho_\odot g_\odot L_0)^{1/2}\, B', \tag{4.19}$$

$$\tag{4.20}$$

where we use $L_0 = 10$ Mm as the characteristic unit of length. For density and temperature we choose the values at the solar surface, $\rho_\odot = 2.5 \times 10^{-4}$ Kg $\cdot$ m^{-3}, and $T_\odot = 5800$ K, as the characteristic units, respectively. For the characteristic gravitational acceleration we take the value at the surface of the sun $g_\odot = 274$ m $\cdot$ s^{-2}. Finally, the permeability of the vacuum is $\mu_0 = 4\pi \times 10^{-7}$ N $\cdot$ A^{-2}.

4.2.2 Cartesian box setup

In the cartesian frame, we label the coordinates as (x, y, z), where x, y and z correspond to θ, ϕ and r in the spherical case. The computational domain consists of a Cartesian box of dimensions $(L_x, L_y, L_z) = (5, 5, 2)$ in code units (See fig. 4.1). The simulations were performed using two different resolutions in the 3D case, 128^3 and 256^3 grid points; and only one resolution for the 2D study, 240^2 grid points. A three-layer profile for the polytropic index $m(r)$, which defines the ambient state, was chosen using error functions as transitions between the layers as follows:

$$m(r) = m_1 + \frac{m_2 - m_1}{2}\left(1 - erf\left(\frac{r - r_{12}}{d}\right)\right) + \frac{m_3 - m_2}{2}\left(1 - erf\left(\frac{r - r_{23}}{d}\right)\right). \tag{4.21}$$

For the simulations in this work, the parameters considered for the polytropic stratification were $(m_1, m_2, m_3, r_{12}, r_{23}, d) = (3.0, 1.5, 1.46, 0.2, 1.8, 0.1)$. This leads to a vertical stratification with a convectively stable layer at the bottom $(0.0 < z < 0.2)$, followed by an adiabatic layer $(0.2 < z < 1.8)$, and a convection-unstable layer at the top, $(1.8 < z < 2.0)$.

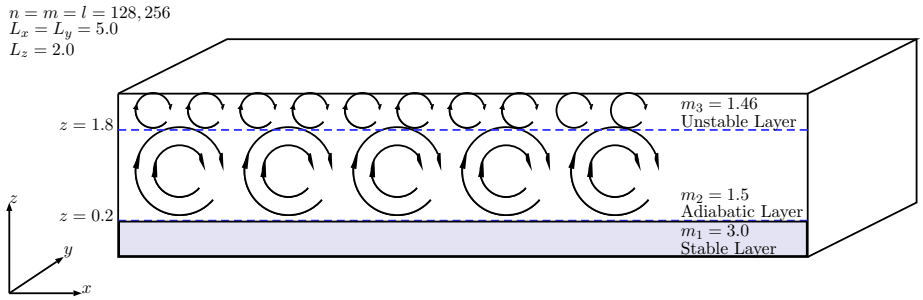

FIGURE 4.1: Schematics of the cartesian boxes considered for the simulations with a four-layer stratification. Horizontally, all boxes have dimensions of $50 \times 50 \times 20$ Mm.

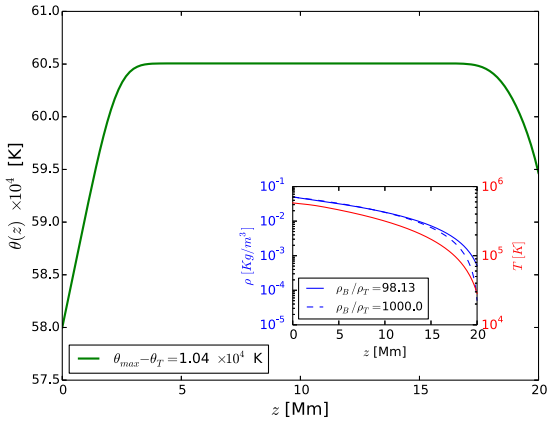

FIGURE 4.2: Potential Temperature profile of the polytropic atmosphere, θ_e, considered as the ambient state in the model. The inset shows the vertical profiles of the corresponding density (blue lines) and temperature (red line) stratifications as a function of the vertical direction, z (see eqs. (4.12)-(4.13)). The blue dashed line corresponds to the adiabatic density profile (see eq. (4.7)).

The vertical distributions of θ_e, ρ and T as a function of the radius are shown in Figure 4.2. The potential temperature is calculated using the relation $\theta(r) = T(r)(P_b/P(r))^{R_g/c_p}$.

The inset shows the vertical profiles of the corresponding density (blue lines) and temperature (red line) stratifications as a function of the vertical direction, z (see eqs. (4.12)-(4.13)). The blue dashed line corresponds to the adiabatic density profile (see eq. (4.7)). Random small perturbations, over the potential temperature θ_e and the z component of flow velocity field w, about the hydrostatic equilibrium are considered as the initial condition for the HD convective state. We use impermeable, stress-free conditions at the top and bottom surfaces of the domain such that:

$$w = \frac{\partial u}{\partial z} = \frac{\partial v}{\partial z} = 0. \tag{4.22}$$

The magnetic field is assumed to be radial at these boundaries, i.e., $\frac{\partial B_z}{\partial z} = B_x = B_y = 0$. Besides, we consider an infinite reservoir of potential temperature fluctuations at the top boundary:

$$\theta'(z_{top}, t_0) = \theta'(z_{top}, t), \text{ for } t > t_0, \tag{4.23}$$

and zero divergence of the convective flux of potential temperature fluctuations at the lower boundary: $\nabla \cdot (\rho_0 \vec{u}\theta') = 0$.

Chapter 5

Results: Solar convection and magnetic structures with EULAG

In this chapter we present the results and analysis of our numerical study. We aim to achieve a convective model, in Cartesian coordinates, able to fulfill the constrains for the development of MHD instabilities reported in the literature (Kleeorin et al. (1989), Kleeorin et al. (1996), Rogachevskii & Kleeorin (2007), Brandenburg et al. (2011), (Losada et al., 2014), Käpylä et al. (2012), Käpylä et al. (2016)). To that end, we perform two dimensional HD simulations and study the influence of the relaxation time $\tau = \alpha^{-1}$ on the properties of convection. The results are presented in the first section of this chapter. In the second section we extend one of these models, the one with multi-scale convection with reasonable amplitudes observed, to three dimensions and perform the simulations with low and high resolution (128^3 and 256^3 gridpoints), respectively. The properties of these two cases are then presented emphasizing in the differences observed in the convective patterns when the resolutions is changed. The final statistically steady state of these models is used as the initial condition for the MHD models where vertical external magnetic fields of different strengths are imposed. The results are discussed in Sec. 5.2. Finally, we discuss the appearance and evolution of magnetic structures in these simulations and the possible role of NEMPI as the instability driver.

5.1 HD convective states

5.1.1 Two dimensional HD simulations with EULAG

According to the equations (4.1)-(4.5), convection is driven when the radial gradient of θ_e (corresponding to the ambient state) is negative as discussed in Sec. 4.2. Yet

the amplitude of the convective velocities depends on two parameters: the value of the polytropic indices, m_2 and m_3, and the relaxation time, τ, of the perturbations of the potential temperature θ. For the simulations presented below, we keep the profile of θ_e defined above, and explore the effects on the convection for different values of τ. Since three-dimensional models are computationally expensive for parametric analysis, we perform this study through 2D simulations with a resolution of 240^2 meshpoints. Two different kinds of models for the relaxation time were considered. The first one (models "cf" in Table 5.1) assumes $\tau = t_0$ with t_0 constant over the entire domain. The second kind (models "vf" in Table 5.1) takes a depth-dependent profile for τ as follows:

$$\tau(r) = t_0 \sqrt{\frac{\rho(r)}{\rho_0}}, \tag{5.1}$$

where $\rho_0(r)$ and ρ_b are given by eq. (4.7). Eq. (5.1) gives a relaxation time proportional to the square root of the adiabatic density profile, this implies that the perturbations are allowed to develop for longer time at the bottom of the domain, while they are damped faster at the top. For each of the two kinds of models considered, four values of t_0 (shown in code units) were tested (a summary of the parameters and results is presented in Table 5.1).

TABLE 5.1: Results for the 2D simulations

–parameter simulation–	t_0 [code units]	u_{rms} $\times 10^3$[m/s]	$\overline{\theta'}$ $\times 10^4$[K]
100-cf	100	0.422	0.045
250-cf	250	0.278	0.049
500-cf	500	0.249	0.053
1000-cf	1000	0.235	0.055
100-vf	100	0.593	0.024
250-vf	250	0.477	0.029
500-vf	500	0.408	0.033
1000-vf	1000	0.409	0.037

Anomalous radial modes[1] appear in all of the simulations. To alleviate the appearance of these radial modes, two types of filters were used. One for the 2D simulations and

[1] Non-physical oscillations have been observed in the upper layers of the domain for all the simulations presented in this work. However, it seems that these oscillations do not modify the convective structure at the small scales observed in the upper layers.

a different one for the 3D simulations. For the 2D hydrodynamic simulations the filter considered ($F1$) is given by:

$$(u_z)_f(i,j,k) = \frac{1}{2}\left[u_z(i,j,k) + u_z(i,j,k+1)\right], \tag{5.2}$$

where $u_z(i,j,k)$ is the vertical component of the flow velocity field at the grid location (i,j,k), and the subscript f indicates filtered data. Vertical slices of the radial velocity for some of the simulations in table 5.1 are shown in Fig. 5.1. The left panel shows the unfiltered data, and the right panel shows the data filtered with ($F1$). The kinetic energy spectra for the 2D simulations considered is given by:

$$E(k,t) = \frac{1}{2}\sum_{k_x^2+k_z^2=k^2} |\hat{u}(k_x,k_z,t)|^2, \tag{5.3}$$

where $\hat{u}$ is the fourier transform of the velocity field. The spectra for the simulations in table 5.1 are shown in fig. 5.2. The lhs (rhs) panel corresponds to the "cf" ("vf") model, and different colors indicate different values of t_0, as indicated in the legends. It is observed that the spectral distribution of kinetic energy changes appreciably from one model to another.

For the model **100-cf**, several power peaks are observed at, $k \sim (0.7, 1.5, 4.5, 8.5)$ Mm^{-1}, suggesting the presence of several dominant scales of convection. An inertial range can be identified, but its extent is unclear due to the presence of strong oscillations at large wavenumbers. For the models **250-cf** and **500-cf**, a power peak at $k \sim 1$ Mm^{-1} is observed together with a power excess at large wavenumbers. The spectrum obtained for model **1000-cf** exhibits a behavior similar to that of models **250-cf** and **500-cf**, except that in this case there is no power peak at $k \sim 1$ Mm^{-1}. In general, the presence of a well-defined inertial range is unclear for all the "cf" models. On the other hand, the spectra for the "vf" models show a well defined inertial range located at wavenumbers within the range, $1 < k < 5$ Mm^{-1}. For the model **100-vf**, there is a power peak at $k \sim 1$ Mm^{-1}. Similar behavior is observed for the models **250-vf** and **500-vf**. However, large amplitude oscillations at the largest wavenumbers are observed for the model **1000-vf** similar to the ones in the spectrum of the model **100-cf**. The nature of the oscillations (radial modes) observed in the models **100-cf** and **1000-vf** is probably of numerical origin. We see that the model chosen to parameterize the relaxation time can affect significantly the energy distribution of the convection.

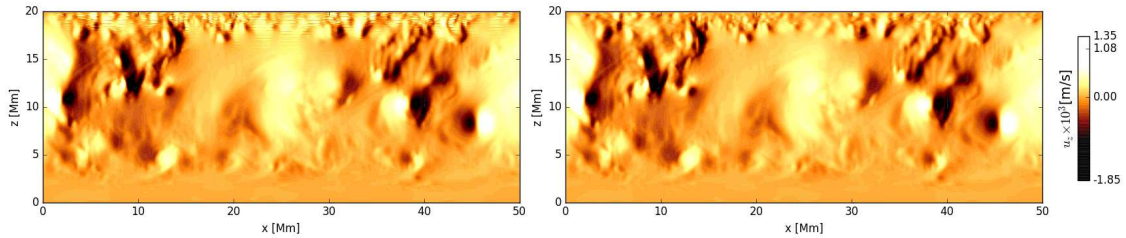

(a)

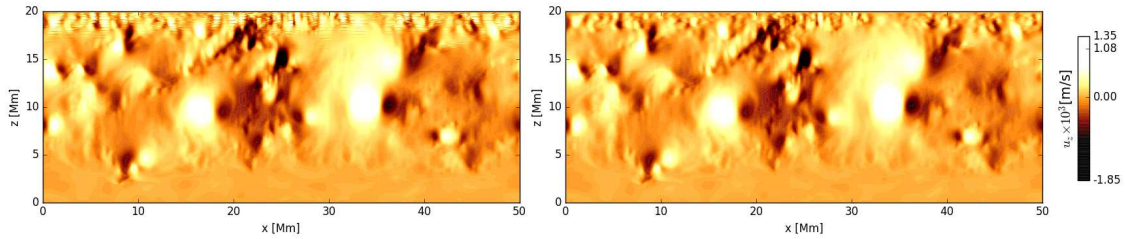

(b)

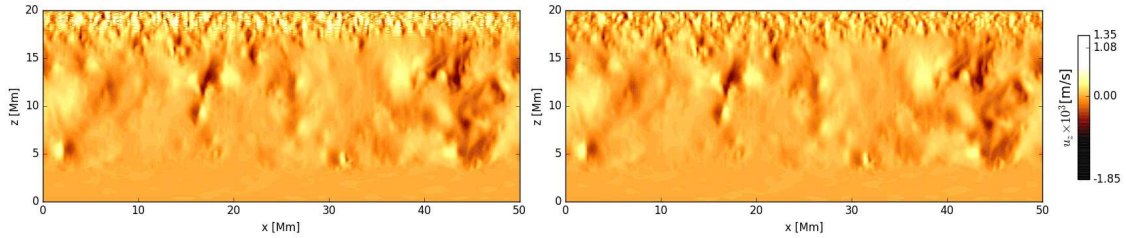

(c)

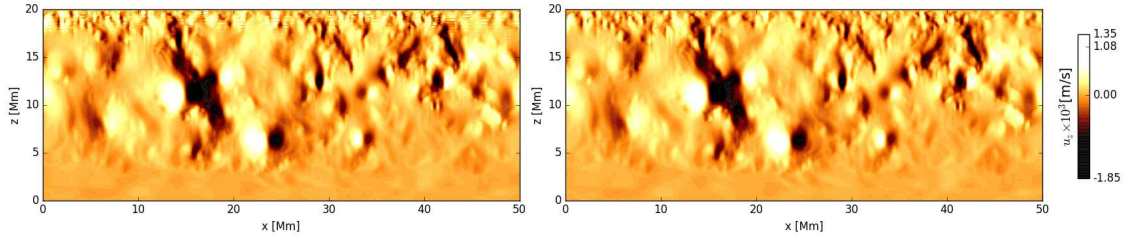

(d)

FIGURE 5.1: x-z slices of the vertical velocity, u_z, for the convective states with relaxation time: a) 100-cf, b) 1000-vf, c) 500-cf, d) 500-vf. Slices on the right and left panels correspond to the filtered and unfiltered data, respectively.

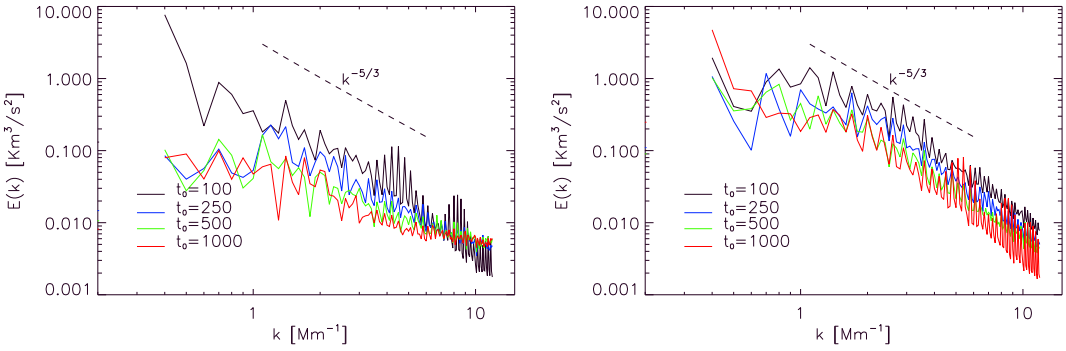

FIGURE 5.2: Kinetic energy spectra for the 2D simulations. Models "cf" and "vf"are show in the left and right panels, respectively. Different colors indicate different values of t_0, as indicated in the legends.

The convective states for which the strong oscillations are observed, **100-cf** and **1000-vf**, are shown in the panels a) and b) of fig. 5.1. Based on the energy spectra shown in fig 5.2, the radial modes should be predominantly visible in these cases (assuming these are related to the observed strong oscillations at large wavenumbers). However, it does not seem to be the case since the "wiggles" can be seen for all the runs considered (compare left and right panels in Fig. 5.1 for each simulation). This indicates that the radial modes do not diminish neither for large nor for small values of the relaxation time. Thus, the question of whether or not the strong oscillations at high wavenumbers in the spectrum are due to the radial modes still deserves further investigation.

The aim is to obtain an hydrodynamical state with a solar-like convection and with a well defined scale separation. Thus, at least two dominant convective scales should be present in the simulation. Among all the cases considered, the one with the most noticeable scale separation is the model **500-cf** (see panel c) in Fig. 5.1). The convective patterns of the other cases show strong vortical flows that modify the dynamics of the downdrafts. These sheared flows move mainly in the horizontal direction and are strong enough so that they can reach the top surface and destroy the small scale dynamics at the near-surface layers. This vortical behavior is not consistent with the current picture of solar convection as explained before in Chapter 1 (See the work of Spruit et al. (1990) and Stein & Nordlund (1989)). The plume-based convective transport is also best reproduced by the model **500-cf**. A tree-like structure for the downflows, where small downdrafts merge to form larger and vertically elongated downflows is observed for this model. However, since the simulation is 2D, it is imposible to observe the wide upflows forming the convection cells surrounded by the downflow lanes in the horizontal directions. Based on these facts, we choose $\tau = 500$ to perform the 3D convection experiments.

Even though the model **500-cf** appears as the most suitable to reproduce solar-like convection, the spectra for the "cf" models appear less suitable for 3D test than the one observed for the "vf" models (notice the bottleneck effect present in the left side spectra of Fig. 5.2). As it will be shown in the next section this represents no issue for the 3D simulations since a well behaved spectra is observed for the HD initial state using the model **500-cf**.

5.1.2 Three dimensional HD simulations

We performed 3D simulations of convection with two different resolutions: 128^3 (low) and 256^3 (high) gridpoints. We use the model **500-cf** that considers a relaxation time $\tau = 1.1$ days ($\tau = 500$ in code units). Here we also observe the appearance of radial modes in the near-surface layers. However, for the 3D case we use a different filter ($F2$) given by:

$$(u_z)_f(i,j,k) = \frac{1}{4}\left[u_z(i,j,k-1) + 2u_z(i,j,k) + u_z(i,j,k+1)\right], \tag{5.4}$$

where $u_z(i,j,k)$ is the vertical component of the flow velocity field at the grid location (i,j,k), and the subscript f indicates filtered data. Vertical slices of the instantaneous vertical velocity in the statistically steady state are shown for the low (high) resolution simulation on the left (right) panels in Fig. 5.3. The unfiltered (filtered) data are shown in the top (bottom) panel.

Similarly to the simulations of Stein & Nordlund (1989) and Kitiashvili et al. (2016), the results indicate that small convective downflows developing at the convectively-unstable layer merge in the adiabatic layer forming a tree-like structure that leads to larger downdrafts. These downdrafts reach the bottom of the adiabatic layer where they are damped by the convectively-stable stratification below. The horizontal slices presented in fig. 5.4 correspond to two different depths for each simulation. They show the standard picture of the solar convection: wide upflows forming convection cells are surrounded by narrow downflow lanes. As expected, the horizontal extent of the cells increases with depth, however, two dominant scales of convection can be identified. These scales are separated by a boundary at about $z \sim 18.0$ Mm, for the low resolution simulation (left panel) and $z \sim 19.0$ Mm, for the high resolution simulation (right panel). The thickness of the layer where the smaller-scale convective motions develop, becomes narrower as the resolution increases. This can be seen in the vertical slices, by comparing the cell size at both depths for each simulation.

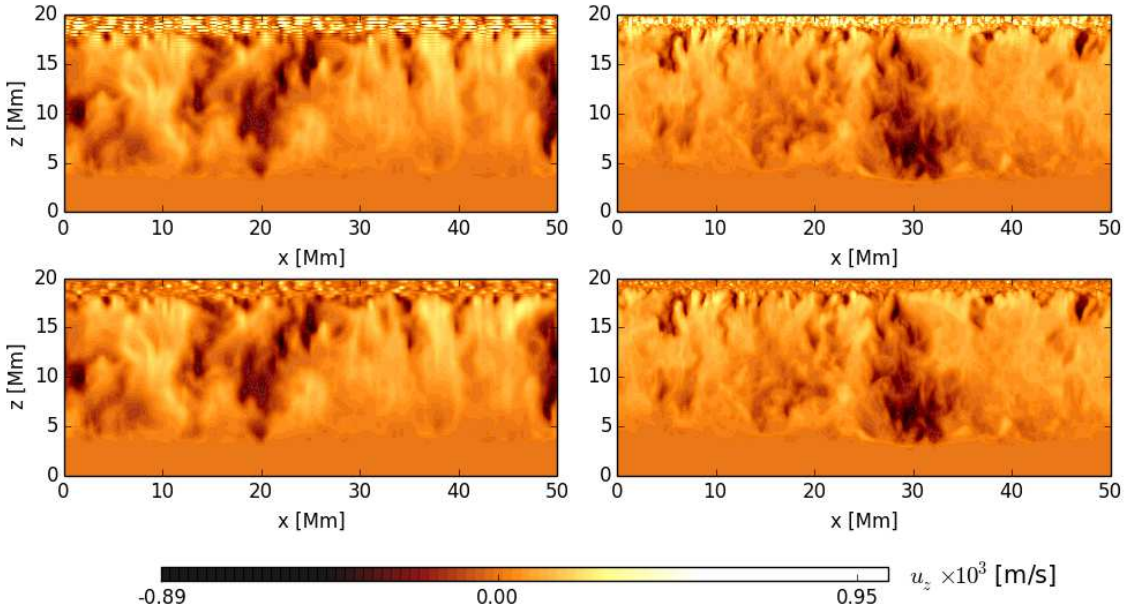

FIGURE 5.3: Instantaneous x-z slices of the radial component of velocity, u_z, corresponding to the low (high) resolution simulation in the left (right) panels. The unfiltered (filtered) results are in the top (bottom) panel.

To determine more precisely the dominant scales of convection, the spectrum of the kinetic energy is calculated at different heigths as a function of the horizontal wavenumber $k_\perp^2 = k_x^2 + k_y^2$ (See Figure 5.5). In this case the spectrum is computed by using:

$$E(k_\perp, z, t) = \frac{1}{2} \sum_{k_x^2+k_y^2=k_\perp^2} |\hat{u}(k_x, k_y, z, t)|^2, \tag{5.5}$$

where $\hat{u}$ is the horizontal Fourier transform of the velocity field. Note that near the upper boundary, the spectrum does not exhibit an inertial range (blue lines in Figure 5.5). This might be due to insufficient resolutions that do not capture the inertial turbulent scales within that layer. The dominant scales can be estimated by identifying the wavenumbers where the power spectra have maxima. For the low resolution simulation (left panel of Figure 5.5), two peaks are observed. At $z = 18.8$ Mm (blue line) the peak is at a wavenumber $k_\perp \sim 3$ Mm^{-1} which corresponds to a length of nearly 2.1 Mm. At $z = 15.6$ Mm (purple line) the other peak is observed at a smaller wavenumber, $k_\perp \sim 0.3$ Mm^{-1}. It corresponds to a length of approximately 20.9 Mm. The red line in the middle corresponds to $z = 18.0$ Mm where the boundary between the adiabatic and the convectively-unstable layers is located. As expected, it is the depth where the transition between the two scales of convection is observed.

A similar pattern, i.e., two peaks, is observed in the power spectra corresponding to the

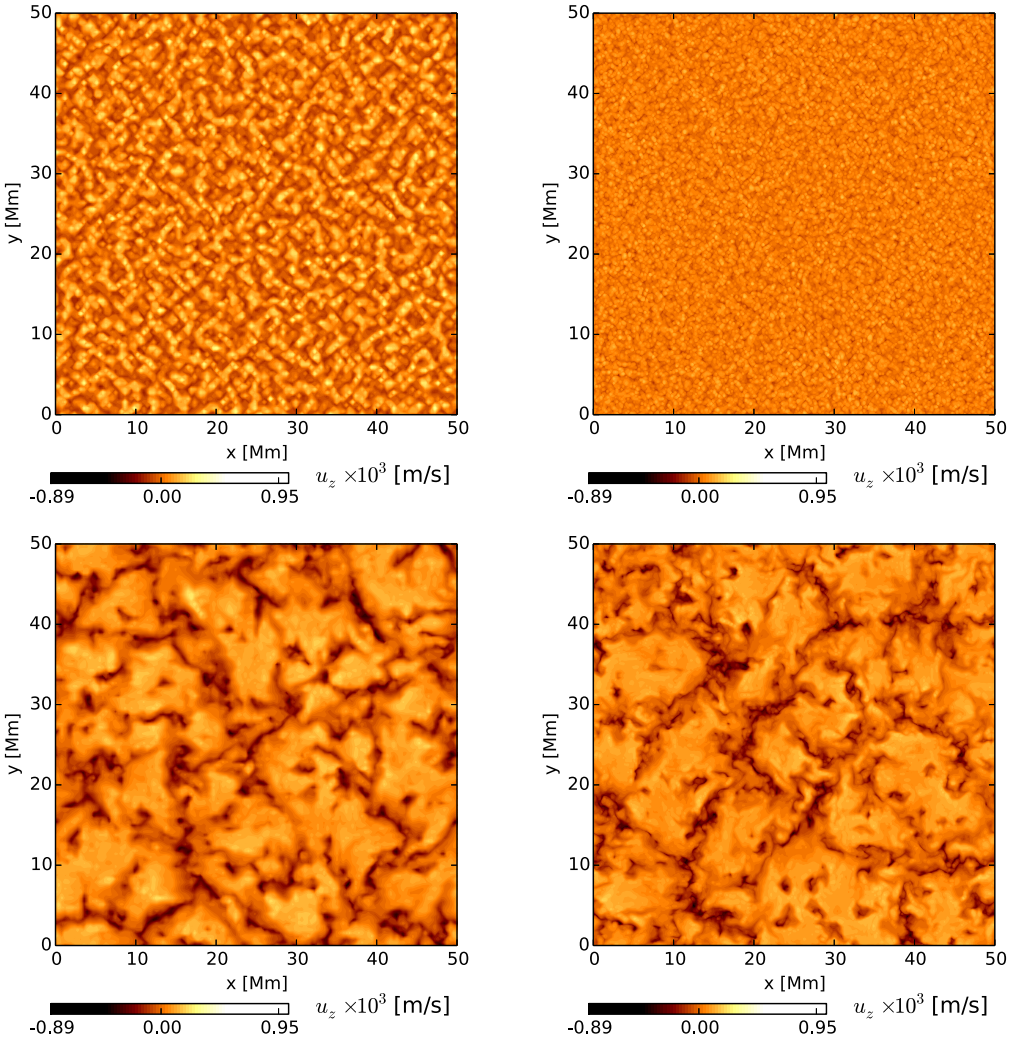

FIGURE 5.4: x-y cuts of the radial velocity, u_z. The *left)* (*right)*) panels correspond to the low, 128^3 grid poings (high, 253^3 grid points) resolution simulation. The top and bottom panels show x-y cuts at depths of 1 and 2 Mm below the top boundary, respectively.

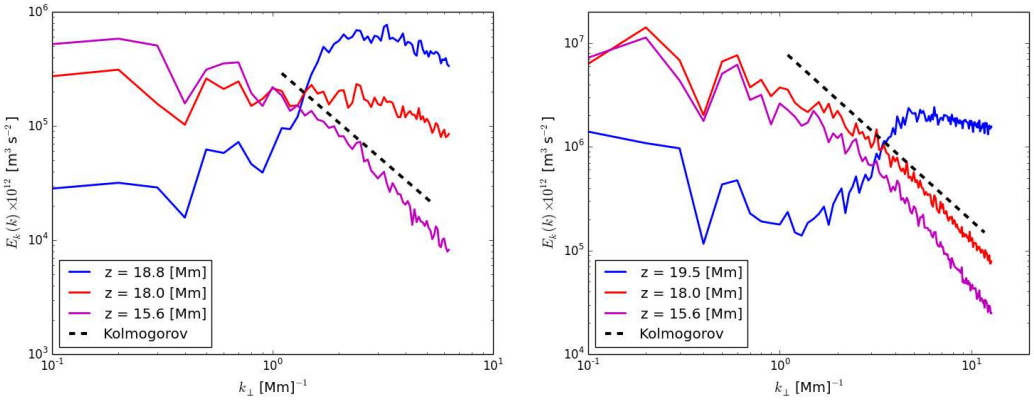

(a) (b)

FIGURE 5.5: Kinetic energy spectra for the HD 3D simulations: *left)* low resolution simulation, *right)* high resolution simulation.

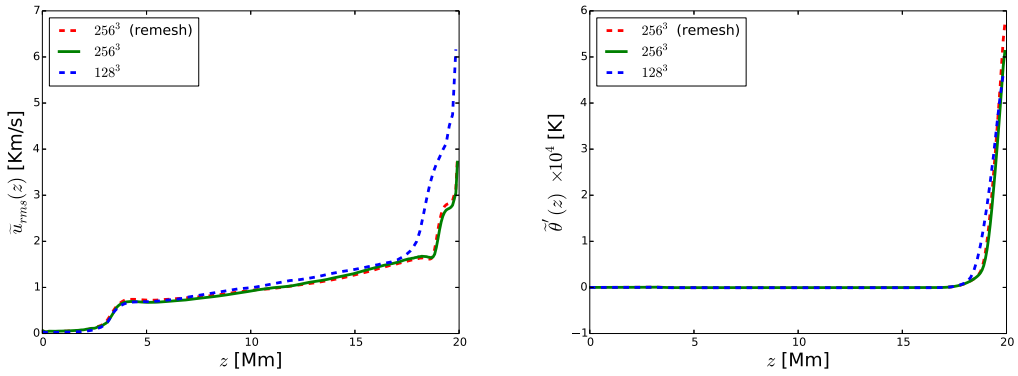

(a) (b)

FIGURE 5.6: Vertical profiles of horizontally averaged *a)* root mean squared velocity fluctuations, u_{rms}, and *b)* potential temperature fluctuations, θ'.

high resolution simulation, (right panel of Figure 5.5). One peak is located at $k_\perp \sim 6$ Mm^{-1} at a depth of $z = 19.0$ Mm (blue line). It corresponds to a length scale of about 1 Mm. For the depths below $z = 18$ Mm, the second peak is located at $k_\perp \sim 0.3$ Mm^{-1}, corresponding to a length scale of 20.9 Mm. This means that increasing the numerical resolution, modifies mostly the convective pattern at small scales. This fact is more evident in the radial profiles of the horizontally averaged rms velocity and potential temperature fluctuations shown in Figure 5.6. The horizontally averaged rms velocity is computed as:

$$(\widetilde{u}_i)_{rms} = \sqrt{\langle u_i^2 \rangle_{xy} - \langle u_i \rangle_{xy}^2}, \tag{5.6}$$

and the horizontally averaged fluctuations of the potential temperature are:

$$\widetilde{\theta}' = \langle \theta' \rangle_{xy}, \tag{5.7}$$

with θ' given by eq. 4.2. By comparing the blue (low resolution case) with the green (high resolution) lines in Figure 5.6, it is evident that changes in $(\widetilde{u}_i)_{rms}$ and $\widetilde{\theta}'$, from one simulation to another are significant only at the upper part of the domain. The red dashed lines represent the radial profiles from a convection model obtained by remeshing a HD simulation of 128^3 gripoints to the resolution of 256^3 gridpoints, which we run further until reaching a statistically steady state. As expected, the resulting model turns out to be similar to the high resolution simulation. This numerical experiment was done to take advantage of the low resolution model in terms of the faster relaxation time, and shorter computing time.

5.2 Simulations with imposed magnetic field

Strong effects of the negative effective magnetic pressure on the formation of shallow magnetic structures have been reported in simulations of isothermal forced turbulence with imposed vertical magnetic field (Brandenburg et al., 2014; Losada et al., 2014). The authors argue that the advantage of considering an external vertical field is that it is not advected by the convective downflows, i.e., the so-called potato-sack effect observed in simulations with imposed horizontal field (Kemel et al., 2013; Brandenburg et al., 2011) is not present. As a first step, in this work we impose a uniform vertical magnetic field, $\vec{B} = (0, 0, B_0)$, with three different strengths, permeating the convective patterns obtained from the HD simulations. We will refer to the HD simulations performed at low resolution (128^3 gridpoints) as **HD-LR**, and at high resolution (256^3 gridpoints) as **HD-HR**. The three different strengths for the imposed magnetic field are $B_0/B_{eq} = (0.01, 0.1, 0.5)$, for the **HD-LR** simulation, and $B_0/B_{eq} = (0.05, 0.1, 0.5)$, for the **HD-HR** simulation. Here, B_{eq} is the mean equipartition magnetic field given by:

$$\frac{1}{2\mu_0} B_{eq}^2 = \frac{1}{2} \overline{\rho} u_{rms}^2, \tag{5.8}$$

where u_{rms} is the volume averaged rms turbulent velocity computed from the HD simulations, and $\overline{\rho}$ is the mean density of the ambient state. The low resolution MHD simulations are denoted by **MHD-LR-0.01**, **MHD-LR-0.1** and **MHD-LR-0.5**. The number at the end of the notation name accounts for the amplitude of the external magnetic field. In a similar way, the high resolution simulations are denoted by **MHD-HR-0.05**, **MHD-HR-0.1** and **MHD-HR-0.5**. Like in the HD case, we compute the MHD kinetic and magnetic energy spectra of the flow at different depths (see eq. 5.5). A time series of the rms magnetic field is shown in the inset of the kinetic energy spectra (see Figures 5.7 and 5.11 for the low and high resolution simulations, respectively). For each depth, the spectrum is calculated for three different times (depending on the temporal evolution of the corresponding magnetic structures observed in each simulation) represented by continuous, dotted and dashed lines, respectively.

5.2.1 Low resolution simulations

From the three low resolution simulations, only model **MHD-LR-0.1** revealed localized magnetic structures. Thus, slices in the x-z plane of the vertical component of the velocity and magnetic fields are shown only for this simulation. In the simulation **MHD-LR-0.1**, the formation of a compact ($\sim$ 6 Mm in diameter) and well-defined magnetic flux concentration is observed. The magnetic structure develops approximately at the horizontal domain center about 1.24 days after the external magnetic field was imposed

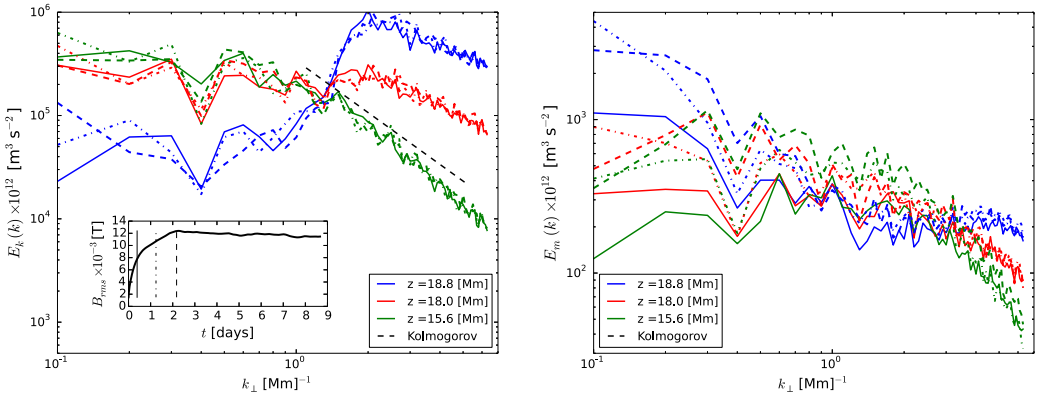

FIGURE 5.7: Kinetic and magnetic energy spectra for the simulation **MHD-LR-0.1**. The spectra were computed at the same depths considered in Figure 5.5. The different line-styles (solid, dotted and dashed) correspond to different times as shown by the vertical cuts in the inset of the left panel.

as can be seen in Figures 5.8 and 5.9. This magnetic structure becomes stronger as it evolves until $t = 2.17$ days. After that, it starts decaying and loses its coherence. At heights around $z = 18.8$ Mm, the convection cells near the magnetic structure lose their regular structure, and acquire a horizontally elongated shape directed towards the center of the magnetic flux concentration (see Figure 5.8). This is reminiscent to the elongated granules that form the penumbra observed around sunspots (Borrero & Ichimoto, 2011).

At deeper layers ($z < 15.6$ Mm), the magnetic structure becomes more intense, but the corresponding large convective cells remain unmodified (see Figure 5.9). Vertical slices, plotted at $y = 28.0$ Mm in Figure 5.10, reveal that the magnetic structure is stronger at heights around $z = 10$ Mm and that its vertical length scale is comparable to the entire convective region, reaching the boundary with the convectively-stable layer. The kinetic energy spectrum corresponding to this simulation does not change appreciably with respect to the pure HD case (see left panel of Figure 5.7). Here, the dominant scales of convection remain unmodified as the simulation evolves. The rms magnetic fluctuations shown in the inset of the left panel of Figure 5.7 show that B_{rms} grows up to a maximum field strength of about 12 $\times 10^{-3}$ T within the first 2 days. After this time it starts to decay slowly. Two power peaks, at heigths around $z = 18.8$ Mm are observed in the magnetic energy spectra (see blue lines in the right panel of Figure 5.7). The power peak located at large wavenumbers ($k_\perp \sim 4$ Mm^{-1}) is weaker compared to the other peak at small wavenumbers ($k_\perp \sim 0.5$ Mm^{-1}). The later corresponds to a length scale of 12.6 Mm. Besides, an increase of magnetic energy is observed only for small wavenumbers, i.e., for the large scales. Thus, this peak might be related to the magnetic structure observed, with horizontal scales between 6 and 15 Mm.

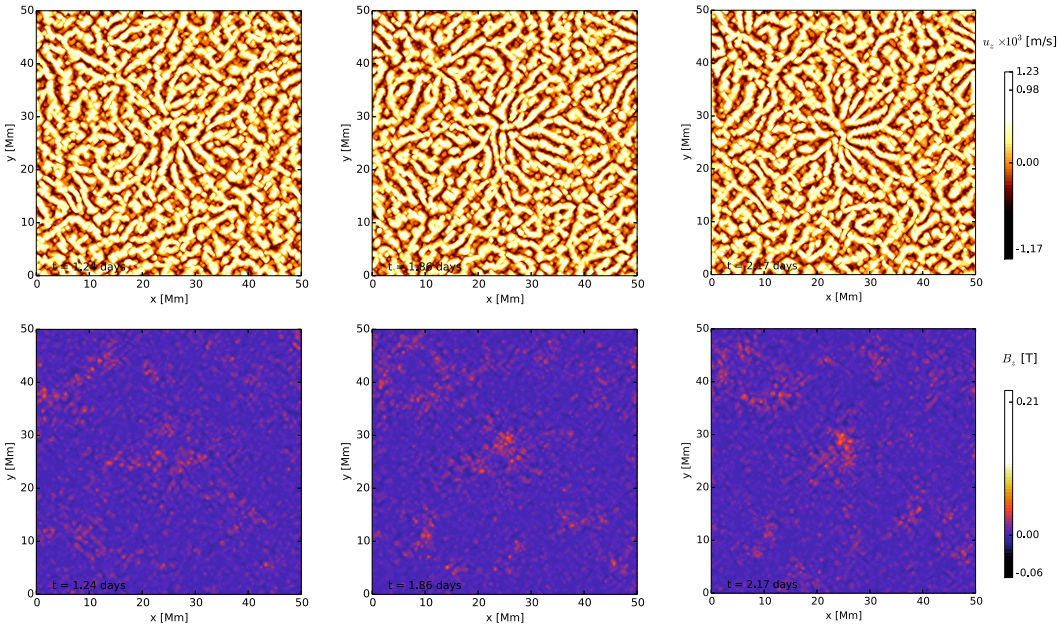

FIGURE 5.8: xy cuts (at $z = 18.8$ Mm) of the vertical velocity and magnetic field at different times for simulation **MHD-LR-0.1**.

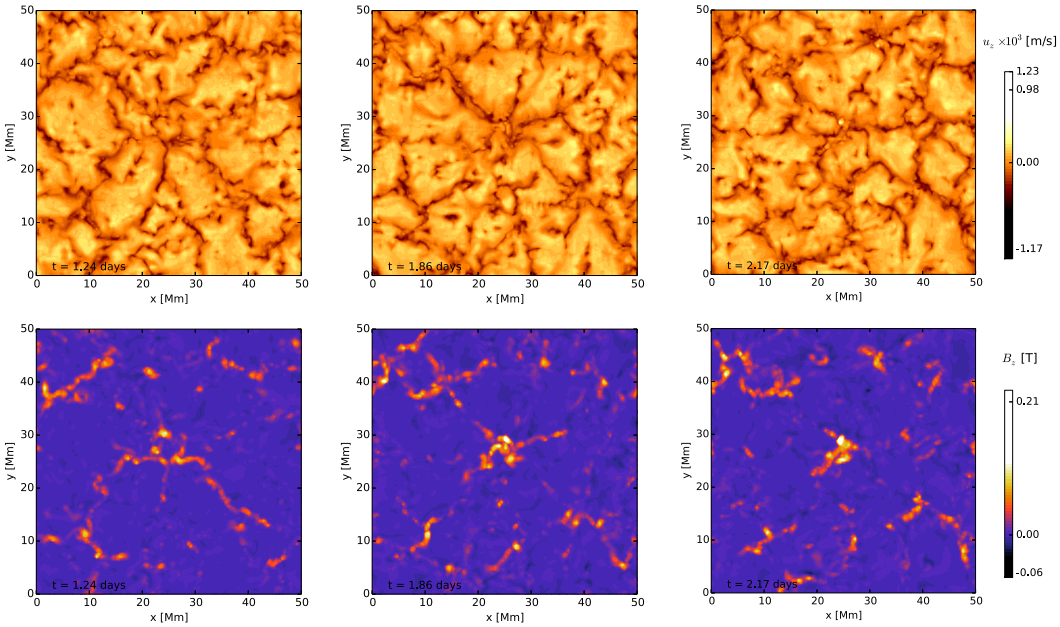

FIGURE 5.9: xy cuts (at $z = 15.6$ Mm) of the vertical velocity and magnetic field at different times for simulation **MHD-LR-0.1**.

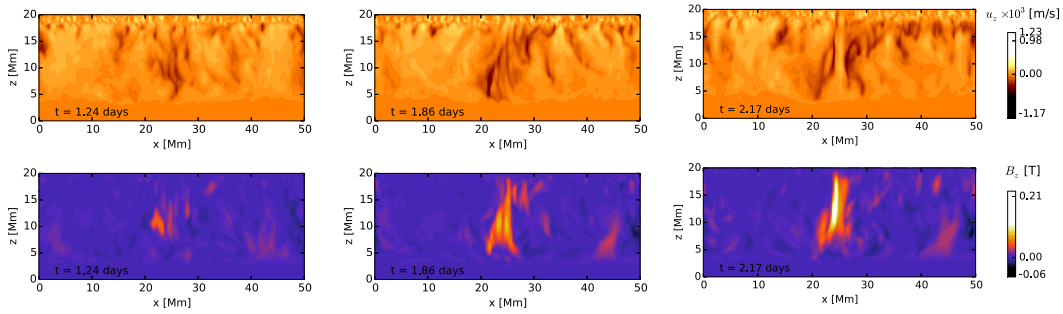

FIGURE 5.10: xz cuts (at $y = 28.0$ Mm) of the vertical velocity and magnetic field at different times for simulation **MHD-LR-0.1**.

In simulation **MHD-LR-0.01**, no significant magnetic structures are observed. However, at $z < 18.0$ Mm, narrow flux tube-like structures develop approximately 1 day after the imposition of the external field. The flux tubes appear inside the downflow lanes and tend to be distributed along them between the large convective cells. The convective patterns do not change significantly suggesting that these structures could possibly be due to flux expulsion. Since no important magnetic flux concentrations are observed in **MHD-LR-0.01**, this simulation is not considered for further analysis of the magnetic structure formation mechanism.

In simulation **MHD-LR-0.5**, intense but non-localized magnetic structures are observed. At heights around $z = 18.8$ Mm, very diffuse and large magnetic lane-like structures develop. Here, as the magnetic lanes develop, they adopt the form of the downflow lanes between the neighbour convective cells at deeper layers ($z \sim 15.6$ Mm). Simultaneously, the convective cells are destroyed as the strong magnetic lanes seem to inhibit the motion of the downflow lanes. Since the convective structure is destroyed by the magnetic lanes, we do not explore further this simulation.

5.2.2 High resolution simulations

From the three high resolution simulations performed, only **MHD-HR-0.05** and **MHD-HR-0.1** reveal the formation of magnetic flux concentrations at the upper layers of the domain. In **MHD-HR-0.05**, several magnetic structures are formed. The convective patterns nearby the magnetic flux concentrations form a penumbra-like structure, similar to the one observed in the low resolution simulation **MHD-LR-0.1**. At heights around $z = 18.8$ Mm, the concentrations start to appear at about 0.78 days after imposing the vertical magnetic field (see Figure 5.12). These structures grow in strength and become more locatized as the simulation evolves until $t = 1.55$ days, when they start decaying and spread along thin filaments as shown in the slices corresponding to $t = 2.33$ days and $t = 3.11$ days in Figure 5.12. In deeper layers, the magnetic flux

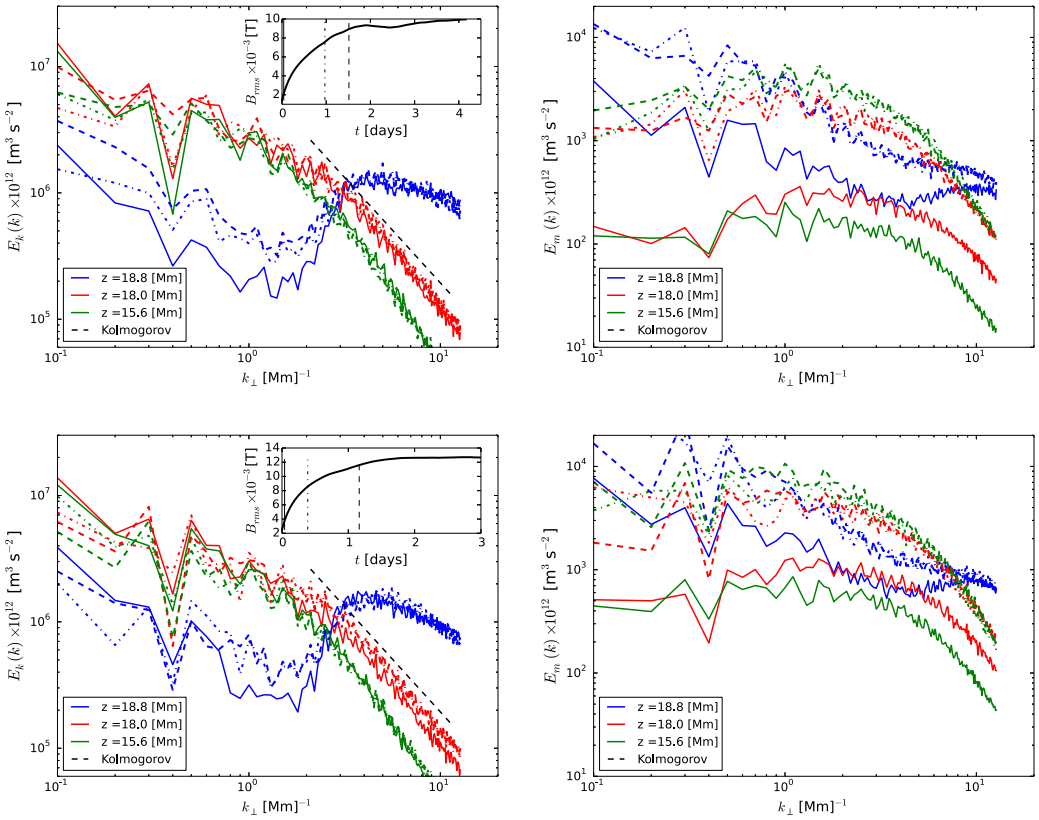

FIGURE 5.11: Kinetic and magnetic energy spectra for the high resolution simulations. The top panels correspond to **MHD-HR-0.05** and the bottom panels correspond to **MHD-HR-0.1**. The spectral profiles are taken at the same depths considered for the high resolution progenitor simulation shown in Figure 5.5. For each simulation the left (right) panel corresponds to the kinetic (magnetic) energy spectra. The different line-styles (solid, dotted and dashed) correspond to different times as shown by the vertical cuts in the inset of the each left panel.

concentrations have a filamentary structure (see Figure 5.13), and the filaments tend to appear along the downflow lanes between the large convective cells. These cells do not have the elongated penumbra-like form observed in the upper layers of the domain. Instead, it seems that the size of these convective cells at this depth determine the shape of the magnetic filamentary structures. At $z = 15.6$ Mm, the filamentary structures become clear enough for us to recognize that they develop mostly at regions where the downdrafts are stronger, as shown in the horizontal slices corresponding to $t = 0.78$ days and $t = 1.55$ days in Figure 5.13. Vertical slices of the radial magnetic field (see Figure 5.14) show that the magnetic structures in this simulation are vertically elongated, and that they cross the entire adiabatic layer in a similar fashion as in the low resolution simulations.

Certain changes are observed in the kinetic energy spectra of the **MHD-HR-0.05** run. In the upper layers the energy for wavenumbers smaller than $k_\perp = 3$ Mm^{-1} decreases

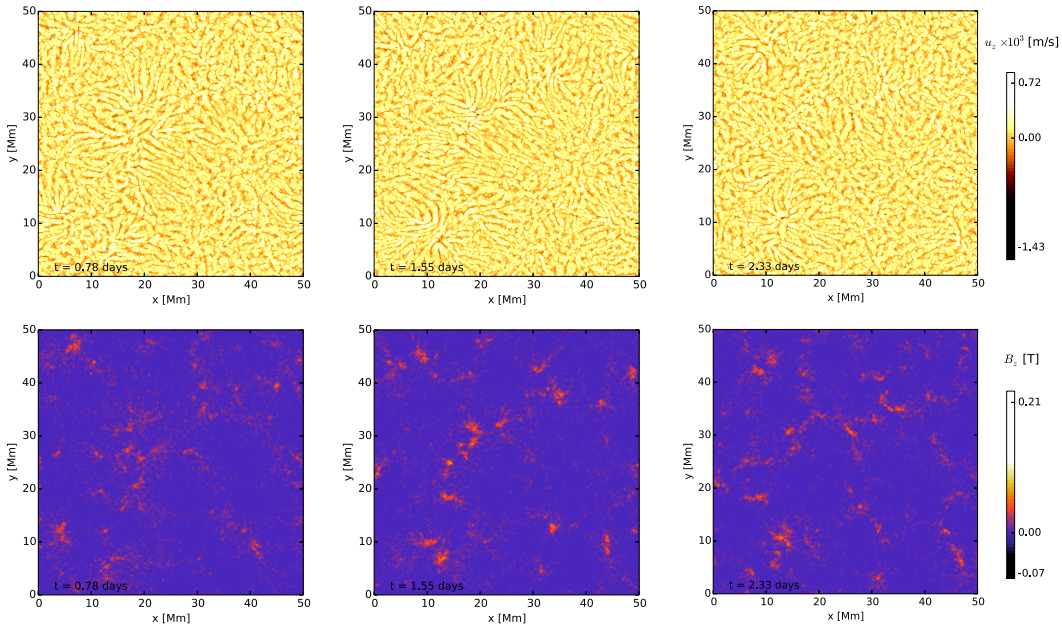

FIGURE 5.12: xy cuts (at $z = 18.8$ Mm) of the vertical velocity and magnetic field at different times for simulation **MHD-HR-0.05**.

(see blue lines on the left side of top panel in Figure 5.11). This leads to a power peak located at about $k_\perp \sim 0.5$ Mm^{-1} corresponding to horizontal scales around 12.6 Mm. The fact that this energy increment at small wavenumbers is not observed in the simulation **MHD-LR-0.1** suggests that the penumbra-like pattern has no correlation with this power peak.

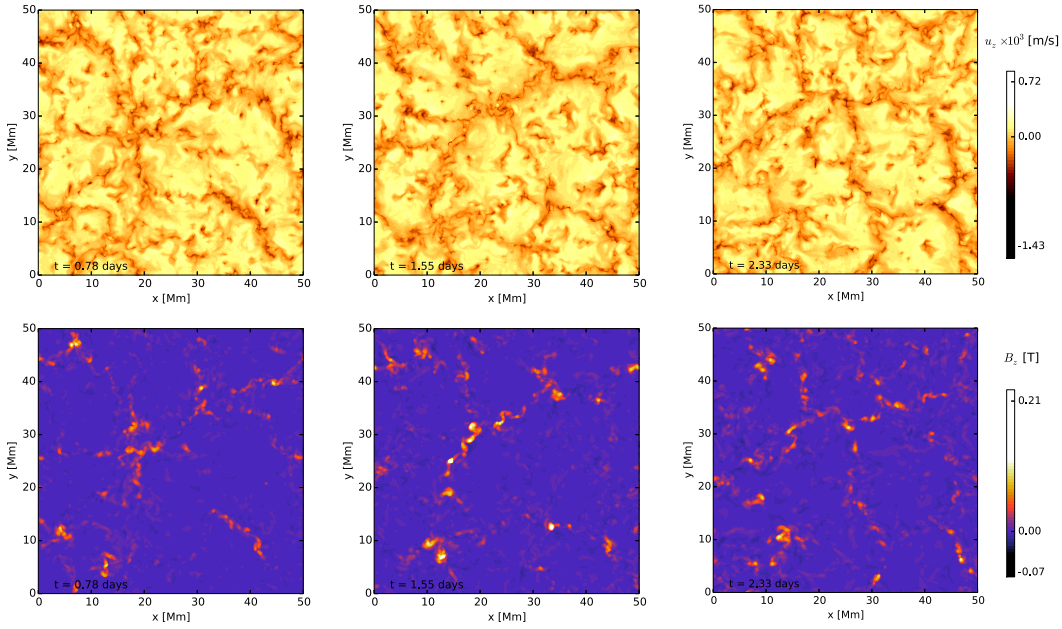

FIGURE 5.13: xy cuts (at $z = 15.6$ Mm) of the vertical velocity and magnetic field at different times for simulation **MHD-HR-0.05**.

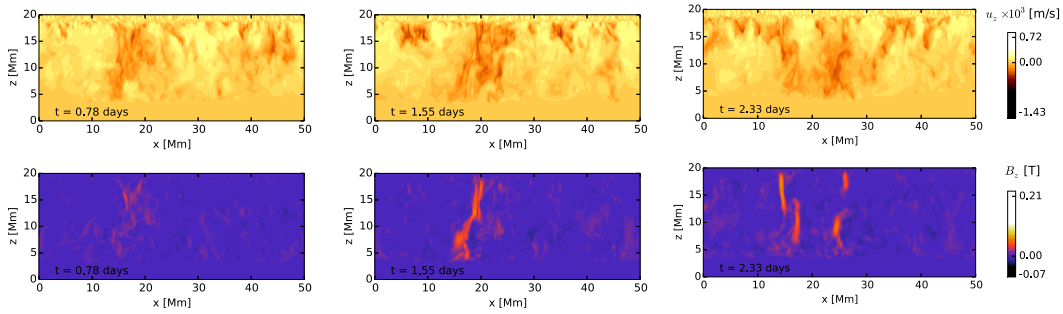

FIGURE 5.14: xz cuts (at $y = 30.5$ Mm) of the vertical velocity and magnetic field at different times for simulation **MHD-HR-0.05**.

The inset in the lhs of top panel of Figure 5.11 shows that the magnetic flux concentration in this simulation develops within the first 2 days. The B_{rms} reaches a value around 10 $\times 10^{-3}$ T. However, for the time that the simulation was run (4 days) it did not reach a statistically stationary phase. Thus, so far it is not possible to estimate with certainty the value of B_{rms} in the stationary state. The magnetic spectra show that the energy increases at all scales. The increment is larger for the smaller wavenumbers (see right side of top panel in Figure 5.11). Two power peaks are observed at $z = 18.8$ Mm. However, unlike the low resolution simulations, the power peak at large wavenumbers tends to disapear as the flux concentration develops. The location of the power peak at deeper layers lies within the wavenumbers $k_\perp = 0.5$ and $k_\perp = 1.0$ Mm^{-1}, which corresponds to the range of lengthscales of the filamentary structures observed in the adiabatic layer.

The results of simulation **MHD-HR-0.1** show that the magnetic structures are slightly stronger than in the corresponding low resolution case, **MHD-LR-0.1**. The horizontal slices taken at $z = 18.8$ Mm (see Figure 5.15), reveal that the magnetic structures appear about 0.39 days after turning on the vertical magnetic field. They are rather disperse and tend to appear irregularly over the entire horizontal plane. An intricate network of elongated convection cells is also present. Locally, the direction of the elongated cells points towards the most intense magnetic structures, similar to the penumbra-like regions observed in **MHD-LR-0.1**. In deeper layers, the magnetic flux concentrations form the filamentary structure previously observed at low resolution (see Figure 5.16). The $x - z$ slices presented in Figure 5.17 reveal a vertically elongated shape for the magnetic flux concentrations. However, in this case the vertical filaments seem to reach the surface layers without decaying as much as observed in the low resolution case. The kinetic (magnetic) energy spectra of this simulation, shown in the left (right) side of bottom panel in Figure 5.11, exhibit changes similar to simulation **MHD-HR-0.05**. The inset in the lhs of the bottom panel of the same figure shows that B_{rms} grows up to a value of 12 $\times 10^{-3}$ T within 1.6 days.

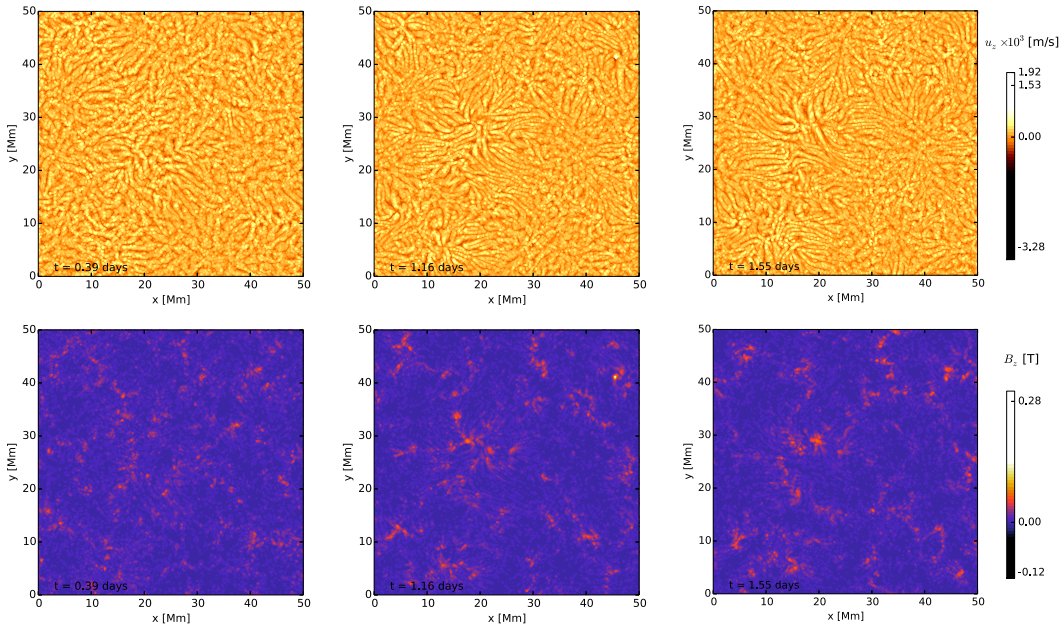

FIGURE 5.15: xy snapshots (at $z = 18.8$ Mm) of the vertical velocity and magnetic field at different times for simulation **MHD-HR-0.1**.

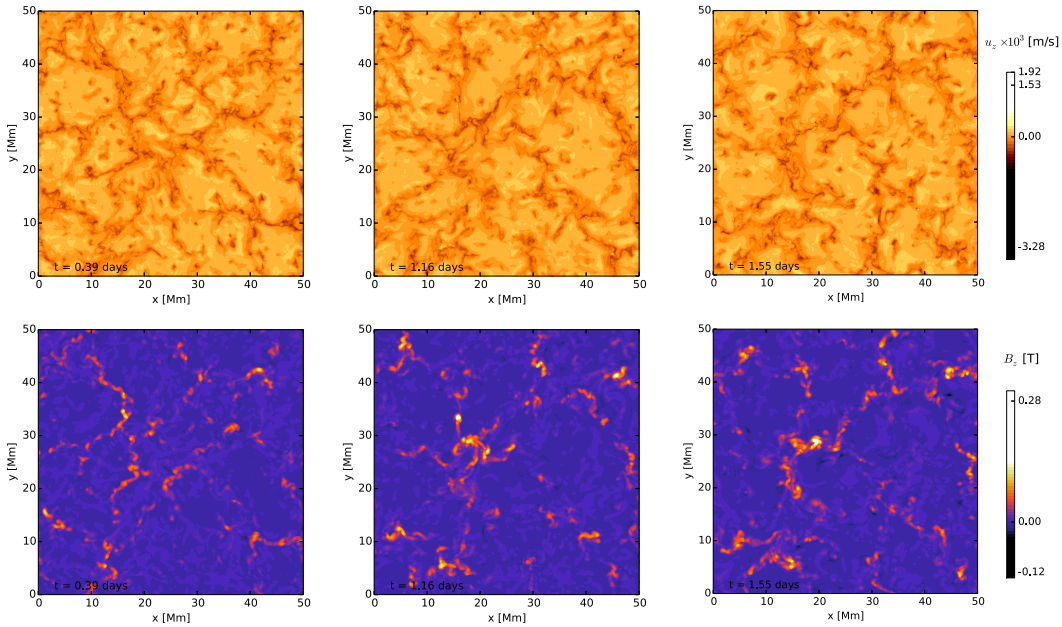

FIGURE 5.16: xy snapshots (at $z = 15.6$ Mm) of the vertical velocity and magnetic field at different times for simulation **MHD-HR-0.1**.

In simulation **MHD-HR-0.5**, structures develop in the form of magnetic lanes such as it is observed in the low resolution simulations. In this case they develop faster than in the low resolution case. However, soon after this happens, the convective pattern is distorted by the external field in such a way that no more structure is evident. For this reason, we don't analyze this simulation in detail.

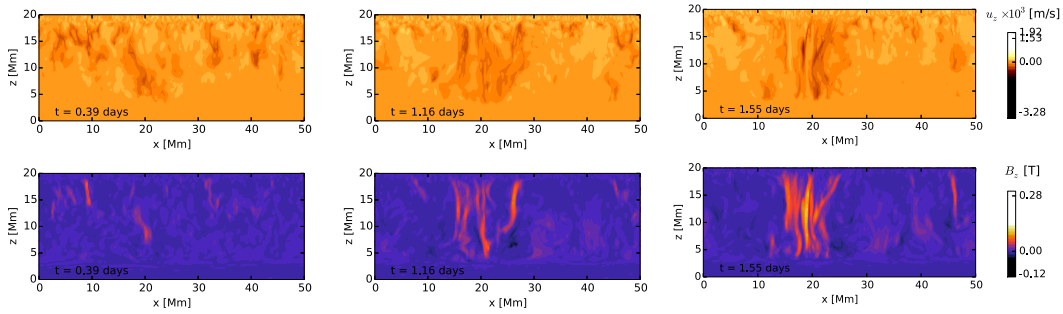

FIGURE 5.17: xz snapshots (at $y = 29.0$ Mm) of the vertical velocity and magnetic field at different times for simulation **MHD-HR-0.1**.

5.2.3 Calculation of NEMPI coefficients

The method by which the presence of NEMPI is determined follows the same approach taken by Käpylä et al. (2016). To find the coefficients that characterize NEMPI in our simulations, we need to use eq. 2.51 to compute the tensor, $\Delta\Pi_{ij}^{(f)} = \Pi_{ij}^{(f,\overline{B})} - \Pi_{ij}^{(f,0)}$. Here, $\Pi_{ij}^{(f,0)}$ is calculated from the progenitor HD simulation and $\Pi_{ij}^{(f,\overline{B})}$ comes from the corresponding MHD simulation with external vertical magnetic field. The tensors mentioned above are given as follows:

$$\Pi_{ij}^{(f,0)} = \overline{\rho}\overline{(u_0)_i\,(u_0)_j} + \frac{1}{2\mu_0}\delta_{ij}\overline{b_0^2} - \frac{1}{2\mu_0}\overline{(b_0)_i\,(b_0)_j} \tag{5.9}$$

$$\Pi_{ij}^{(f,\overline{B})} = \overline{\rho u_i u_j} + \frac{1}{2\mu_0}\delta_{ij}\overline{b^2} - \frac{1}{2\mu_0}\overline{b_i b_j}, \tag{5.10}$$

where the overbar indicates horizontal average (over the x-y plane). The lowercase letters denote the turbulent part of the fields and the subscript "0" denotes the values of the fields from the progenitor HD simulation which in general are different from zero ($(b_0)_i \neq 0$). The coefficient that determines whether there is a negative effective magnetic pressure is q_p (see eqs. (2.31) and (2.44)), thus, we only compute this coefficient. To do that, it is enough to take the x component of eq. (2.51), which leads to:

$$q_p = -2\mu_0\Delta\Pi_{xx}^{(f)}/\overline{B}^2. \tag{5.11}$$

This gives the coefficient q_p as a function of z. The profiles of $q_p(z)$ are calculated for each of the MHD simulations discussed in the previous sections at three different times (the same times considered for the corresponding kinetic and magnetic energy spectra), the results are shown in Fig. 5.18. The simulations **MHD-LR-0.01**, **MHD-LR-0.1** and **MHD-LR-0.5** are shown in the upper left, middle and right panels, respectively.

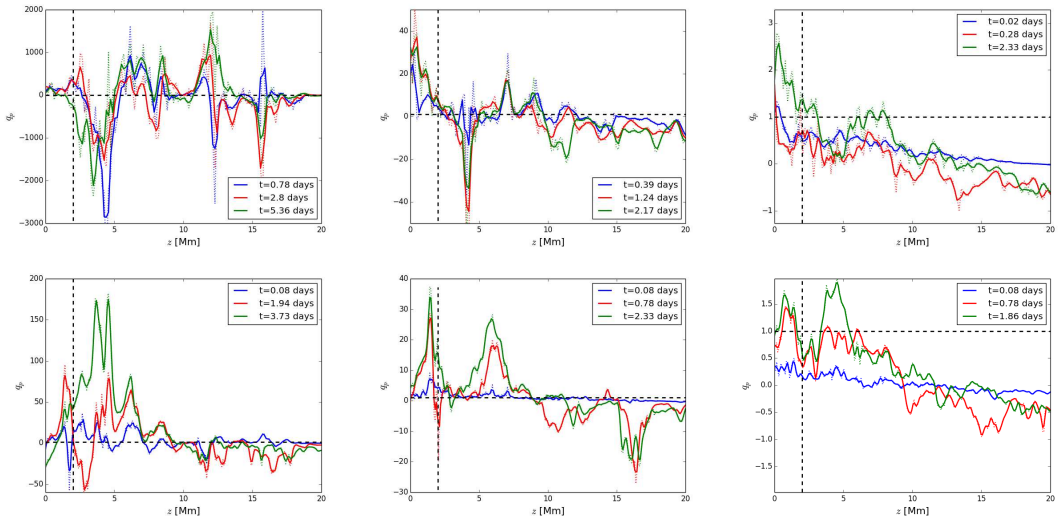

FIGURE 5.18: Profiles of $q_p(z)$ for the MHD simulations. The results for the simulations **MHD-LR-0.01**, **MHD-LR-0.1** and **MHD-LR-0.5** are shown on the upper left, middle and right panels. The simulations **MHD-HR-0.05**, **MHD-HR-0.1** and **MHD-HR-0.5** are shown on the bottom left, middle and right panels. The vertical black dashed line indicates the location of the convectively-stable layer, and the horizontal black dashed line indicates the limit $q_p = 1$.

In a similar way, the simulations **MHD-HR-0.05**, **MHD-HR-0.1** and **MHD-HR-0.5** are shown on in the bottom left, middle and right panels, respectively. The vertical black dashed line indicates the location of the convectively-stable layer at the bottom of the domain, and the horizontal black dashed line indicates the limit $q_p = 1$. Here, the effective magnetic pressure is negative when $q_p > 1$. For both, low and high resolution simulations, it can be seen that the maximum and minimum values of q_p become smaller in magnitude as the strength of the external vertical magnetic field increases. This result is in agreement with earlier findings by Brandenburg et al. (2010), where it is seen that the volume averaged q_p becomes smaller as $\overline{B}/B_{eq}$ increases (see Fig. 2.1).

For the simulation **MHD-LR-0.01**, values of q_p greater than unity are detected at several locations within the adiabatic layer. The largest (positive) values of q_p can be seen at the peak located around $z = 12$ Mm. Other peaks somewhat weaker are observed at deeper layers. However, for this simulation no significant magnetic structures are observed, thus, if NEMPI is operating on this simulation it is unable to form large magnetic flux concentrations relevant for the study of sunspot formation.

For the simulation **MHD-LR-0.1**, positive values of q_p within the adiabatic layer are detected in the range $5 < z < 10$ Mm (see middle of top panel in Fig. 2.1). As mentioned before, the vertical slices of B_z shown in Fig. 5.10, indicate that the magnetic flux concentration is stronger at $z = 10$ Mm. This means that the peaks of q_p observed in this case could be related with the magnetic structure observed. Larger values of q_p are detected within the convectively-stable layer, however this layer is of no interest as

convection does not take place there. In the near-surface layers the coefficient q_p is less than 1, with values that become more negative as time advances, showing that NEMPI is not operating in the uppermost part of the domain. For the simulation **MHD-LR-0.5**, values of the coefficient q_p considerably greater than unity are detected only below the adiabatic layer, indicating that NEMPI is definitively not operating in this simulation.

For the high resolution simulations a similar behavior is observed. For the simulation **MHD-HR-0.05**, large values of q_p (greater than unity) are detected mostly in the deepest part of the adiabatic layer ($2 < z < 9$ Mm) and within the convectively-stable layer. There is also an interval, $12 < z < 18$ Mm, where the values of q_p are not so large, yet they are greater than unity. Comparing with the vertical slices shown in Fig. 5.14 the location of the strongest magnetic field inside the magnetic structure matches the intervals of z where $q_p > 1$ (see the slice for $t = 1.55$ days in the bottom panel of Fig. 5.14). Even though the magnetic structures in this simulation have a small horizontal extent, their formation could be related to the presence of a negative effective magnetic pressure.

For the simulation **MHD-HR-0.1**, values of q_p greater than unity, within the adiabatic layer, are detected in the interval $2 < z < 9$ Mm. However in this case, the interval for which the largest values of q_p are detected does not match the location of the strongest magnetic field inside the magnetic structure observed (see the slice for $t = 1.16$ days in the bottom panel of Fig. 5.17). Thus, the correlation of the magnetic structures observed in this simulation with the presence of a negative effective magnetic pressure is unclear. For the simulation **MHD-HR-0.5**, a small peak of q_p with values larger than unity is observed at the deepest part of the adiabatic layer ($z \sim 4$ Mm) for $t = 1.86$ days. Even though, for this simulation we do not observe localized magnetic flux concentrations, the appearance of a positive peak in the q_p profile for $t = 1.86$ days indicate that a magnetic structure might be able to develop just after the simulation finished. In this case, we will need to run for a longer time the simulation to clarify this fact.

Chapter 6

Conclusions and future work

We performed 3D magnetoconvection simulations in the anelastic approximation, using the code EULAG-MHD for two different resolutions, 128^3 and 256^3 gridpoints. We use a three-layer polytropic stratification for the background state. The background stratification is mostly adiabatic except for a convectively-stable layer at the bottom and a convectively-unstable layer at the top. Convection is driven by the strong downdrafts generated in the thin convectively-unstable layer in the upper part of the domain. Two dominant scales of convection, separated by a transition layer at $z \sim 18.0$ Mm for the low resolution simulation and at $z \sim 19.0$ Mm for the high resolution simulation are identified. The convection obtained from the pure HD simulations may be considered as a simplified version of the realistic models of Stein & Nordlund (1989) and Kitiashvili et al. (2016). The horizontal extent of the convection cells increases with depth as the downflows merge forming larger structures. These structures seem to be essential for the appearance of magnetic structures. The simulations with imposed vertical magnetic field reveal that there is an optimal range of field strengths, $0.01 < B_0/B_{eq} < 0.5$, for the formation of localized magnetic flux concentrations. The structures are rather disperse at the layer where the convection cells are small ($z > 18.0$, Mm for the low resolution case and $z > 19.0$ Mm for the high resolution case). At deeper layers, within the adiabatic layer of the domain, the magnetic flux concentrations have a well-defined boundary encompassing horizontal lengths between 6 and 15 Mm. Vertically, these structures have the length scale of the entire adiabatic layer.

For the simulations that show the formation of magnetic flux concentrations, an important change in the form of the convective cells is observed. At the upper layers ($z > 18.8$ Mm), the convective cells near the magnetic flux concentrations acquire a elongated form pointing towards the center of these structures. As pointed out before, these convective cells are reminiscent of the penumbrae filaments around the dark center of sunspots

(Borrero & Ichimoto, 2011). For the moment, it is not clear whether these structures are the results of MHD instabilities or the collapse of the magnetic flux within the downflow lanes. Since the downflows have the horizontal scale of the deep convective motions, the magnetic elements at the surface cover several small-scale convective elements. Even though magnetic structures are observed at relatively large imposed vertical magnetic field, $B_0/B_{eq} = 0.5$, the localized magnetic flux concentrations relevant for sunspot formation analysis are observed for particularly weak magnetic fields. Moreover, the vertical profiles of $q_p(z)$ shown in Fig. 5.18 indicate that the effective magnetic pressure measured in the simulations is more negative (at the deepest layers of the domain) as the external magnetic field imposed is weaker. Similarly, NEMPI operates at a regime for which $B_0/B_{eq} << 1$, as shown in the literature (Kleeorin et al. (1989), Kleeorin et al. (1996), Rogachevskii & Kleeorin (2007), Brandenburg et al. (2011), (Losada et al., 2014), Käpylä et al. (2012), Käpylä et al. (2016)). This suggest that NEMPI could be taking part in the formation of magnetic structures in these simulations. However, our simulations with $B_0/B_{eq} = 0.01$ did not reveal the structure formation. Further work is required to analize the presence of such instability and its correlation with the appearance of the magnetic structures observed in this work. To do that, it is necessary to estimate the growth rate of NEMPI as given by eq. (2.50). That is, we need to determine for each of our simulations if the derivative of the effective magnetic pressure P_m with respect to the parameter $\beta = \overline{B}/B_{eq}$ takes negative values for the instability to develop. Simulations with horizontal magnetic field are a priority of our future work. The role of NEMPI in such simulations must be studied as well.

It is clear that improvements to resolve better the layer of small scale convection are needed. The implementation of a better boundary condition for the magnetic field could result in more realistic magnetic structures at the upper boundary. Perhaps including an additional convectively-stable layer at the top of the domain to simulate the solar atmosphere is also important for the structure formation. We also need to create larger convective structures at the adiabatic layer, which can be done by increasing the extent of the domain in the vertical direction. Effects of compressibility and radiative energy transport may also play an important role in the upper layers of the domain.

Bibliography

Babcock, H. D. 1959, ApJ, 130, 364

Beck, R., & Wielebinski, R. 2013, Magnetic Fields in Galaxies, ed. T. D. Oswalt & G. Gilmore, 641

Birch, A. C., Schunker, H., Braun, D. C., et al. 2016, Science Advances, 2, e1600557

Borrero, J. M., & Ichimoto, K. 2011, Living Reviews in Solar Physics, 8

Brandenburg, A., Gressel, O., Jabbari, S., Kleeorin, N., & Rogachevskii, I. 2014, A&A, 562, A53

Brandenburg, A., Kemel, K., Kleeorin, N., Mitra, D., & Rogachevskii, I. 2011, ApjL, 740, L50

Brandenburg, A., Kleeorin, N., & Rogachevskii, I. 2010, Astronomische Nachrichten, 331, 5

Brun, A. S., Miesch, M. S., & Toomre, J. 2004, ApJ, 614, 1073

Busse, F. 2007, Cowling's Theorem, ed. D. Gubbins & E. Herrero-Bervera (Dordrecht: Springer Netherlands), 138–139

Caligari, P., Moreno-Insertis, F., & Schussler, M. 1995, ApJ, 441, 886

Cameron, R. H., Dikpati, M., & Brandenburg, A. 2016, Space Science Reviews, 1

Cameron, R. H., Dikpati, M., & Brandenburg, A. 2016, Space Sci. Rev.

Charbonneau, P. 2010, Living Reviews in Solar Physics, 7

—. 2014, ARA&A, 52, 251

Choudhuri, A. R. 2013, in IAU Symposium, Vol. 294, Solar and Astrophysical Dynamos and Magnetic Activity, ed. A. G. Kosovichev, E. de Gouveia Dal Pino, & Y. Yan, 37–47

Christensen-Dalsgaard, J., Dappen, W., Ajukov, S. V., et al. 1996, Science, 272, 1286

Cline, K. S. 2003, PhD thesis, UNIVERSITY OF COLORADO AT BOULDER

Cossette, J.-F. 2015, PhD thesis, Université de Montreal

Cowling, T. G. 1945, MNRAS, 105, 166

Dasi-Espuig, M., Solanki, S. K., Krivova, N. A., Cameron, R., & Peñuela, T. 2010, A&A, 518, A7

Davidson, P. 2015, Turbulence: An Introduction for Scientists and Engineers (OUP Oxford)

di Mauro, M. P., Cardini, D., & Marconi, M. 2010, Synergies between Solar and Stellar Modelling

Dikpati, M., & Charbonneau, P. 1999, ApJ, 518, 508

Domaradzki, J. A., Xiao, Z., & Smolarkiewicz, P. K. 2003, PoF, 15, 3890

Domínguez Cerdeña, I., Sánchez Almeida, J., & Kneer, F. 2003, A&A, 407, 741

Duvall, Jr., T. L. 2003, in ESA Special Publication, Vol. 517, GONG+ 2002. Local and Global Helioseismology: the Present and Future, ed. H. Sawaya-Lacoste, 259–262

Falkovich, G. 1994, Physics of Fluids, 6, 1411

Fan, Y. 2009, Living Reviews in Solar Physics, 6

Fan, Y., Abbett, W. P., & Fisher, G. H. 2003, ApJ, 582, 1206

Ferriz-Mas, A., & Schuessler, M. 1990, Washington DC American Geophysical Union Geophysical Monograph Series, 141

Ferriz-Mas, A., & Schüssler, M. 1993, Geophysical and Astrophysical Fluid Dynamics, 72, 209

—. 1995, Geophysical and Astrophysical Fluid Dynamics, 81, 233

Ghizaru, M., Charbonneau, P., & Smolarkiewicz, P. K. 2010, Ap. J. Lett., 715, L133

Ghosal, S. 1996, Journal of Computational Physics, 125, 187

Govoni, F., & Feretti, L. 2004, International Journal of Modern Physics D, 13, 1549

Grinstein, F., Margolin, L., & Rider, W. 2007, Implicit Large Eddy Simulation: Computing Turbulent Fluid Dynamics (Cambridge University Press)

Guerrero, G., & de Gouveia Dal Pino, E. M. 2008, A&A, 485, 267

Guerrero, G., & Käpylä, P. J. 2011, A&A, 533, A40

Guerrero, G., Smolarkiewicz, P. K., de Gouveia Dal Pino, E. M., Kosovichev, A. G., & Mansour, N. N. 2016, ApJ, 819, 104

Guerrero, G., Smolarkiewicz, P. K., Kosovichev, A. G., & Mansour, N. N. 2013, ApJ, 779, 176

Hale, G. E., Ellerman, F., Nicholson, S. B., & Joy, A. H. 1919, ApJ, 49, 153

Hanasoge, S. M., Duvall, T. L., & Sreenivasan, K. R. 2012, Proceedings of the National Academy of Science, 109, 11928

Hathaway, D. H. 2015, Living Reviews in Solar Physics, 12

Hathaway, D. H., Beck, J. G., Bogart, R. S., et al. 2000, Sol. Phys., 193, 299

Hathaway, D. H., Upton, L., & Colegrove, O. 2014, ArXiv e-prints

Haugen, N. E. L., & Brandenburg, A. 2004, Phys. Rev. E, 70, 026405

—. 2006, Physics of Fluids, 18, 075106

Hirt, C. W. 1969, Physics of Fluids, 12, II

Hotta, H., Rempel, M., & Yokoyama, T. 2014, ApJ, 786, 24

—. 2015, ApJ, 798, 51

Howe, R. 2009, Living Reviews in Solar Physics, 6

Howe, R., Christensen-Dalsgaard, J., Hill, F., et al. 2005, Astrophys. J., 634, 1405

Howe, R., Hill, F., Komm, R., et al. 2011, in Journal of Physics Conference Series, Vol. 271, Journal of Physics Conference Series, 012074

Howe, R., Komm, R., & Hill, F. 2000, Solar Phys., 192, 427

Hoyt, D. V., & Schatten, K. H. 1998, Sol. Phys., 179, 189

Hughes, D. W., Rosner, R., & Weiss, N. O. 2012, The Solar Tachocline

Ilonidis, S., Zhao, J., & Kosovichev, A. G. 2011, AGU Fall Meeting Abstracts

Jackiewicz, J., Serebryanskiy, A., & Kholikov, S. 2015, ApJ, 805, 133

Jiang, J., Hathaway, D. H., Cameron, R. H., et al. 2014, Space Sci. Rev., 186, 491

Kaneda, Y., Ishihara, T., Yokokawa, M., Itakura, K., & Uno, A. 2003, Physics of Fluids, 15, L21

Käpylä, P. J., Brandenburg, A., Kleeorin, N., Käpylä, M. J., & Rogachevskii, I. 2016, A&A, 588, A150

Käpylä, P. J., Brandenburg, A., Kleeorin, N., Mantere, M. J., & Rogachevskii, I. 2012, MNRAS, 422, 2465

Käpylä, P. J., Korpi, M. J., Brandenburg, A., Mitra, D., & Tavakol, R. 2010, Astronomische Nachrichten, 331, 73

Kemel, K., Brandenburg, A., Kleeorin, N., Mitra, D., & Rogachevskii, I. 2012, Sol. Phys., 280, 321

—. 2013, Sol. Phys., 287, 293

Khomenko, E. V., Collados, M., Solanki, S. K., Lagg, A., & Trujillo Bueno, J. 2003, A&A, 408, 1115

Kitiashvili, I. N., Kosovichev, A. G., Mansour, N. N., & Wray, A. A. 2016, Ap. J. Lett., 821, L17

Kleeorin, N., Mond, M., & Rogachevskii, I. 1996, A&A, 307, 293

Kleeorin, N. I., Rogachevskii, I. V., & Ruzmaikin, A. A. 1989, Pisma v Astronomicheskii Zhurnal, 15, 639

Kosovichev, A. G. 1999, Journal of Computational and Applied Mathematics, 109, 1

Kosovichev, A. G., Duvall, Jr., T. L. ., & Scherrer, P. H. 2000, Sol. Phys., 192, 159

Kosovichev, A. G., Zhao, J., & Ilonidis, S. 2016, ArXiv e-prints

Lipps, F. B., & Hemler, R. S. 1982, Journal of the Atmospheric Sciences, 39, 2192

Losada, I. R., Brandenburg, A., Kleeorin, N., & Rogachevskii, I. 2014, A&A, 564, A2

McElhinny, M. W., & Senanayake, W. E. 1980, Journal of Geophysical Research: Solid Earth, 85, 3523

Moffatt, H. K. 1978, Magnetic field generation in electrically conducting fluids

Nandy, D., & Choudhuri, A. R. 2002, Science, 296, 1671

Nordlund, Å., Stein, R. F., & Asplund, M. 2009, Living Reviews in Solar Physics, 6

Ogura, Y., & Phillips, N. A. 1962, Journal of the Atmospheric Sciences, 19, 173

Oran, E., & Boris, J. 2005, Numerical Simulation of Reactive Flow (Cambridge University Press)

Orozco Suárez, D., Bellot Rubio, L. R., del Toro Iniesta, J. C., et al. 2007, ApJL, 670, L61

Parker, E. N. 1955a, ApJ, 122, 293

—. 1955b, ApJ, 121, 491

Pope, S. 2000, Turbulent Flows (Cambridge University Press)

Prusa, J. M., Smolarkiewicz, P. K., & Wyszogrodzki, A. A. 2008, Computers & Fluids, 37, 1193

Racine, É., Charbonneau, P., Ghizaru, M., Bouchat, A., & Smolarkiewicz, P. K. 2011, ApJ, 735, 46

Reiners, A. 2012, Living Reviews in Solar Physics, 9

Rieutord, M., Meunier, N., Roudier, T., et al. 2008, A&A, 479, L17

Rieutord, M., & Rincon, F. 2010, Living Reviews in Solar Physics, 7

Roberts, G. O. 1970, Philosophical Transactions of the Royal Society of London Series A, 266, 535

Roberts, P. H., & Glatzmaier, G. A. 2001, Geophysical and Astrophysical Fluid Dynamics, 94, 47

Rogachevskii, I., & Kleeorin, N. 2007, PRE, 76, 056307

Schad, A., Timmer, J., & Roth, M. 2013, Ap. J. Lett., 778, L38

Schou, J., Antia, H. M., Basu, S., et al. 1998, ApJ, 505, 390

Schou, J., Scherrer, P. H., Bush, R. I., et al. 2012, Sol. Phys., 275, 229

Schrijver, C. J., & Siscoe, G. L. 2012, Heliophysics: Evolving Solar Activity and the Climates of Space and Earth

Schrijver, C. J., & Zwaan, C. 2008, Solar and Stellar Magnetic Activity

Schwabe, M. 1844, Astronomische Nachrichten, 21, 233

Schwenn, R. 2006, Living Reviews in Solar Physics, 3

Shibata, K., & Magara, T. 2011, Living Reviews in Solar Physics, 8

Smolarkiewicz, P. K., & Charbonneau, P. 2013, J. Comput. Phys., 236, 608

Smolarkiewicz, P. K., Grubišić, V., & Margolin, L. G. 1997, Monthly Weather Review, 125, 647

Smolarkiewicz, P. K., & Margolin, L. G. 1998a, J. Comput. Phys., 140, 459

—. 1998b, Journal of Computational Physics, 140, 459

Socas-Navarro, H., & Sánchez Almeida, J. 2003, ApJ, 593, 581

Spruit, H. C., Nordlund, A., & Title, A. M. 1990, ARA&A, 28, 263

Spruit, H. C., & van Ballegooijen, A. A. 1982, A&A, 106, 58

Stein, R. F., & Nordlund, A. 1989, Ap. J. Lett., 342, L95

Strugarek, A., Beaudoin, P., Brun, A. S., et al. 2016, ArXiv e-prints

Ulrich, R. K. 2010, ApJ, 725, 658

Yashiro, S., Gopalswamy, N., Michalek, G., et al. 2004, Journal of Geophysical Research (Space Physics), 109, A07105

Yoshimura, H. 1975, ApJ, 201, 740

Zhao, J., Bogart, R. S., Kosovichev, A. G., Duvall, Jr., T. L., & Hartlep, T. 2013, Ap. J. Lett., 774, L29

Zhao, J., Kosovichev, A. G., & Duvall, Jr., T. L. 2001, ApJ, 557, 384

Zwaan, C. 1996, Sol. Phys., 169, 265